# 論文 / 著書情報
# Article / Book Information

| | |
|---|---|
| 題目(和文) | クライオ遠視野顕微鏡による 蛍光体のナノメートル確度での相対位置決定 |
| Title(English) | Cryogenic far-field localization microscopy of individual fluorophores with nanometer accuracy |
| 著者(和文) | 古林 琢 |
| Author(English) | Taku Furubayashi |
| 出典(和文) | 学位:博士(理学),<br>学位授与機関:東京工業大学,<br>報告番号:甲第11370号,<br>授与年月日:2020年3月26日,<br>学位の種別:課程博士,<br>審査員:松下 道雄,笹本 智弘,佐藤 琢哉,納富 雅也,VACHA MARTIN |
| Citation(English) | Degree:Doctor (Science),<br>Conferring organization: Tokyo Institute of Technology,<br>Report number:甲第11370号,<br>Conferred date:2020/3/26,<br>Degree Type:Course doctor,<br>Examiner:,,,, |
| 学位種別(和文) | 博士論文 |
| Type(English) | Doctoral Thesis |

Ph.D. thesis

# Cryogenic far-field localization microscopy of individual fluorophores with nanometer accuracy

Taku Furubayashi

School of Science, Department of Physics
Tokyo Institute of Technology

Revised on February 20th, 2020
Submitted on December 27th, 2019

# Abstract

One of subjects of molecular biology is to understand biochemical processes of cell in terms of chemical reactions of individual biomolecules. Among microscopic methods for non-invasive observation of cells, far-field fluorescence microscopy is unique in its high sensitivity. While the sensitivity has reached to the ultimate level of single molecules, spatial resolution of fluorescence microscopy is limited by diffraction of the light in use (around 700 nm), which is much larger than the size of biomolecules. If the three-dimensional spatial precision is improved to an angstrom level, various molecular arrangements in the cell can be visualized on an individual basis. This thesis represents development of cryogenic far-field fluorescence localization microscopy with nanometer accuracy.

By designing a mechanically stable cryogenic microscope, the imaging stability of the setup with an exposure time of 5 minutes reached 0.05 nm in standard deviation at a temperature of 1.8 K in super-fluid helium. Optically, this setup is reflecting microscope with a numerical aperture of 0.99. The essential optics to realize the performance is the reflecting objective developed by our laboratory. This objective consists of a pair of mirrors made on a single piece of fused silica. Monolithic design of the objective guarantees the optical alignment of the mirrors against temperature cycling between room temperature and liquid-helium temperatures. For fluorescence imaging, the most crucial alignment in the setup is the position of the objective with respect to the sample. The objective and the sample were fixed to a monolithic holder and were placed in super-fluid helium at 1.8 K.

In 3D localization microscopy of individual fluorophores, different methods of localization were used for the lateral ($xy$-) and axial ($z$-) positions. For the $xy$-localization, the fluorescence image on the focal plane was taken by a charge coupled device (CCD) camera, and the position of the fluorophore was determined as the centroid of the CCD image. The fluorescence intensity of individual fluorophores shows on/off behavior, which is called

blinking. The observed image is free from noise due to blinking, because the CCD camera detects all of the positions on the image plane simultaneously.

The $z$-position of the fluorophore is determined by defocus imaging, which uses images taken at an out-of-focus position. The defocus image consists of the $xy$-image of the point-spread function (PSF) and diffraction rings. Since information about the $z$-position is contained in the width of PSF, thee image was fitted to a model function of PSF. Because the diffraction rings were found to mislead the fitting to a false minimum, the diffraction rings were removed by on-chip binning of the CCD camera or frequency filtering in the reciprocal space. The angstrom-precision of our cryogenic localization microscopy was demonstrated by localization measurements of fluorescent molecule (ATTO647N). An individual ATTO647N at 1.8 K was localized with standard errors of 0.53 nm ($x$), 0.31 nm ($y$), and 0.90 nm ($z$). To build one image, $10^6$ fluorescence photons from the molecule were accumulated in 5 min.

The localization measurement of individual ATTO647N was repeated on the same one fluorophore and the reproducibility of the localized position was examined. The reproducibility of the measurement is called precision. The localization precision of a single fluorophore reached to one-nanometer level. The next step towards the nanometer-level microscopy of whole cell is to localize two or more fluorophores and reconstitute the 3D arrangement of the fluorophores in the sample. The correctness of measurement of relative positions is called accuracy.

As an example of biomolecule labeled with two fluorescent dyes, we designed a dual-labeled double-stranded (ds) DNA molecule consisting of 30 base pairs (bp). The 5' and 3' ends of the DNA was labeled with an infrared and a red dyes, respectively. The NIR dye was Alexa Fluor 750 (Ax750) or sulfo cyanine 7 (sCy7) and the red dye was ATTO655 (AT655). The length of the 30-bp dsDNA is 10.2 nm. The dyes are bonded to the DNA molecule via a flexible linker of a length of a few nm. Thus, the distance between the NIR and red dyes bonded to the same DNA molecule should measure about 10 nm.

We started the 3D localization of the dual-labeled DNA molecule with position determination of the two dyes. Each of the dyes was localized with a 1 nm precision, as it was so in the case of ATTO647N. The distance between the two dyes, however, distributed from 0 to 50 nm. The discrepancy was found to be originated from the dipole character of the fluorescence emission. Since individual fluorophores are orientationally fixed at 1.8 K, the fluorescence emission from a single fluorophore should be treated as dipole emission. As a result, PSF may tilt from the $z$-axis and the $xy$-centroid may depend on the $z$-position at which the $xy$-image is taken. The amount of the $z$-uncertainty is the focal depth of about 0.7 µm. Because different fluorophores orient differently, the centroid of fluorophores deviates differently from the true position. Thus, relative distance between two fluorophores will suffer from $z$-dependent $xy$-deviation. This systematic error will vanish if the centroid is determined on the true focal plane of $z = 0$. By taking into account of the $z$-dependent $xy$-centroid, the length of dsDNA was reproduced. As for the lateral ($xy$) cross-section, 19 images were taken along the $z$-axis with an interval of 100 nm. The distribution of $D_{xy}$ was centered around the DNA length of about 10 nm with the standard deviation of 5 nm.

In conclusion, towards nanometer level microscopy of multiple biomolecules in cell, we demonstrate a nanometer accuracy of far-field fluorescence localization microscopy using near-infrared and red fluorophores bonded to the both ends of a 10 nm-long dsDNA.

# Contents

Chapter 1 Introduction 1

# Chapter 1

# Introduction

## 1.1 Overview of this Ph.D. thesis

A single cell is composed of multiple biomolecules, proteins, DNA, peptides. For example, B. Ho et al. calculated that $10^7$ proteins are contained in a single cell [1]. Biological activity in cells is regulated by a variety of molecules that interact with each other. To understand the biological activity, the structure of a biomolecules and their complexes has been studied. The experimental methods employed are X-ray crystallography, nuclear magnetic resonance (NMR) spectroscopy, and cryogenic electron microscopy (cryo-EM) [2]. X-ray crystallography has been established from three decades [2]. X-ray crystallography provides the stereostructure of a biomolecule from diffraction image of a crystal of biomolecules. NMR spectroscopy provides information about their dynamics and structure in a solution. The application of NMR is limited to small biomolecules of a size less than 30 kDa [3] . For reference, the average molecular weight of protein is 55 kDa [1]. Cryo-EM provides structure of a biomolecule from thousands of electron microscopic images taken for individuals of the molecules that are all identical in chemical composition and structure [2,4]. The method is so-called single particle analysis. In the single particle analysis, the structure of purified biomolecules in glass-water film can be determined. The cryo-EM can be applied to those biomolecules for which crystallization has not been successful. Recently, the single particle analysis can be applied to the complex of couple of biomolecules. However, the method remains still difficult to apply to the interior of cell. Among microscopic methods proposed for investigation of cell-interior. Far-field fluorescence microscopy is non-invasive imaging of whole cell. The sensitivity of fluorescence detection has been at single-molecule level already for several decades [5,6]. Chemical specificity of target molecules is realized by the technique of immunofluorescence staining of cell. By utilizing specificity of immunological antigen-antibody reactions, fluorescence microscopy is applied widely in the frontiers of molecular biology.

Resolution of far-field fluorescence microscope is not enough for molecular imaging in cell. Super-resolution fluorescence microscopies are developed to observe structures smaller than the optical resolution. Commonly used microscopies are stimulated-emission-depletion microscopy (STED), stochastic optical reconstruction microscopy (STORM), and so on [7]. STED is a technique using two pulsed laser lights to reduce the fluorescence area by STED light, which causes stimulated emission [8]. After photo-excitation by the first laser pulse, the second pulse of STED is applied before the target molecules emit fluorescence. The shape of STED light is designed on purpose to be concentric doughnut in such a way that, among the molecules excited by the first laser pulse, only those at periphery of the beam are depleted, and others at the center survive stimulated emission to form a smaller fluorescence spot. Note that STED is a method to reduce the size of fluorescence spot which consists of an ensemble of molecules. STED is not a scheme which improves the resolution of single molecule imaging. STORM is single molecule localization microscopy, and is a technique to observe for observing individual molecule [9]. Under continuous-wave (cw) excitation, individual fluorophores, in general, resides either in the fluorescent state, where an individual fluorophore repeats photo-excitation-emission cycle, or in the dark state where after photo-excitation fluorophore is shelved in a metastable state. Going back and forth between the two states is called blinking. Utilizing the blinking phenomenon of single fluorophore, each molecule is localized with precision smaller than the optical resolution. The localized positions of fluorophores compose molecular image within optical resolution. In this method, localization with nanometer precision requires long time accumulation because fluorescence of single molecule is weak. The precision of cellular imaging is limited several tens nanometers because of biomolecules moving by thermal motion such as Brownian movement and diffusion in cell. Therefore, we use cryogenic immobilization technique in order to stop the molecular motion. Rapidly cooling the sample below the glass transition temperature keeps biomolecules and cells in glassy water matrix. It can be stored in near natural state.

In this Ph.D. study, we demonstrated localization of the two ends of individual double-stranded DNA (dsDNA) molecule using the cryogenic immobilization. To realize nanometer accuracy in fluorescence localization microscopy of an individual molecule, we developed a cryogenic fluorescence microscope with mechanical stability of 0.05 nm and a 0.99-numerical aperture. Using this microscopy, a single ATTO647N molecule in the water matrix at a temperature of 1.8 K was localized with an angstrom precision in 3D. However, the precision of single fluorophore often differs from the accuracy of relative distance between multiple fluorophore. We measured the distance of fluorophores bonded to the ends of dsDNA whose distance is 10.2 nm. In conventional fluorescence localization using far-field microscopy, an $xy$-centroid for each fluorophore is determined from an image at a $z$-position within a diffraction-limited focal depth (the $z$-localization precision $\Delta_z \sim 700$ nm for the microscope). Although $xy$-localization precision $\Delta_{xy}$ was 1 nm, the $xy$-projection of the distance between the two fluorophores ($D_{xy}$) distributed from 0 to 50 nm. Mislocalization was mainly causes by $z$-dependent $xy$-shift due to the dipole orientation effect. This $xy$-shift was reduced by improving the $z$-localization from $\Delta_z \sim 700$ to 11 nm and $\Delta_{xy} = 1$ nm. By correcting the mislocalization, the distribution of $D_{xy}$ was centered around the dsDNA length of 10 nm, and a standard deviation of $D_{xy}$ was 5 nm. This result shows that nanometer-accuracy localization of multiple fluorophores with far-field microscopy requires not only $xy$-precision but also $z$-precision, far beyond the diffraction limit (see Chapter 3).

The key component for the mechanical stability of the cryo-microscope is cryogenic objective mirror. To realize a high-mechanical stability in a cryogenic microscope, an objective lens and a sample are set to a monolithic holder and the holder is cooled down to a few K [10]. Because, a commercially available objective-lens does not work under cryogenic conditions, our laboratory developed a reflecting objective mirror that works at a few K [11–13]. Moreover, the stability against the ambient-temperature fluctuation was improved by adjusting thermal expansivity of the holder and internal holder parts to be almost the same. Around the image unit part, optical parts such as mirror are mounted to an airtight stainless-steel boxes in order to improve the stability. These stabilization improvement were essential for localization of individual fluorophore with angstrom precision (see Chapter 2).

In 3D localization microscopy with angstrom precision, we used charge coupled device (CCD) for localization lateral ($xy$-) position because the blinking noise of a single fluorophore is free in the 2D detection. An axial ($z$-) position is determined by defocus imaging that to seek the position from defocusing image [14]. The defocused image has width of expanding beam. In my experimental condition, the width of central disk is constant with depth of focus because of the objective mirror. The shading of the objective mirror affects PSF. The PSF has diffraction rings, which has $z$-position information. After excepting diffraction rings that has high frequency component by using binning (see Chapter 2) or Fourier transformation (see Chapter 3), the $z$-position is determined quantitative from beam width. By the methods of $xy$- and $z$-position localization, a position of individual ATTO647N molecule is determined with angstrom precision (see Chapter 2).

Localization with angstrom precision revealed that the dipole radiation causes systematic error with several tens nanometers. A single molecule fluorescence is dipole radiation, which is not isotropic radiation. When fluorescence from single molecule is focused, point-spread-function (PSF) is different from PSF of isotropic radiation. Several studies have reported that mislocalization causes from dipole orientation [15–22]. This problem is that even if the excitation light adjusted, PSF is tilted from a principal ray depended a direction of transition dipole. Simulation of dipole radiation clarifies that $xy$-position depends $z$-position shifting. When the microscope is not accurately focused, a systematic error occurs at the position of $xy$-plane. A molecular level imaging requires observing 3-dimensional PSF because it is difficult to adjust to focus accurately from single image. We demonstrated nanometer accuracy of far-field fluorescence localization microscopy at 1.8 K by correcting systematic error using 3D-PSF (see Chapter 3).

In far-field fluorescence microscopy, a previous existing method cannot localize the position of single fluorophore. We developed cryogenic far-field fluorescence microscope that can localize 3D position of individual fluorophore with angstrom precision. Due to the precision, the systematic error that is larger than molecular level is revealed. We demonstrated several nanometer accuracy imaging with correcting the systematic error. Chapter 2 contains localization with angstrom precision and Chapter 3 contains imaging with molecular accuracy. In this chapter, the problems of existing fluorescence microscopies are mentioned first. Next, the cryogenic fluorescence microscope is described. Finally, the problems and solution strategies of single molecule localization with molecular accuracy are shown.

## 1.2 Fluorescence microscopy

Fluorescence microscopy is widely used to observe a 3D spatial distribution of biomolecules at a cellular interior. By using a biochemical technique, fluorophores can selectively labeled to an desired biomolecule. The labeled biomolecule can be captured by the fluorescence microscopy. The sensitivity of the fluorescence microscopy had reached to single molecule level [5]. The key to realize the single molecule sensitivity is a small background in the fluorescence microscopy. Figure 1.1 shows absorption and fluorescence spectra of ATTO647N molecule in phosphate buffer solution at 296 K. The excitation light ($\lambda$ = 637 nm) is indicated by an arrow. In a stokes law, the wavelength of fluorescent light is longer than that of the excitation light. Although the scattering of the excitation light is $10^5$–$10^6$ times longer than the fluorescence of a single fluorophore, the strong scattering can be completely blocked with fluorescence filter. Figure 1.1(b) shows Jablonski diagrams showing energy transition of a fluorescent molecule. The ground-state low lying and excited singlet-state are depicted by $S_0$ and $S_1$. The $S_0$ and $S_1$ stats have vibrionic stats that is shown v= 0, v= 1, v= 2, and so on. When a molecule is excited, the energy state of molecule is transmitted $S_0 \rightarrow S_1$ and v= 0 state. The excited molecule relaxes to vibrational grand-state $v_0$ in the $S_1$ state with in a few picosecond. After relaxed to $v_0$ of $S_1$ state, the molecule returns to ground state and emits fluorescence.

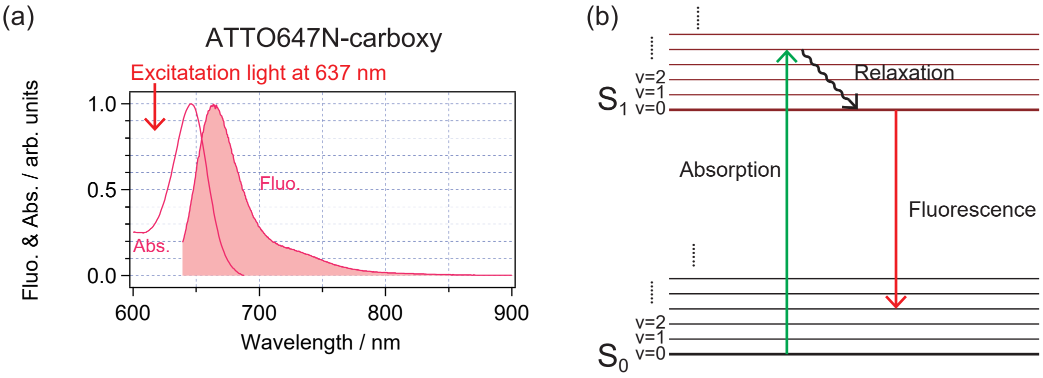

Figure 1.1 Absorption and fluorescence of a fluorescence molecule. (a) Spectra of absorption and fluorescence of ATTO647N-carboxy. (b) A simplicity Jablonski diagrams of energy transition of a fluorescent molecule. The excited molecule absorbed excitation light is relaxed to lower vibration state, the molecule returns to ground state and emits fluorescence light.

In fluorescence microscopy, fluorescent image can be taken excepting excitation because the wavelength of fluorescence differs from excitation light. Figure 1.2 shows schematic illustration of fluorescence microscope. The light source is lamp. The spectral of the lamp is filtered with ac excitation lifter. The optically filtered excitation light is reflected with a dichroic mirror and is focused with an objective lens. The fluorescence of the sample is collected and collimated with the objective lens. The collimated fluorescence light transmits the dichroic mirror and fluorescence filter. The fluorescence filter is blocked the scattering light. The fluorescence light is focused with an imaging mirror and is imaged on CCD detector. However, observing of network among biomolecules has been difficult because the resolution of fluorescence microscope is much worse than the sized of network. A light does not become a point in focus, but disk shown Fig. 1.3. Regarding the disk, the resolution of Rayleigh criterion $d_r$ is defined in following equation;

$$d_r = 0.61 \frac{\lambda}{\mathrm{NA}} \,. \tag{1.1}$$

Here, this distance of $d_r$ is radius of the first dark ring, $\lambda$ is wavelength of light, NA is numerical aperture defined by

$$\mathrm{NA} = n \sin\theta \,, \tag{1.2}$$

where $n$ is index of refraction of medium in which the object is placed, and $\theta$ is the maximal half-angle of the cone of light entering or exiting the lens. When the light disk is made from single fluorophore, the position of fluorophore is localized with molecular precision [23]. However, when the distance of two fluorophores is less than resolution of light, localization of positions of fluorophore is difficult. In the light direction, the resolution $d_z$ is expressed following equation:

$$d_z \sim \frac{n\lambda}{\mathrm{NA}^2} \,. \tag{1.3}$$

Furthermore, fluorescence microscopy has another problem that is background noise. In Figure 1.1, the sample is observed wide field because the excitation light illuminates all the sample. On the other hand, the molecular precision is difficult because many fluorophores emit the light and obstruct localization. To resolve this back ground problem, confocal fluorescence microscope was developed.

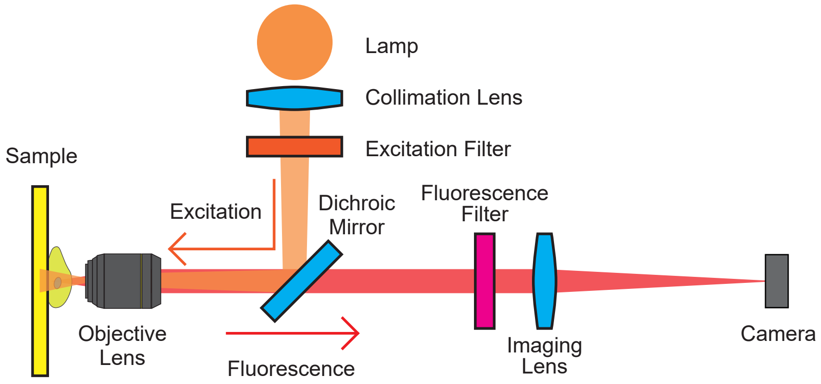

Figure 1.2 A schematic diagram of fluorescence microscope. The light emitted from the lamp excites fluorophores in the sample. The excitation light is limited wavelength using bandpass filter. The fluorescence from the sample is collimated and passes through the dichroic mirror and fluorescence filter to except excitation light. The camera detects the fluorescence image on focus of the imaging lens.

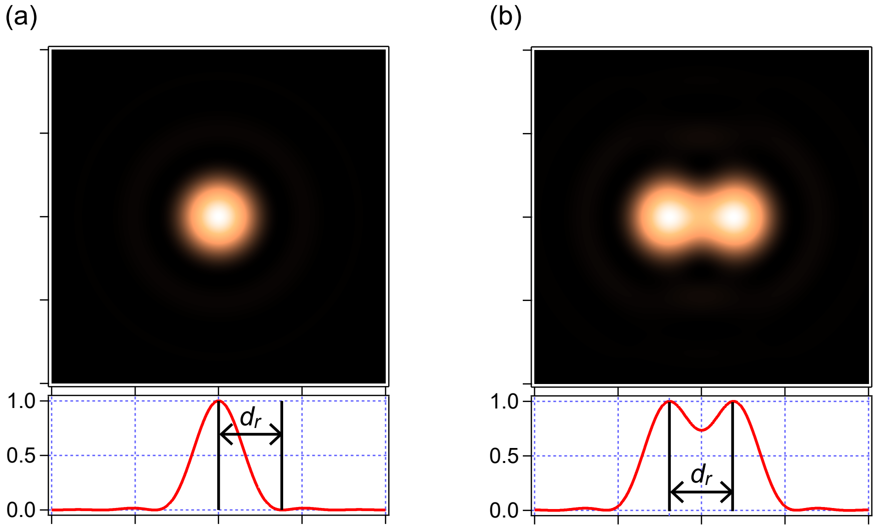

Figure 1.3 Simulated images from point light source on focus. (a) From single light source image. The radius of the first dark ring $d_r$ is defined by Eq. 1.1. (b) From two light sources image. The distance of two light source is $d_r$. When the distance is nearer than $d_r$, localization positions with high precision is difficult.

## 1.3 Confocal microscopy

Confocal microscopy is an optical imaging technique for 3D imaging. In confocal microscope, two pinholes are used for reduced blurring of the image from light scattering, increased effective resolution and signal-to-noise ratio, possible optical-axial-scanning, and so on [24]. The first pinhole is excitation pinhole and limits the position of the field of illumination on the microscope axis. The second pinhole is imaging pinhole and restricts of the field of view. This pinhole is placed confocal position to the illuminated spot in the specimen and to the first pinhole. Figure 1.4 shows schematic diagram of a typical confocal fluorescence microscope. The excitation light from the laser passes through the first pinhole by focusing lens. The light through the pinhole is collimated with the lens and is reflected with dichroic mirror. The reflected excitation light is focused by an objective lens and illuminates a point of three-dimensional position. The fluorescence emits from only the excited position. The fluorescence is collimated with the objective lens and is transmitted the dichroic mirror and fluorescence filter. The transmitted light is focused with imaging lens. The second pinhole lets through fluorescence from only confocal position to the illumination spot and the first pinhole. In order to get the three-dimensional image, the sample is moved for 3D axis by the stage. Confocal microscopy improves the optical imaging resolution and contrast. However, small fluorophores among a light resolution are not resolved each positions with precision less than the light resolution. To observe structures of the size under the light resolution, super-resolution fluorescence microscopes are developed.

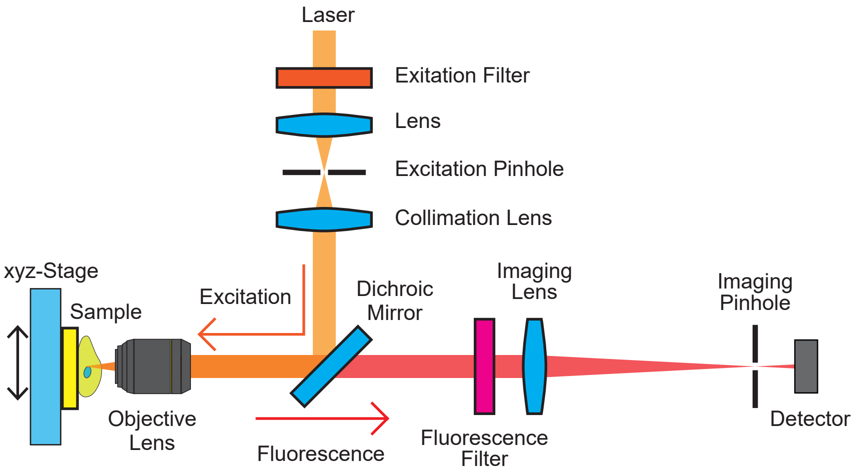

Figure 1.4 Schematic diagram of a confocal fluorescence microscope. Compared with Fig. 1.1, this microscope has two pinholes. The first pinhole placed excitation side limits the position of the field of illumination on the microscope axis. The second pinhole placed before the detector lets through fluorescence from only confocal position to the illumination spot and the first pinhole. By scanning the sample stage for *xyz*-direction, 3-dimentional image is obtained with low background noise and optical resolution.

## 1.4 Super-resolution fluorescence microscopy

In order to observe cellular small targets whose size is smaller than optical resolution, super-resolution far-field fluorescence microscopies have been developed. Stimulated-emission-depletion (STED) fluorescence microscopy, sub-diffraction-limit imaging by stochastic optical reconstruction microscopy (STORM), and so on are commonly used [7]. STED is the method of becoming smaller the effective fluorescence spot using stimulated emission. Fluorophores of the center spot because the excitation shape of STED light is doughnut. STORM is the method of single molecule localization and composition. A single fluorescence molecule is occurred blinking or photo-switching. Using these on-off fluorescence emittance, the positions of molecules are localized each molecule with several tens nanometer. Another mothed is spectrally selective imaging [25]. Single molecule localization is executed by excitation only single molecule because of selecting absorption spectrum. In following sections, details of these microscopies are described.

### 1.4.1 Stimulated-emission-depletion (STED) microscopy

STED is the method of using stimulated emission [8]. Figure 1.5(a) shows schematic diagram of STED. STED beam is made of phase modulated laser and its shape becomes doughnut on a objective plane. Using dichroic mirrors, illumination beam and STED beam are aligned. The beams are focused with an objective lens. On the focal plane of objective lens, the the shape of excitation spot is Airy disk (shown Fig 1.5(b) left) and the shape of STED spot is doughnut (shown Fig 1.5(b) centor.) At objective space on the sample, STED light quenches fluorescence which is excited by the excitation beam. The effective fluorescence spot is several tens nanometer of a hole of the doughnut shape of STED. This resolution is limited by the hole of STED. The hole can be smaller intensifying the STED light. However, the high power STED light occurs fluorescence bleaching quickly. The resolution for light axial direction is same as normally fluorescence microscope. Therefore, STED is not suitable for molecular resolution imaging and it can observe the ensemble molecules and time resolution is about milliseconds for 512 times 512 image [7].

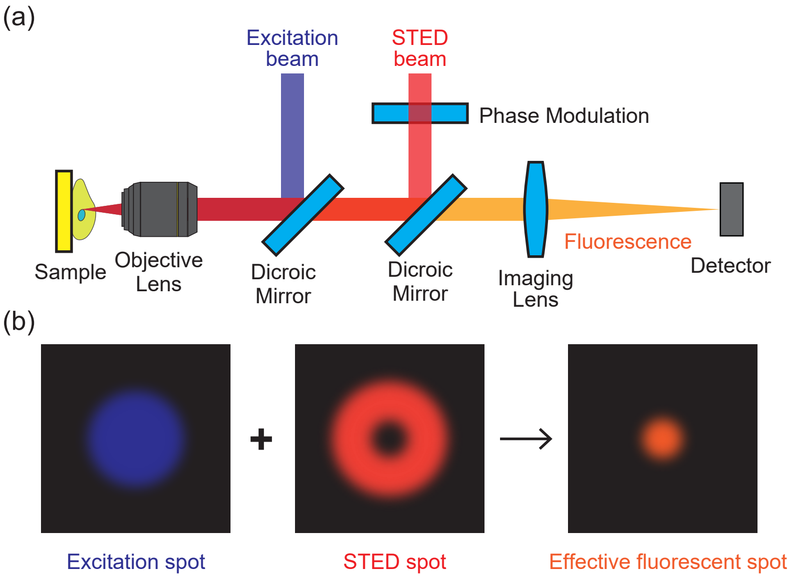

Figure 1.5 Schematic diagram of STED. (a) is schematic diagram of optical setup and (b) is images of beams and effective fluorescence on the sample plane. STED light is doughnut shape made from laser beam using phase modulation. Excitation and STED light illuminate the sample and the effective fluorescence spot is small as hole of STED light shown (b) because STED light causes stimulated emission.

### 1.4.2 Single molecule localization fluorescence microscopy

Some fluorescence dye occurs photo-switching. This is switching between fluorescence state and dark state using specific wavelength light. Using this phenomenon, sub-diffraction-limit imaging by stochastic optical reconstruction (STORM) [9] and photo-activated localization microscopy (PALM) [26] are developed for imaging individual molecules within optical resolution. An individual molecule of specific fluorophore goes and comes between fluorescence and dark state. A single image of multiple molecules within optical resolution contains fluorescence-state molecules and dark-state molecules. Figure 1.6 is shown STORM imaging process. First, all fluorophores are switched off using quenching light. In each cycle, a fraction of the fluorophores in the field of illuminated are switched on. This condition allows determining the position of the on state fluorophores with high precision. After observation, the fluorophore is switched off again. Repeating multiple times this cycle, positions of many fluorophores are determined in optical resolution. The precision of this localization of single fluorophore is no limit in theoretical because the precision scales as a $1/\sqrt{N}$, where $N$ is photon numbers in the spot for the shot noise limit. However, in living cell, biomolecules move by thermal motion such as Brownian movement and diffusion during accumulation time. The precision of STORM and PALM is several tens nanometers in living cell.

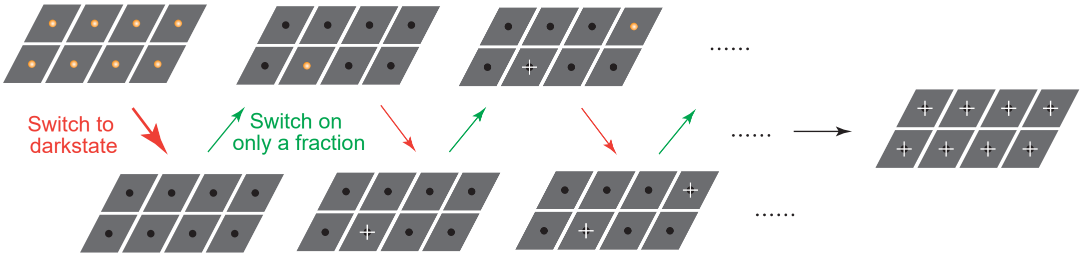

Figure 1.6 Imaging method of STORM [9]. Positions of each fluorophore in optical resolution are determined by fluorescence image of only individual molecule using photo-switching. In each image cycle, the fluorophores are switched off, individual molecule is switched on, and the position of molecule is determined. The overall image is reconstructed from the fluorophore positions obtained from photo-switching and determination cycles.

### 1.4.3 Spectrally selective imaging microscopy

For resolving the molecules internal of optical resolution, the solution is excitation and fluorescence one by one of the fluorophores. When absorption spectrum is resolved each fluorescence molecule, multiple molecules is resolved each position only single molecule excited using wavelength of single dye spectrum. A. Bloeß et al. reported that lateral position and orientation of 314 single molecules is obtained with 3.4 nm precision [25]. Bulk fluorescence excitation spectrum of 2,3,8,9-dibenzan-thanthrene (DBATT) in *n*-tetradecane (the molecular structure shown in Fig. 1.7) at 1.2 K has full width at half maximum (FWHM) of $\sim$ 600 GHz. However, using selective excitation light of 1 MHz frequency bandwidth, each spectrum of molecules reveals separate lines with a FWHM of 25 – 60 MHz that correspond to individual DBATT molecules. The position of single molecule can be determined from fluorescence image when single molecule is excited at single separate spectrum. A problem of spectrally selective imaging by Bloeß et al. is that used fluorophore is not suitable for biomolecule labeling and the solvent is *n*-tetradecane that is organic solvent. Main component of a cell is water. Recent research shows that single molecule spectrum of BODIPY581/591 and BODIPY558/568, which are dyes often used for biomolecule labeling, are narrower than ensemble spectrum of the dyes [27]. Microscopy of spectrally selective imaging for cellular is going to be realized using this technique.

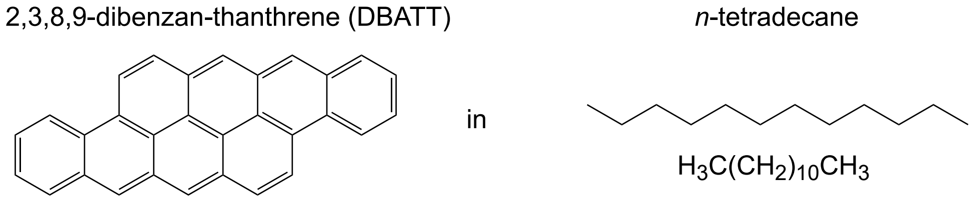

Figure 1.7 Molecular structures of DBATT and *n*-tetradecane which are used for Spectrally selective imaging in Bloeß et al. study.

## 1.5 Cryogenic fluorescence microscope

Under cellular molecular level imaging, observation requires immobilization biomolecules during acquisition time. To make immobilized condition, vitrificatiion technique is used in cryogenic electron microscopy. Therefore, we developed cryogenic fluorescence microscope for cellular imaging of molecular level accuracy. Previous study of cryogenic fluorescence microscopy has reported lateral localization of fluorophore in organic solvent with 3.4 nm precision [25]. Moreover, using same technique, the axial position of individual fluorophores is with $\sim$ 100 nm precision. Other study has demonstrated that 3D average position of fluorophores at 4 K was reconstructed from $xy-$images of thousands of molecules [28]. However, this study is almost the same as structure determination using cryo-EM that can determine more detail structure. A merit of cryogenic fluorescence microscope is practicable to observe immobilized individual molecules. Furthermore, cryo-immobilization occurs increasing lifetime until bleach fluorophore [29]. The longer lifetime of fluorescence, the better the precision of localization. Because of the above reasons, cryogenic fluorescence microscopes have developed by our laboratory.

The key optics for our cryogenic fluorescence microscope is cryo-resistant objective reflecting lens developed by our laboratory [11–13]. This objective lens is composed a monolithic fused silica and two mirrors by the vacuum deposition of aluminum onto the fused silica surface. Usual objective lens is normally placed out of cryostats because the objective lens cannot stand up in liquid helium. However, separating between sample placed into cryostat and objective lens placed out of cryostat occurs lack of stability. Imaging has an error from moving between the sample and the lens directly. Figure 1.8 shows a case that an objective lens is placed outside of a cryostat and another case that an objective lens is held with sample holder placed in a cryostat. In the latter case, imaging error reduced to $1/M$, where $M$ is magnification of the microscope, because sample plane is magnified immediately and holder moving is observed relative small. In order to decrease error less than 1 nm, sample and objective lens is necessary to be held by one monolithic holder. We need a lens for using cryogenic condition, thus the cryo-resistant objective reflecting lens is developed. The image stability increases to $< 1/10$ nm in our microscope using monolithic holder having sample and the reflecting lens [10]. In this study, we adopted INAGAWA objective mirror, whose photo is shown in Fig. 1.9 . INAGAWA mirror [12] used has higher optical performance such as NA of 0.99 in superfluid helium (refractive index $n$ of 1.027 [30]) and 0.96 in air because the lens has aspherical and spherical mirror. This lens is suitable for localization of fluorophores because the higher NA causes decreasing optical resolution (see Eq. 1.1 and Eq. 1.3).

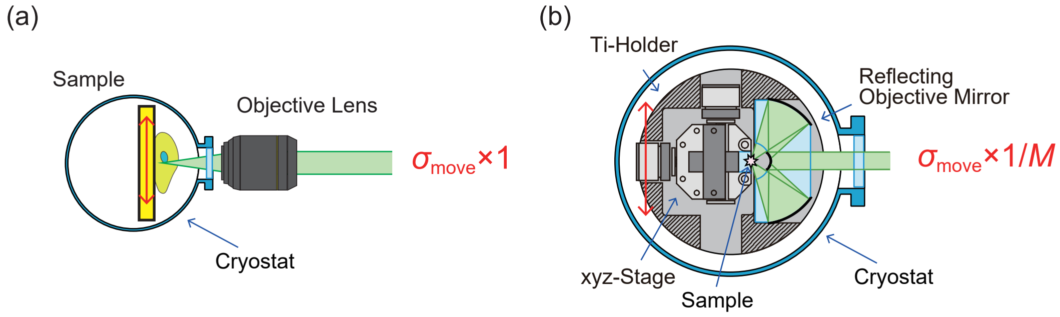

Figure 1.8 Positions of sample and lens and drift error of the sample. In usual cryogenic fluorescence microscope as (a), objective lens is placed out of cryostat because normally objective lens cannot be frozen. When the sample moves $\sigma_{\mathrm{move}}$ , image has error $\sigma_{\mathrm{move}}$. In (b), imaging error reduced to $\sigma_{\mathrm{move}}/M$, where $M$ is magnification because the sample fluorescence is immediately magnified.

## 1.6 Problems and solution in molecular level imaging

Previous studies have not achieved molecular imaging yet because of sample moving, microscope vibration, aberration of optics, and so on. The problems for achievement of cellular molecules imaging with nanometer accuracy using cryogenic far-field fluorescence microscope are (1) sample moving, (2) microscope moving, (3) aberration of optics, (4)

Figure 1.9 A photograph of INAGAWA objective mirror. The diameter of INAGAWA mirror is about 3 cm. This lens has higher optical performance because of inside mirror having aspherical surface.

background noise (5) shot noise, (6) blinking noise, and (7) molecular dipole orientation effect. Here I describe problems and solution strategies detailed as following.

### 1.6.1 Thermal drift of cryogenic stage

Moving of sample is detected directly. This problem is solved by cryogenic immobilized technique, which applies for cryo-EM using liquid ethane not to destroy biomolecules [2]. We consider that cryogenic fluorescence microscopy adopts this immobilization technique. In this thesis, sample fluorophores are frozen into superfluid helium. Superfluid helium is cryogenic temperature, does not appear babbles, and does not obstruct imaging. Moreover, its temperature can be controlled without difficulty because superfluid helium has high heat conductivity. Thermal control achieves 0.2 mK of standard deviation using cooling by a vacuum pump and a PID controlled thermal resistance. This 0.2 mK of standard deviation is enough for molecular imaging because optical drift is assessed occurred by thermal changing 1 μm/K. Furthermore, the sample holder moving should be care as Fig. 1.8 (mentioned in 1-4-5).

### 1.6.2 Vibration and drift of microscope

Longtime observation requires longtime stability of microscope. The reasons of microscope moving are air drift as wind and temperature changing. Figure 1.10 shows photographs of stabilized microscope. The airtight stainless-steel boxes of Fig. 1.10 (a, b) block the flow of air. The boxes are placed in a black aluminum box that light-shielding and airtight (see Chapter 2). Temperature changing causes image drift because the minor expansion and contraction of microscope. The cryostat is tall; hence weak for temperature changing in my microscope. In order to control the wall of cryostat temperature, silicon tube is coiled around the wall and water is pouring in the tube. Moreover, the babble wrap covers silicone tube coiled (see Chapter 3).

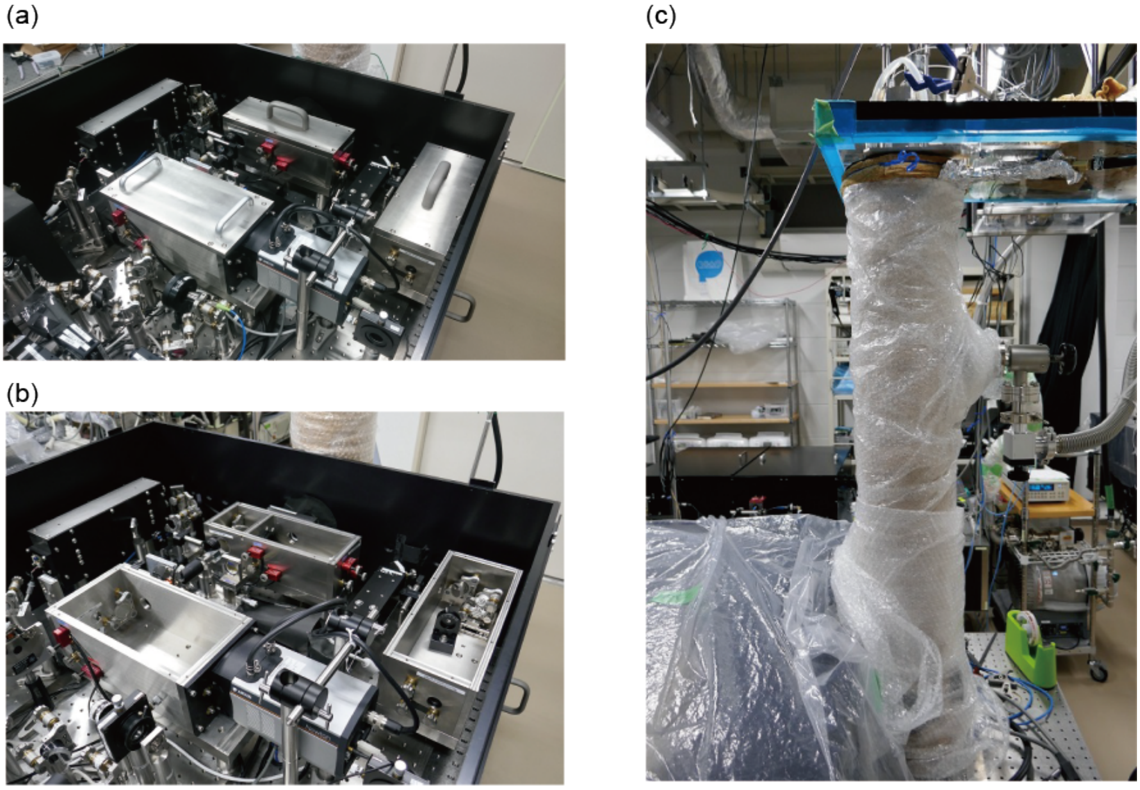

Figure 1.10 Photographs of stabilized cryogenic fluorescence microscope. (a, b) Mirrors are held by the airtight stainless-steel boxes not to shake. (a) denotes the photograph when a cover is closed, and (b) denotes when a cover is off. (Detail is described in Chapter 2.) (c) is the picture of when the wall of cryostat is isolated from the room temperature. (Detail is described in Chapter 3.)

### 1.6.3 Aberrations

In optics, aberration is a property of optical system such as lens which causes light spread out of a point on focus. There are two main types; one is mono-chromatic aberrations and the other one is chromatic aberrations. An objective lens gives mainly mono-chromatic aberrations to microscope. In our microscope, INAGAWA mirror is developed by our laboratory in order to put into cryostat (Fig. 1.9). This lens has higher optical performance, however its field of diameter is 3 μm, which is very small [12]. When observing out of the field diameter, the image has much distortion caused by mono-chromatic aberration. Accordingly, sample scanning takes wide field image using $xyz-$piezo stage. The chromatic aberration is caused by wavelength dependence of refraction index. We developed reflecting microscope using flat and concave mirrors.

### 1.6.4 Background from autofluorescence

Single molecule fluorescence is weak; hence background noise disturbs localization individual fluorophore with molecular precision. In this thesis, we consider that background light is reduced using red and NIR dye for fluorescence imaging. Most of fluorescent biomolecules absorb light of wavelength < 500 nm and emit fluorescence of < 600 nm [31]. Red or NIR light are good at cellular imaging because they are not much absorbed and emitted. Therefore, we adopted red dye for instance ATTO647N and ATTO655, and NIR dye for instance Alexa Fluor 750 and sulfo-Cyanine 7.

### 1.6.5 Shot noise

A fluorescence image of single molecule has width whose size is about wavelength called Airy disk such as Fig. 1.11, which is an individual ATTO647N molecule. The position of single molecule is localized from this image. The precision of localization has shot noise depended photon numbers that are distributed probably for point-spread-function (PSF). The precision $\Delta_{\text{photon}}$ is described following equation, [23]

$$\Delta_{\text{photon}} = \frac{s_{\text{disk}}}{\sqrt{N_{\text{disk}}}}, \tag{1.4}$$

where $s_{\text{disk}}$ is width of standard deviation of Airy disk and $N_{\text{disk}}$ is photon number in Airy disk. $s_{\text{disk}}$ equals 139 nm when the image of ATTO647N whose fluorescent wavelength is about 680 nm using INAGAWA mirror. $\Delta_{\text{photon}}$ less than 1 nm requires $N_{\text{disk}} > 1.9 \times 10^4$. Furthermore, localization for light axis direction requires more photons because the resolution of light axis is worse than lateral direction. Stability of microscope during gathering photons to localization is necessary for molecular level imaging. Moreover, not to bleach fluorophore is important for molecular level imaging. Some fluorescent molecules are less likely to bleach at cryogenic temperature.

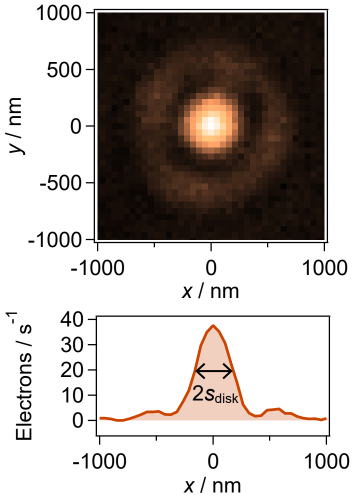

Figure 1.11 Fluorescence image of ATTO647N individual molecule using CCD camera. The accumulation time is 4 second. The width of standard deviation $s_{\mathrm{disk}}$ is 139 nm in this image. When localization the position of molecules, Gaussian function fitting determines the center of gravity as the position.

### 1.6.6 Blinking noise of single fluorophore

Blinking of single fluorophore disturbs localization with high precision under a system of imaging used single detector such as confocal imaging. Figure 1.12 shows blinking fluorophore image obtained by sample scanning. Photon number in the Airy disk is almost same as Fig. 1.11, however the localization error is deteriorated. This blinking process is explained Fig. 1.13 diagram, which shows molecular absorption process. When the fluorophore absorbs excitation light, it emits fluorescence for the most part, however intersystem crossing to triplet state rarely occurs and the state has long lifetime. The image of Fig. 1.12(a) has blinking noise not only shot noise because each pixel of this image differs in timing as Fig 1.12(b). To avoid this blinking noise, molecular level image is obtained by 2D detector, which ignores the blinking noise according to same time the light entering each pixel.

### 1.6.7 Systematic error due to the dipole orientation effect

Fluorescence is dipole radiation, which is not isotropic radiation. Several studies reported that mislocalization is caused by distortion of image due to the dipole orientation effect [15, 16]. Not only that others studies reported that PSF from single fluorophore is tilted by dipole radiation as shown Fig. 1.14 [18, 19]. When light dradiation is perpendicular to

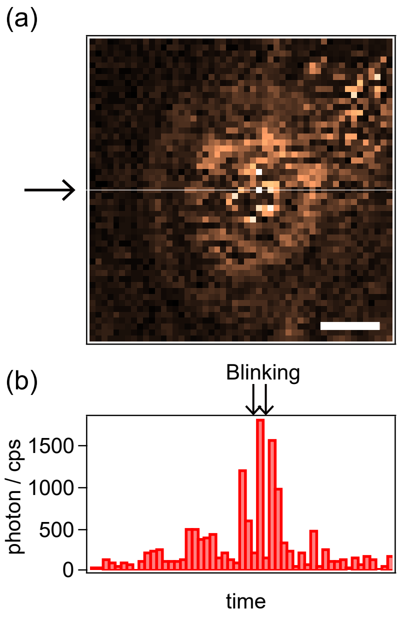

Figure 1.12 The result of ATTO647N imaging using avalanche photodiode (APD). (a) Fluorescence image of $2.5 \times 2.5$ µm$^2$ with sample scanning. Accumulation time on single pixel is 0.05 second. The scale bar is 0.5 µm. (b) Each detecting count of photons during scanning area of the arrow in (a).

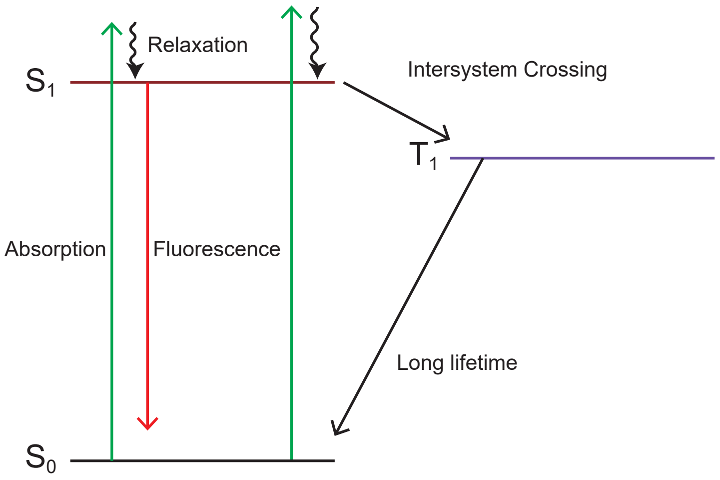

Figure 1.13 A Jablonski diagram of a blinking fluorescent molecule. Blinking is caused by intersystem crossing to long lifetime state rarely occurs.

light axis, the focusing light is gathered on the principal ray (shown top of Fig. 1.14). On the other hand, the focusing light is tilted from the principal ray when the radiation is anisotropic like dipole radiation (shown bottom if Fig. 1.14). Image of 3D-PSF is obtained to grasp the dipole orientation direction which is fixed at cryogenic temperature. By correcting the dipole orientation effect from 3D-PSF, molecular accuracy imaging can be obtained.

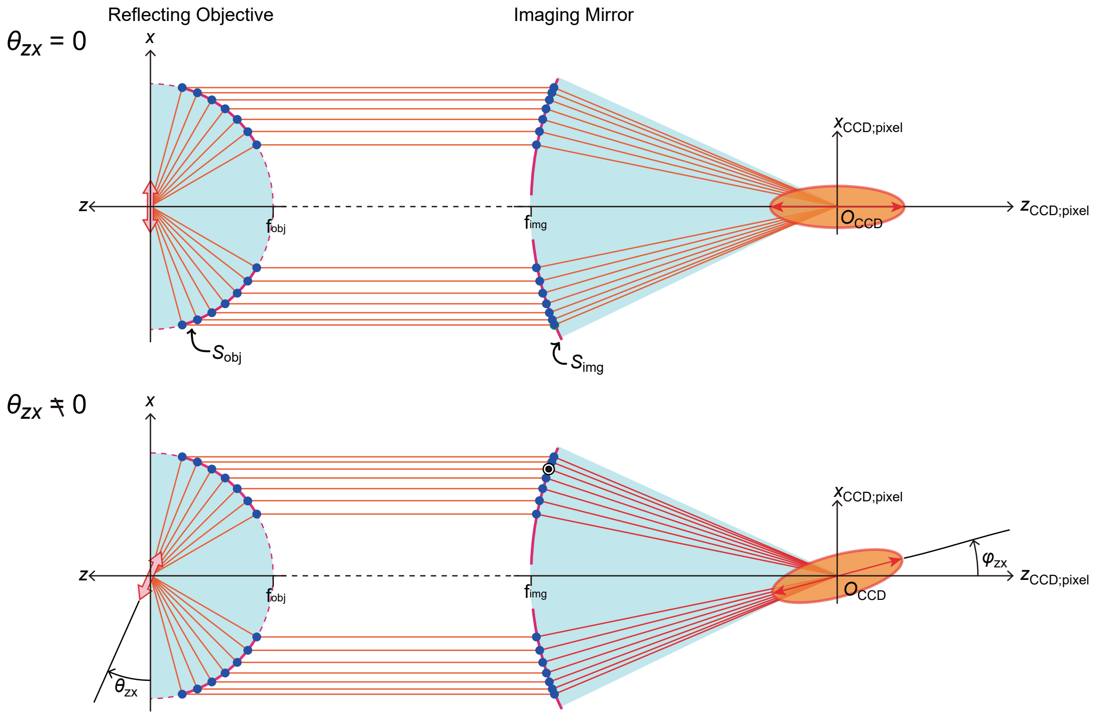

Figure 1.14 The relation between dipole direction and imaging PSF. (Top) When light radiation is perpendicular to light axis, the focusing light is gathered on the principal ray. (Bottom) The focusing light is tilted from the principal ray when the radiation is anisotropic like dipole radiation. Mislocalization is caused by a $z$-dependent $xy$-shift due to the dipole orientation effect.

## Reference List

[1] B. Ho, A. Baryshnikova and G. W. Brown: “Unification of protein abundance datasets yields a quantitative saccharomyces cerevisiae proteome”, Cell Systems, **6**, 2, pp. 192–205 (2018).

[2] R. Fernandez-Leiro and S. H. Scheres: “Unravelling biological macromolecules with cryo-electron microscopy”, Nature, **537**, 7620, pp. 339–346 (2016).

[3] K. Wüthrich: “Protein structure determination in solution by nuclear magnetic resonance spectroscopy”, Science, **243**, 4887, pp. 45–50 (1989).

[4] A. Merk, A. Bartesaghi, S. Banerjee, V. Falconieri, P. Rao, M. I. Davis, R. Pragani, M. B. Boxer, L. A. Earl, J. L. Milne, et al.: “Breaking cryo-EM resolution barriers to facilitate drug discovery”, Cell, **165**, 7, pp. 1698–1707 (2016).

[5] W. E. Moerner and L. Kador: “Optical detection and spectroscopy of single molecules in a solid”, Physical Review Letters, **62**, 21, pp. 2535–2538 (1989).

[6] M. Orrit and J. Bernard: “Single pentacene molecules detected by fluorescence excitation in a *p*-terphenyl crystal”, Physical Review Letters, **65**, 21, pp. 2716–2719 (1990).

[7] L. Schermelleh, R. Heintzmann and H. Leonhardt: “A guide to super-resolution fluorescence microscopy”, The Journal of Cell Biology, **190**, 2, pp. 165–175 (2010).

[8] S. W. Hell and J. Wichmann: “Breaking the diffraction resolution limit by stimulated emission: stimulated-emission-depletion fluorescence microscopy”, Optics Letters, **19**, 11, pp. 780–782 (1994).

[9] M. J. Rust, M. Bates and X. Zhuang: “Sub-diffraction-limit imaging by stochastic optical reconstruction microscopy (STORM)”, Nature Methods, **3**, 10, pp. 793–796 (2006).

[10] T. Hinohara, Y. I. Hamada, I. Nakamura, M. Matsushita and S. Fujiyoshi: “Mechanical stability of a microscope setup working at a few kelvins for single-molecule localization”, Chemical Physics, **419**, pp. 246–249 (2013).

[11] M. Fujiwara, S. Fujiyoshi and M. Matsushita: “Single-component reflecting objective for ultraviolet imaging and spectroscopy at cryogenic temperature”, Journal of the Optical Society of America B, **26**, 7, pp. 1395–1399 (2009).

[12] H. Inagawa, Y. Toratani, K. Motohashi, I. Nakamura, M. Matsushita and S. Fujiyoshi: “Reflecting microscope system with a 0.99 numerical aperture designed for three-

dimensional fluorescence imaging of individual molecules at cryogenic temperatures", Scientific Reports, **5**, p. 12833 (2015).

[13] M. Fujiwara, T. Ishii, K. Ishida, Y. Toratani, T. Furubayashi, M. Matsushita and S. Fujiyoshi: "Aberration-corrected cryogenic objective mirror with a 0.93 numerical aperture", Applied Physics Letters, **115**, 3, p. 033701 (2019).

[14] H. P. Kao and A. Verkman: "Tracking of single fluorescent particles in three dimensions: use of cylindrical optics to encode particle position", Biophysical Journal, **67**, 3, pp. 1291–1300 (1994).

[15] A. P. Bartko and R. M. Dickson: "Imaging three-dimensional single molecule orientations", The Journal of Physical Chemistry B, **103**, 51, pp. 11237–11241 (1999).

[16] J. Enderlein, E. Toprak and P. R. Selvin: "Polarization effect on position accuracy of fluorophore localization", Optics Express, **14**, 18, pp. 8111–8120 (2006).

[17] F. Aguet, S. Geissbühler, I. Märki, T. Lasser and M. Unser: "Super-resolution orientation estimation and localization of fluorescent dipoles using 3-D steerable filters", Optics Express, **17**, 8, pp. 6829–6848 (2009).

[18] J. Engelhardt, J. Keller, P. Hoyer, M. Reuss, T. Staudt and S. W. Hell: "Molecular orientation affects localization accuracy in superresolution far-field fluorescence microscopy", Nano Letters, **11**, 1, pp. 209–213 (2010).

[19] M. P. Backlund, M. D. Lew, A. S. Backer, S. J. Sahl, G. Grover, A. Agrawal, P. Rafael and M. WE: "Simultaneous, accurate measurement of the 3d position and orientation of single molecules", Proceedings of the National Academy of Sciences of the United States of America, **109**, 47, pp. 19087–19092 (2012).

[20] M. D. Lew and W. Moerner: "Azimuthal polarization filtering for accurate, precise, and robust single-molecule localization microscopy", Nano Letters, **14**, 11, pp. 6407–6413 (2014).

[21] K. I. Mortensen, J. Sung, H. Flyvbjerg and J. A. Spudich: "Optimized measurements of separations and angles between intra-molecular fluorescent markers", Nature Communications, **6**, p. 8621 (2015).

[22] K. I. Mortensen, J. Sung, J. A. Spudich and H. Flyvbjerg: "How to measure separations and angles between intramolecular fluorescent markers", Methods in Enzymology, Vol. 581, Elsevier, pp. 147–185 (2016).

[23] R. E. Thompson, D. R. Larson and W. W. Webb: “Precise nanometer localization analysis for individual fluorescent probes”, Biophysical journal, **82**, 5, pp. 2775–2783 (2002).

[24] S. Inoué: “Foundations of confocal scanned imaging in light microscopy”, Handbook of biological confocal microscopy (secon edition), Springer, pp. 1–17 (1995).

[25] A. Bloeß, Y. Durand, M. Matsushita, H. Van Dermeer, G. Brakenhoff and J. Schmidt: “Optical far-field microscopy of single molecules with 3.4 nm lateral resolution”, Journal of Microscopy, **205**, 1, pp. 76–85 (2002).

[26] E. Betzig, G. H. Patterson, R. Sougrat, O. W. Lindwasser, S. Olenych, J. S. Bonifacino, M. W. Davidson, J. Lippincott-Schwartz and H. F. Hess: “Imaging intracellular fluorescent proteins at nanometer resolution”, Science, **313**, 5793, pp. 1642–1645 (2006).

[27] H. Tabe, K. Sukenobe, T. Kondo, A. Sakurai, M. Maruo, A. Shimauchi, M. Hirano, S.-n. Uno, M. Kamiya, Y. Urano, M. Matsushita and S. Fujiyoshi: “Cryogenic fluorescence localization microscopy of spectrally selected individual FRET pairs in a water matrix”, The Journal of Physical Chemistry B, **122**, 27, pp. 6906–6911 (2018).

[28] S. Weisenburger, D. Boening, B. Schomburg, K. Giller, S. Becker, C. Griesinger and V. Sandoghdar: “Cryogenic optical localization provides 3D protein structure data with angstrom resolution”, Nature Methods, **14**, 2, pp. 141–144 (2017).

[29] R. Zondervan, F. Kulzer, M. A. Kol’chenk and M. Orrit: “Photobleaching of rhodamine 6G in poly (vinyl alcohol) at the ensemble and single-molecule levels”, The Journal of Physical Chemistry A, **108**, 10, pp. 1657–1665 (2004).

[30] E. Burton: “Refractive indexes of helium I and II”, Nature, **140**, p. 1015 (1937).

[31] J. R. Lakowicz: “Principles of fluorescence spectroscopy”, Springer Science, New York, third edition (2006).

# Chapter 2

# 3D localization of individual fluorophores with angstrom precision

The contents of this chapter is were prepared from the journal of our group.

Taku Furubayashi, Kazuya Motohashi, Keisuke Wakao, Tsuyoshi Matsuda, Isao Kii, Takamitsu Hosoya, Nobuhiro Hayashi, Mahito Sadaie, Michio Matsushita, and Satoru Fujiyoshi

“ Three-dimensional localization of individual fluorescent molecule with angstrom precision ” *Journal of the American Chemical Society* **139**, 8990 – 8994 (2017)

## 2.1 Introduction

In living cells, biological functions are regulated cooperatively by various biomolecules. Visualizing the three-dimensional (3D) arrangements of molecules is the first step toward understanding the molecular mechanism of such cooperative regulation. The candidates for the methods to visualize the interior of cells with the molecular resolution are cryogenic (cryo-) electron tomography of mechanically sliced cell sections [1] and optical localization microscopy of individual fluorescent molecules [2]. Among the imaging methods for cells, cryoelectron tomography has the highest 3D spatial resolution. In cryo-electron tomography, living cells are vitrified, i.e., rapidly frozen below a glass-transition temperature. Thus, the native state of the living cells is almost preserved in the vitrified cells. The near native state can be imaged with any desired precision using any desired long accumulation time because the molecules in the cells are perfectly immobilized. Three-dimensional visualization using cryo-electron tomography has played important roles in the life sciences. However, the resolution of cryo-electron tomography (4 - 5 nm) is still insufficient for identification of molecular species. Another limitation of cryo-electron tomography of cells is that the mean free path of the electrons limits the maximum thickness of the sample specimen to 0.5 - 1 μm. Because mammalian cells are typically $\sim$ 10 μm thick, most cells must be mechanically sliced into thin sections. By contrast, localization microscopy does not face the aforementioned difficulties. First, when target biomolecules are labeled with a small fluorescent molecule, i.e., a fluorescent dye or a fluorescent protein, localization microscopy can be used to visualize the distribution of the target molecules in living cells as a distribution of the fluorescence of the labeled fluorescent molecules [3]. Second, the localization microscopy can capture optical section images of an entire cell without mechanical slicing [4]. Excitation and detection in localization microscopy are performed using only visible light. Because visible light is transmitted through whole mammalian cells, the lateral ($xy$-) section images of the cells can be optically obtained at the desired axial ($z$-) position. However, the 3D standard error of the localization microscopy of individual fluorescent molecules at room temperature is 10 - 15 nm even for fixed cells [5]. The localization error in living cells is more than threefold greater than in fixed cells [6]. In comparison with the fluorescence from fluorescent beads or quantum dots, that from small molecules is very weak; consequently, a long accumulation time is required. Therefore, at room temperature, 3D localization precision is determined by the movement of the target molecules over a finite exposure time. If a target molecule is perfectly immobilized on the sample surface, the $xy$-localization error of $\sim$ 1 nm has been demonstrated to be achievable even at room temperature [7–9]. Under cryogenic conditions, a fluorescent molecule is perfectly immobilized. In addition, a molecule becomes more stable against photobleaching [10–12]. In lateral ($xy$-) directions, the standard error of the cryo-localization microscopy of individual fluorescent molecules reached 3.4 nm in 2002 [13]. Recently, the $xy$-localization error has been further improved to molecular level [12, 14–16]. In axial ($z$-) directions for individual fluorescent molecules, the localization precision under cryogenic conditions has still remained at 100 nm since 1998 [17]. As an alternative to making a precise measurement of $z$-position, Weisenburger et al. has derived a 3D average position (probability densities) from thousands of 2D ($xy$-) projection images of individual molecules by assuming a single conformation common to all the molecules [16]. For visualizing individual 3D molecular arrangement and conformation, the localization error of an individual molecule must be at a molecular level in all three directions.

Here, I present cryo-localization microscopy for an individual fluorescent molecule (ATTO647N) with angstrom precision in all the three directions. Over the past decade, we have developed cryo-reflecting microscopes for single-molecule fluorescence imaging and spectroscopy [11, 18–23]. The key optics to realize the high-precision 3D imaging in the present work is the reflecting objectives developed by our laboratory. In conventional cryo-microscopes, a sample is cooled and an objective lens is placed outside the cryostat at room temperature [24] because commercial objective lenses do not function at cryogenic temperatures. In this separate configuration of the objective lens and the sample, the thermal drift of the sample against the objective degrades the imaging stability to a few hundred nanometers. By contrast, our reflecting objective does function under a cryogen below a glass transition temperature [11, 18]. The sample and the reflecting objective are mounted onto a cryogenic insert holder and immersed in superfluid helium, which is an excellent cryogen for high-spatial-resolution microscopy [25]. Using the single-component configuration, the image passively stabilized to <1 nm/10 min [26]. In the present work, the passive stabilization was further improved. The cryogenic insert is chiefly composed of titanium (see Fig. 2.1a and Fig. 2.1b) to passively avoid the uneven thermal expansion of different materials (see Fig. 2.1d). In addition to this passive stabilization, the stage position was actively stabilized with three capacitive sensors, and the temperature near the sample was actively controlled by within a 0.24 mK standard deviation (time interval = 1.5 s in 30 min). Consequently, the imaging stability of the cryo-reflecting microscope reached a 0.05 nm standard deviation (time interval = 64 s in 13 min). Furthermore, the imaging quality was also improved. By introducing an aspherical mirror to the reflecting objective, the numerical aperture (NA) of the reflecting objective increased to 0.99, which is almost the maximal NA in superfluid helium (NA = 1.027) [23]. Compared with the $xy$-localization error, which is proportional to $\mathrm{NA}^{-1}$, the $z$-localization error is proportional to $\mathrm{NA}^{-2}$; hence, the final NA of 0.99 is vital for expanding the precise localization from 2D to 3D.

In Fig. 2.2, a localization error $\Delta r$ of 1 nm is compared to the size of a fluorescent protein. Figure 2.2a shows the simulation of the cryo-localization microscopy for an individual fluorescent molecule. Under the assumption that the standard error of the localization microscopy ($\Delta r$) follows a Gaussian distribution, the 50 localization points (pink marks) were generated from Gaussian noise. As evident in Fig. 2.2a, most localization points fall within a sphere with a radius $2\Delta r$ centered at the fluorescent molecule. When $\Delta r$ is 1 nm, the $2\Delta r$ sphere is comparable to the size of a fluorescent protein (Fig. 2.2). Therefore, in the present work, we use a $\Delta r$ of <1 nm as a measurement of the molecular precision.

I checked that localization with less than 1 nm precision is realizable using optical simulation. After the simulation, I demonstrated localization with angstrom precision at experiment.

## 2.2 Optical simulation

### 2.2.1 Setup of optical simulation

The optical simulation of the cryo-reflecting microscope for the $xy$- and $z$-localization of an individual fluorescent molecule was performed using a commercial optical design software (Zemax Optic Studio 15.5). The optical layout of the simulated microscopic system is shown in Fig. 2.3a at $xy$- and Fig. 2.4a at $z$-localization. A fluorescent molecule is much smaller in size than the PSF of its fluorescence; therefore, the fluorescence of the fluorescent

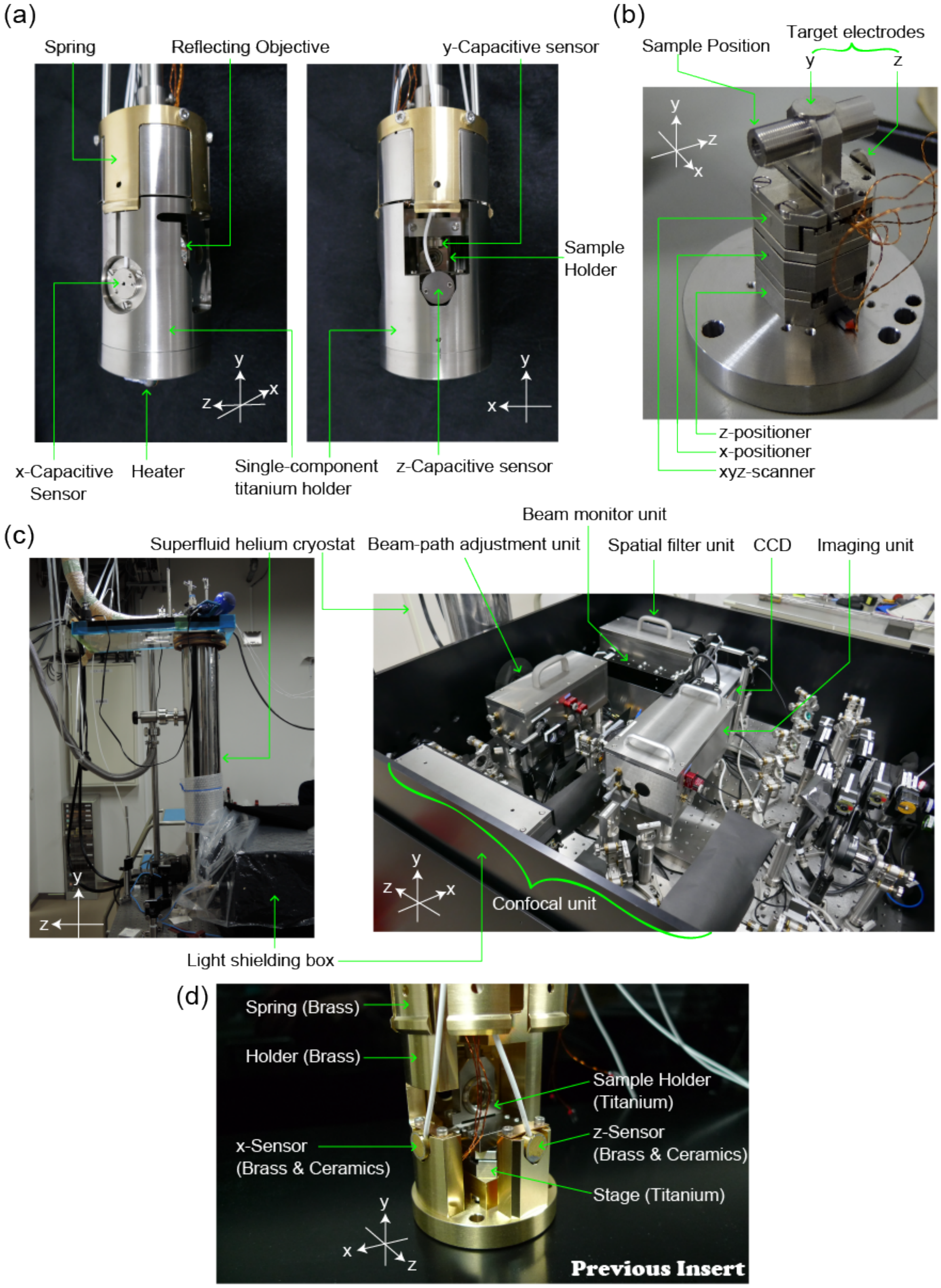

Figure 2.1 Photographs of the cryo-reflecting microscope. The head of the superfluid helium insert (a), the sample holder and cryogenic piezo-driven stages (b), and the overhead view of the cryo-reflecting microscope (c). To suppress thermal drift, the insert head (a, b) was composed chiefly of titanium. (d) The previously reported cryo-insert holder [23].

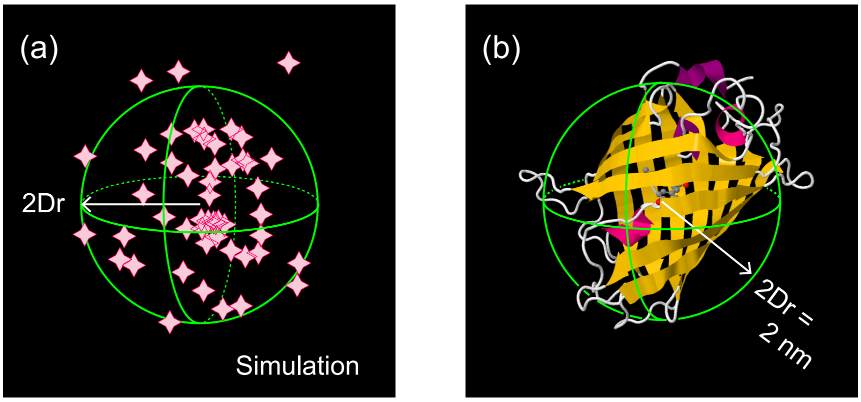

Figure 2.2 Concepts of cryo-localization microscopy. (a) Simulation of localization microscopic measurements of an individual fluorescent molecule with standard error $\Delta r$. A sphere with radius $2\Delta r$ centered at the individual fluorescent molecule is shown in the green. (b) Comparison of the localization error $\Delta r = 1$ nm and the size of a fluorescent protein (PDB code 1EMA).

molecule was regarded as an isotropic emission from a point source. To express the point source, the system aperture type was set to "Object Space NA = 0.96" and the apodization type was set to "Cosine Cubed, factor = 0". The polarization was linear along the $x$-axis. The wavelength was 705 nm. The detailed design of the reflecting objective has been reported [23]. A Huygens PSF was used with a pupil sampling of 128 × 128 and the image sampling of 128 × 128. The pixel size of the obtained image ( " Image Delta " ) was 26 μm, which is the same as that of the CCD camera used.

### 2.2.2 Simulation results of $xy$-localization

We carried out optical simulations for the cryo-reflecting microscope for $xy$-localization. The optical layout of the simplified setup used in the simulation is shown Fig. 2.3a. An individual fluorescent molecule is located at the focal point of an objective. The fluorescence of the individual fluorescent molecule is collected by the reflecting objective and focused by a combination of a concave mirror. The $xy$-centroids were evaluated from of a bright disk in PSF using a weighted least-squares fitting of 2D Airy function,

$$I(r) = I_0 \left[ \frac{2J_1(R)}{R} \right]^2 , \tag{2.1}$$

$$R = 1.22\pi\sqrt{\frac{(x-x_0)^2}{R_x^2}+\frac{(y-y_0)^2}{R_y^2}}, \tag{2.2}$$

$$s_x = 0.324R_x, \quad s_y = 0.324R_y, \tag{2.3}$$

where $x_0$ and $y_0$ are fixed molecular positions, $s_x$ and $s_y$ are width of the standard deviation of Airy disk, and $R_x$ and $R_y$ are distance between the center and the dark ring. The number of fluorescence photons inside the bright disk ($N_{\text{disk}}$) is expressed by $N \times \text{EE}_{1\text{st}}$, where $\text{EE}_{1\text{st}}$ is an encircled energy inside the first dark ring. The theoretically predicted $xy$-localization error ($\Delta_{xy}$) can be expressed by [27].

$$\Delta_{xy} = \sqrt{\frac{{s_{xy;\text{disk}}}^2 + \frac{a^2}{12}}{N_{\text{disk}}} + {\delta_{xy;\text{drift}}}^2 + {\delta_{xy;\text{back}}}^2}, \tag{2.4}$$

where a is the pixel size in the image (53 nm). From the optical simulation of PSF, the theoretical values are $\text{EE}_{1\text{st}} = 0.40$ and $s_{xy;\text{disk}} = 109$ nm. The simple case of $\delta_{z;\text{drift}}$ and $\delta_{z;\text{back}} = 0$ gives the equation,

$$\Delta_{xy} \cong A_{xy}\frac{s_{xy;\text{disk}}}{\sqrt{N}} \tag{2.5}$$

The proportional coefficient for the $xy$-localization in theory $A_{xy}^{\text{theory}}$ was 1.6. The photon noise was assumed to follow a Poisson distribution. The $xy$-localization error $\Delta_{xy}$ was simulated as a function of $N$ (pink circles in Fig. 2.3e). The simulated errors (pink circles) are in good agreement with the theoretical curve (black curve). The proportional coefficient for the $xy$-localization in the simulation ($A_{xy}^{\text{sim.}}$) was evaluated as 1.7.

### 2.2.3 Simulation results of $z$-localization and discussion

We carried out optical simulations for the cryo-reflecting microscope for $z$-localization. For $z$-localization using an off-focus imaging technique [28, 29], a singlet lens was inserted into the optical path; hence the focal plane shifted from the CCD camera. The optical layout of the simplified setup used in the simulation is shown in Fig. 2.4a. An individual fluorescent molecule is located at the focal point of an objective. The fluorescence of the individual fluorescent molecule is collected by the reflecting objective and focused by a combination of a plano-convex lens and a concave mirror. The theoretically predicted PSF of the fluores-

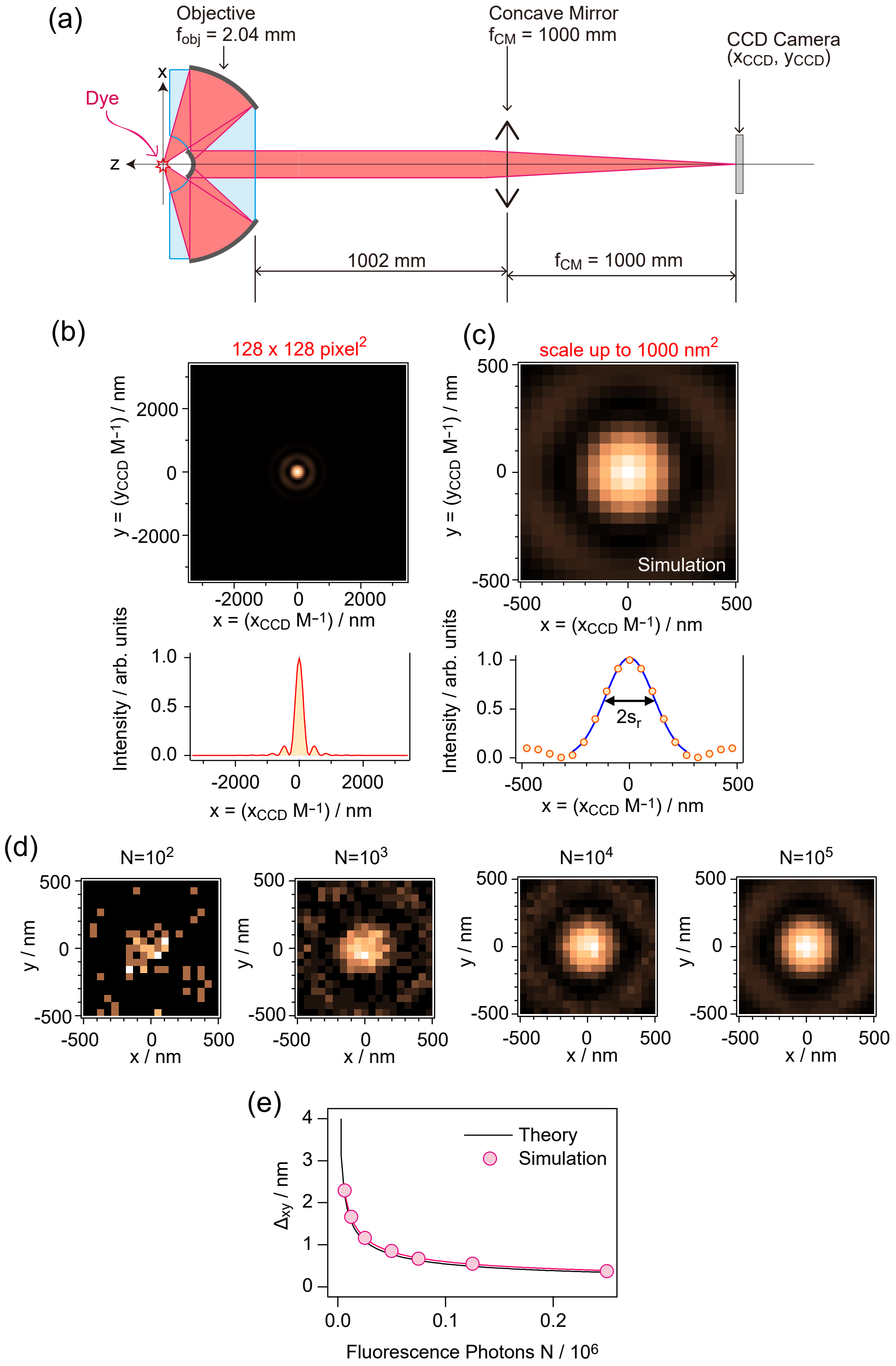

Figure 2.3 Optical simulation of PSF for fluorescence of an individual molecule in the *xy*-localization experiment. (a) Optical layout of the simplified cryo-reflecting microscope for the optical simulation of the *xy*-localization mode. (b) Simulated PSF on the CCD camera. The horizontal and vertical axes are the CCD position ($x_{\mathrm{CCD}}, y_{\mathrm{CCD}}$) divided by the magnification of the cryo-reflecting microscope (M = 490). (c) Scale up from the image of b to 1000 nm$^2$. The PSF resembles a Gaussian function (blue curve). (d) Poisson-noised images of the fluorescence photons $N = 10^2, 10^3, 10^4, \mathrm{and} 10^5$. (e) Optical simulation for the localization error for $\Delta_{xy}$ as a function of $N$ (colored circles). The theoretical curve is depicted by a black curve.

cence of the individual fluorescent molecule on the CCD detector is shown in Fig. 2.4b. The bright central disk appears with concentric bright rings. The defocused PSF image depends not only on the $z$-position of the fluorescent molecule but also on the wavelength of fluorescence ($\lambda_{\text{fluo}}$). To exclude the diffraction pattern, the pixels of the PSF of 128 × 128 pixel$^2$ (Fig. 2.4b) was binned to obtain the PSF of 12 × 12 pixel$^2$ (Fig. 2.4c). The focal length of the additional lens (5000 mm) was chosen from the commercially available lenses so that the 10 × 10-binning fluorescence image (Fig. 2.4c) was best fitted by a 2D Gaussian function. As seen in Fig. 2.4c, the shape of the binning image resembles a Gaussian function (blue curves).

The standard deviation of the binning image on the $xy$-plane ($s_{xy;\text{bin}}$) was evaluated using a weighted least-squares fitting of a Gaussian function. The weight is the reciprocal of the expected uncertainties in photons on each pixel. The fitting result of $s_{xy;\text{bin}}$ is linearly proportional to the $z$-position of the individual fluorescent molecule from −40 nm to 40 nm against the focal point (Fig. 2.4d). The slope ($\mathrm{d}z/\mathrm{d}s_{xy;\text{bin}}$) was 1.4. In practice, $s_{xy;\text{bin}}$ is calculated from the average of the standard deviations along the major and minor axes; thus, the $z$-localization error ($\Delta z$) is reduced by a factor of $\sqrt{2}$,

$$\Delta z = \frac{\mathrm{d}z}{\mathrm{d}s_{xy;\text{bin}}} \frac{\Delta s_{xy;\text{bin}}}{\sqrt{2}} \cong \Delta s_{xy;\text{bin}}. \tag{2.6}$$

The error $s_{xy;\text{bin}}$ is caused by the photon shot noise ($\delta z_{\text{photon}}$), the pixelation noise ($\delta z_{\text{pix}}$), the mechanical drift of the microscope ($\delta z_{\text{drift}}$), and the background noise ($\delta z_{\text{back}}$) [13, 27]. The total $z$-localization error can be expressed by

$$\Delta z \cong \Delta s_{xy;\text{bin}} = \sqrt{\delta z_{\text{photon}}{}^2 + \delta z_{\text{pix}}{}^2 + \delta z_{\text{drift}}{}^2 + \delta z_{\text{back}}{}^2} = \sqrt{\frac{s_{xy;\text{bin}}{}^2 + \frac{a_{\text{bin}}{}^2}{12}}{N} + \delta z_{\text{drift}}{}^2 + \delta z_{\text{back}}{}^2}. \tag{2.7}$$

where $a_{\text{bin}}$ is a pixel in the binning image. In the simple case of $\delta z_{\text{drift}}$ and $\delta z_{\text{back}} = 0$, $\Delta z$ is expressed by

$$\Delta z = A_z \frac{s_{xy;\text{bin}}}{\sqrt{N}}. \tag{2.8}$$

The pixel size $a_{\text{bin}}$ is the pixel size of the binned image (530 nm) and $s_{xy;\text{bin}}$ was evaluated to be 560 nm from the optical simulation in Fig. 2.4c. The theoretical proportional coefficient $A_z^{\text{theory}}$ was 1.0. We simulated the $z$-localization error ($\Delta z$) in our cryo-reflecting microscope.

The photon noise was assumed to follow a Poisson distribution. A series of Poisson-noised images was simulated with $N = 10^2, 10^3, 10^4,$ and $10^5$ (Fig. 2.5a). In the simulation of $\Delta z$, 1000 noised images were generated for each number of photons. The standard deviations of the 1000 noised images ($s_{xy;\mathrm{bin}}$) were evaluated with the weighted least-squares fitting of 2D Gaussian function. From Fig. 2.4d, the $z$-position of an individual fluorescent molecule is proportional to 1/1.4 of $s_{xy;\mathrm{bin}}$. The simulated errors for $\Delta z$ are shown as a function of $N$ (green circles in Fig. 2.5b). The proportionality factor of the simulation ($A_z^{sim.}$) in Eq.(2.8) was simulated as 1.3, which is 1.3 times the theoretically predicted factor ($A_z^{\mathrm{theory}} = 1.0$). This variance might be due to the difference between the fitting function (Gaussian) and the shape of the binning image in Fig. 2.4c. This simulation shows this localization method can achieve less than 1 nm precision when $\delta_{z;\mathrm{drift}} \ll 1$ nm, $\delta_{z;\mathrm{back}} \ll 1$ nm.

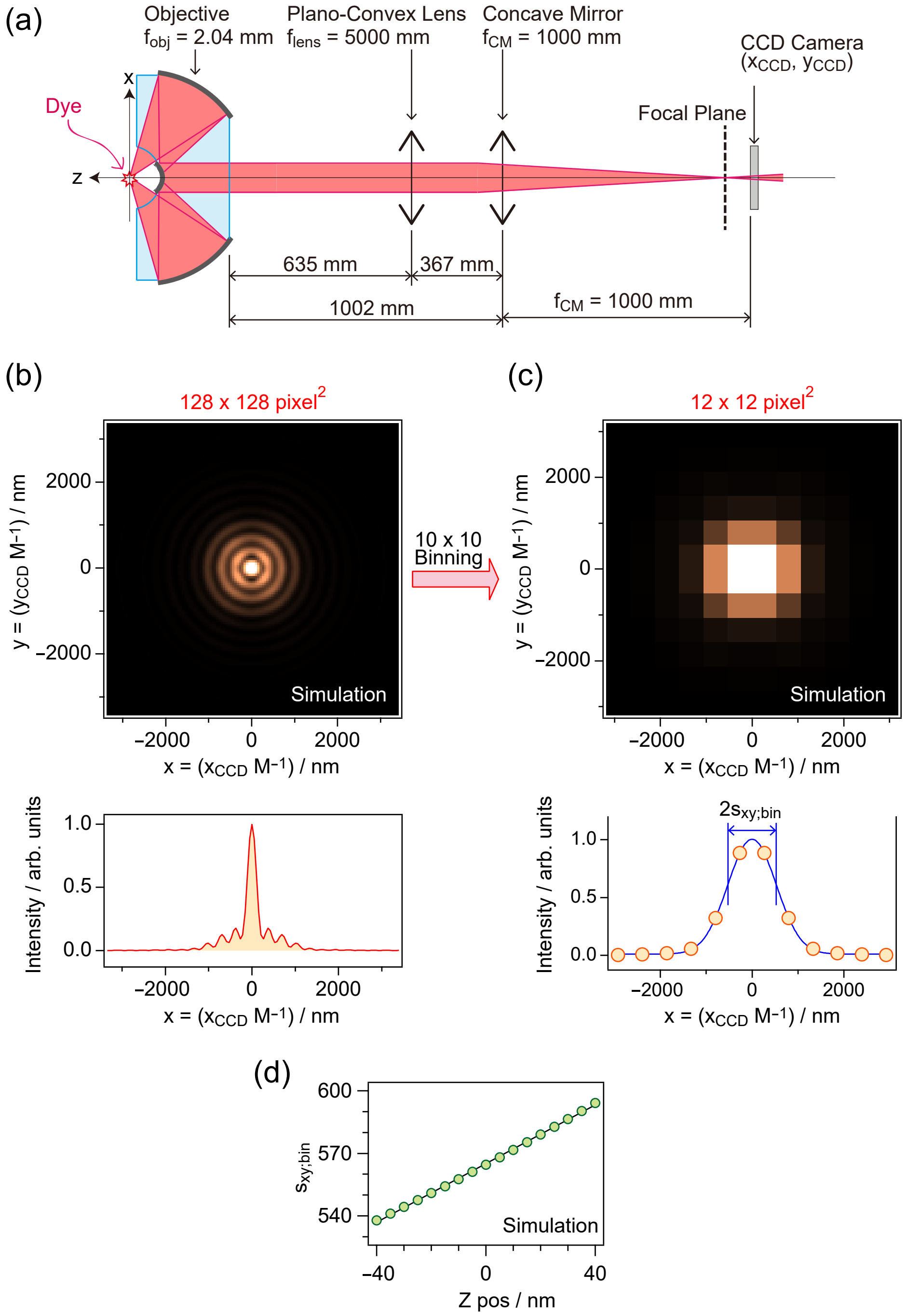

Figure 2.4 Optical simulation of PSF for fluorescence of an individual molecule in the $z$-localization experiment. (a) Optical layout of the simplified cryo-reflecting microscope for the optical simulation of the $z$-localization mode. (b) Simulated PSF on the CCD camera. The horizontal and vertical axes are the CCD position ($x_{\mathrm{CCD}}$, $y_{\mathrm{CCD}}$) divided by the magnification of the cryo-reflecting microscope ($M$ = 490). The image b was binned into 100 (10 × 10) pixels to obtain the component with low spatial frequency (c). The binned PSF resembles a Gaussian function (blue curve). (d) Standard deviation of the binned PSF ($s_{xy;\mathrm{bin}}$) shown as a function of the $z$-position of the fluorescent molecule.

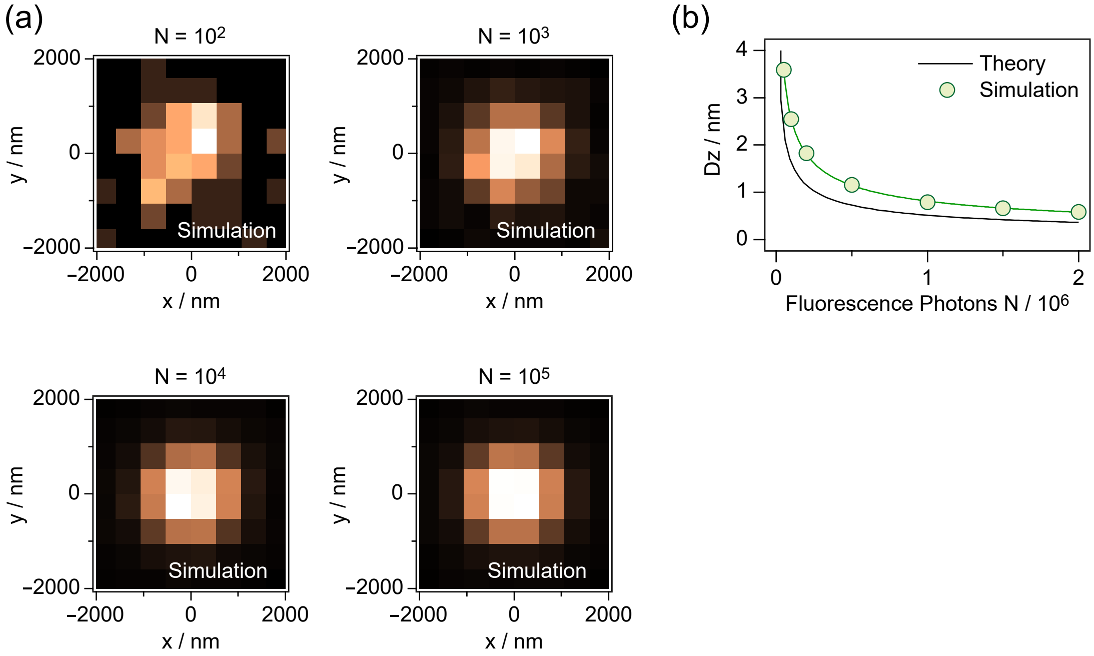

Figure 2.5 Optical simulation for the standard error of the localization of an individual fluorescent molecule. (a) Poisson-noised images of the binned PSF of an individual fluorescent molecule (Fig. 2.4c) under the conditions for the fluorescence photons $N = 10^2, 10^3, 10^4$, and $10^5$. (b) Optical simulation for the localization errors of $\Delta z$ as a function of $N$ (colored circles). The theoretical curve is depicted by a black curve.

## 2.3 Experimental setup

### 2.3.1 Cryo-reflecting microscope

Figure 2.6 shows the details of the cryo-reflecting microscope. The microscope was composed of four optical units. Reflecting optics was used in the units to avoid chromatic aberration. Excepting those in the confocal unit, the all optics in the unites were placed in an airtight stainless-steel box for mechanical stabilization (Fig. 2.1c). The four units were placed in a black aluminum box that was light-shielding and airtight.

### 2.3.2 Light source

The light source was a continuous-wave diode laser with wavelengths of 637 nm (OBIS637-140mW, Coherent). The laser lights were coupled with polarization-maintaining single-mode fibers, and the outputs were collimated by the objective lenses. The collimated laser light was spectrally filtered with a bandpass filter (Filter1; FF01-637/7, Semrock, for $\lambda_{\mathrm{ex}}$ = 637 nm).

### 2.3.3 Spatial-filter unit

The first unit was a spatial-filter unit to minimize the wave front error of a light source. The laser light was focused with the plano-convex fused-silica lens Lens1 ($f$ = 150 mm; SLSQ-25-150P, Sigma Koki) at the center of a 20-µm pinhole (PA-20, Sigma Koki). The light was diffracted through the pinhole and collimated with the silver-coated concave mirror CM1 ($f_{\mathrm{CM1}}$ = 250 mm; 10DC500ER.2, Newport). The central disk of the light was identified with an iris and propagated to the second unit.

### 2.3.4 Beam-path adjustment unit and superfluid-helium cryostat

Approximately 30% of the light was reflected by the beam-splitter BS2 (PSM25-25.4C03-10-550, Sigma Koki) and was conducted to the inside of a superfluid-helium cryostat by the second unit, a beam-path adjustment unit. The two silver-coated mirrors (M3, M4) in the second unit matched the principal ray of the laser light to the optical axis of the cryo-reflecting

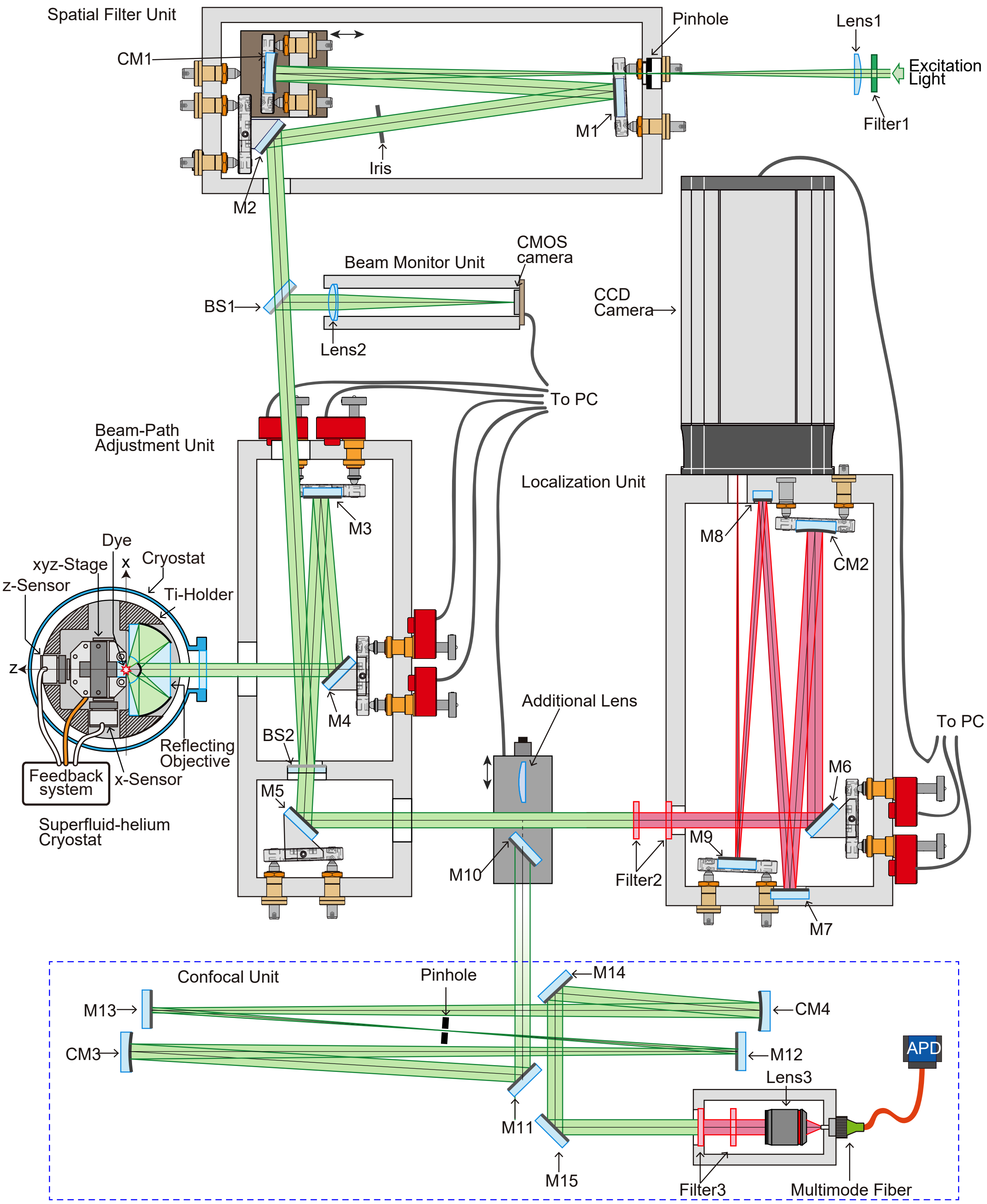

Figure 2.6 Optical arrangement of the cryo-reflecting microscope. The symbols are M1-15: silver-coated flat mirrors, BS1-2: beam splitters (T = 0.8 at $\lambda$ = 700 nm), CM1: a silver-coated concave mirror (focal length, $f$ = 250 mm), CM2-4: silver-coated concave mirrors (focal length $f$ = 1000 mm), APD: Avalanche photo-diode, CMOS: complementary metal oxide semiconductor, CCD: a charge-coupled device

objective. The tilt angles of the two mirrors were finely controlled by piezo-driven linear actuators (8301NF, Newport). The field of view of the reflecting objective is approximately 1 $\mu$m × 1 $\mu$m because of coma and spherical aberration [23]. The angle between the principal ray and the optical axis was adjusted within $3 \times 10^{-4}$ radians. The laser light was focused on the sample by the cryo-reflecting objective [23] ($f_{\text{obj}}$ = 2.04 mm, NA = 0.99 in superfluid helium). The sample position was moved finely with a piezo-driven cryo-scanner in the $xyz$ directions (the scanning range of $30 \times 15 \times 30$ $\mu$m$^3$ in the $x \times y \times z$ directions; ANSxyz100std, Attocube Systems) and coarsely with two cryo-positioners in the $xz$-directions (distance of travel = 5 mm; ANPx101, Attocube Systems). The xyz-positions of the stage ($x_{\text{stage}}, y_{\text{stage}}, z_{\text{stage}}$) were monitored with three capacitive cryo-sensors that were custom-made for cryogenic experiments (the detection range was 100 – 150 µm; Unipulse). The reflecting objective and three cryo-sensors were fixed with a single-component titanium holder (Fig. 2.1a). Components near the sample (sample holder, cryo-stages and cryo-position sensors) were chiefly composed of titanium (Figs. 2.1a and 2.1b) so that the mechanical drift due to thermal expansion was minimized. In addition to this passive stabilization, the temperature near the sample holder was controlled within 0.24 mK standard deviation using a commercial temperature controller (model 335, Lake Shore). The standard deviation was calculated from 1200 data points with the time interval = 1.5 s and the acquisition time ~ 1.5 s. The $xyz$-position of the sample stage was actively stabilized using a closed-loop feedback system with three position sensors and the cryo-scanner. Consequently, the image stability of the cryo-reflecting microscope was improved to 0.05 nm standard deviation. The standard deviation was calculated from 12 data points with the time interval = 64 s and the acquisition time ~ 64 s. The fluorescence light from an individual fluorescent molecule was collected by the reflecting objective. Approximately 70% of the fluorescence light passed through BS2. In addition, the excitation light reflected on the sample surface was conducted with BS2 to the third unit, a beam monitor unit. The light was focused on a complementary metal oxide semiconductor sensor (ARTCAM-130MI-BW, Artray). By the image, the $z$-distance between the sample and the objective was adjusted to the focal length of the objective ($f_{\text{obj}}$).

### 2.3.5 Localization and confocal unit

The cryo-reflecting microscope was operated in three modes, that is, $xy$-localization (Fig. 2.7a), $z$-localization (Fig. 2.7b), and 3D confocal raster-scanning imaging (Fig. 2.7c). In the first operating mode for the $xyz$-localization, the fluorescence light was separated from the excitation light with two notch filters (Filter2; NF03-633E; Semrock) and propagated to the third unit, the localization unit. The fluorescence light was focused on the charge-coupled device (CCD) image sensor (DU920P-BEX2-DD, Andor) with the silver-coated concave mirror CM2 ($f_{\mathrm{CM2}}$ = 1000 mm, PS-SMCC-2.00-UV, CVI). The distance between CM2 and the reflecting objective was approximately $f_{\mathrm{CM2}} + f_{\mathrm{obj}}$ = 1002 mm to image the point spread function (PSF) correctly along the axial direction. The observed fluorescence image of a fluorescent molecule (ATTO647N) is shown in Results (Fig. 2.9c). The excitation wavelength ($\lambda_{\mathrm{ex}}$) was 637 nm. The $xy$-position of the fluorescent molecule was determined from the centroid of the central disk by a weighted-least-squares fitting of an Airy function. The weight is the reciprocal of the expected uncertainties in photons on each pixel [27]. The accumulation time for one frame was 4 s, and the readout time was 3.5 s. The total number of frames obtained was 576.

In the second operating mode for $z$-localization, a long-focal-length singlet lens ($f$ = 5000 mm, antireflection-coated plano-convex BK7 lens; SLB-30-5000PIR1, Sigma Koki) was added before the light was propagated to the localization unit. The fluorescence light was focused in front of the CCD camera, and the spot was defocused on the imaging sensor (shown in Fig 2.10a). The defocused image was binned in 100 pixels (10 × 10 pixels) on the CCD chip (shown in Fig. 2.10b). The accumulation time for one frame was 8 s and the read-out time was 0.9 s. The total number of frames obtained was 576. The standard deviation of the binning image was evaluated by a weighted-least-squares fitting of 2D Gaussian function. The weight was the reciprocal of the expected uncertainties in photons on each pixel. Because the binning image was slightly elliptical due to the polarization of the fluorescence light, the $z$-position was determined from the average of the standard deviations along the major and minor axes.

In the third operating mode for 3D confocal raster-scanning imaging, the fluorescence light propagated to the fourth unit, the confocal unit with the flat mirror M9. The fluorescence light was focused on a 300-μm pinhole (P300S, Thorlabs) with a silver-coated concave mirror CM3 ($f_{\mathrm{CM3}}$ = 1000 mm; PS-SMCC-2.00-UV, CVI). In the same manner as for the localization unit, the distance between CM3 and the cryo-objective was approximately $f_{\mathrm{CM3}}$ + $f_{\mathrm{obj}}$ = 1002 mm. The fluorescence light was collimated with the silver-coated concave mirror CM4 (($f_{\mathrm{CM4}}$ = 1000 mm, PS-SMCC-2.00-UV, CVI) and separated from the excitation light with two filters (Filter3; ZET635NF, Chroma Technology, for $\lambda_{\mathrm{ex}}$ = 637 nm; NF03-658-25, Semrock) The filtered fluorescence light was coupled with a multimode fiber (core diameter = 50 µm, NA = 0.12; Fiberguide) and counted with an avalanche photodiode (SPCM-AQR16FC, Perkin Elmer). In the 3D confocal imaging, the number of fluorescence photons was plotted against the $xyz$-position of the stage. In addition, the 300-µm pinhole could be removed from the optical path. The fluorescence image in Results (Fig. 2.9b) was obtained without the pinhole.

### 2.3.6 Sample for the $xyz$-localization of an individual ATTO647N molecule

A $10^{-10}$ M solution of ATTO647N carboxylic acid (ATTO TEC) was prepared at pH = 7 in the presence of 20 mM phosphate buffer and 1.0% wt/wt polyvinyl alcohol. The solution was spin-coated on a $CaF_2$ substrate with the spinning speed of 3000 revolutions per minute (rpm) for the coat time of 60 s. Figure 2.8 shows Spectra of optical filters, laser, and ATTO647N. This fluorophore has absorption at 637 nm and fluoresce the light whose spectrum is shown right bottom of Fig. 2.8.

## 2.4 Experiments and results

### 2.4.1 Blinking

In the case of the present cryo-reflecting microscope, fluorescence images of the individual molecule were taken using a 2D multichannel detector to suppress the blinking noise of fluorescence for an individual molecule. The fluorescence of an individual fluorescent molecule often shows a repeated on/off cycle of emission called blinking (Fig. 2.9a). The blinking noise severely deteriorates the fluorescence image quality when the fluorescence signals at different positions in the image are measured at different points of time. Therefore, an image

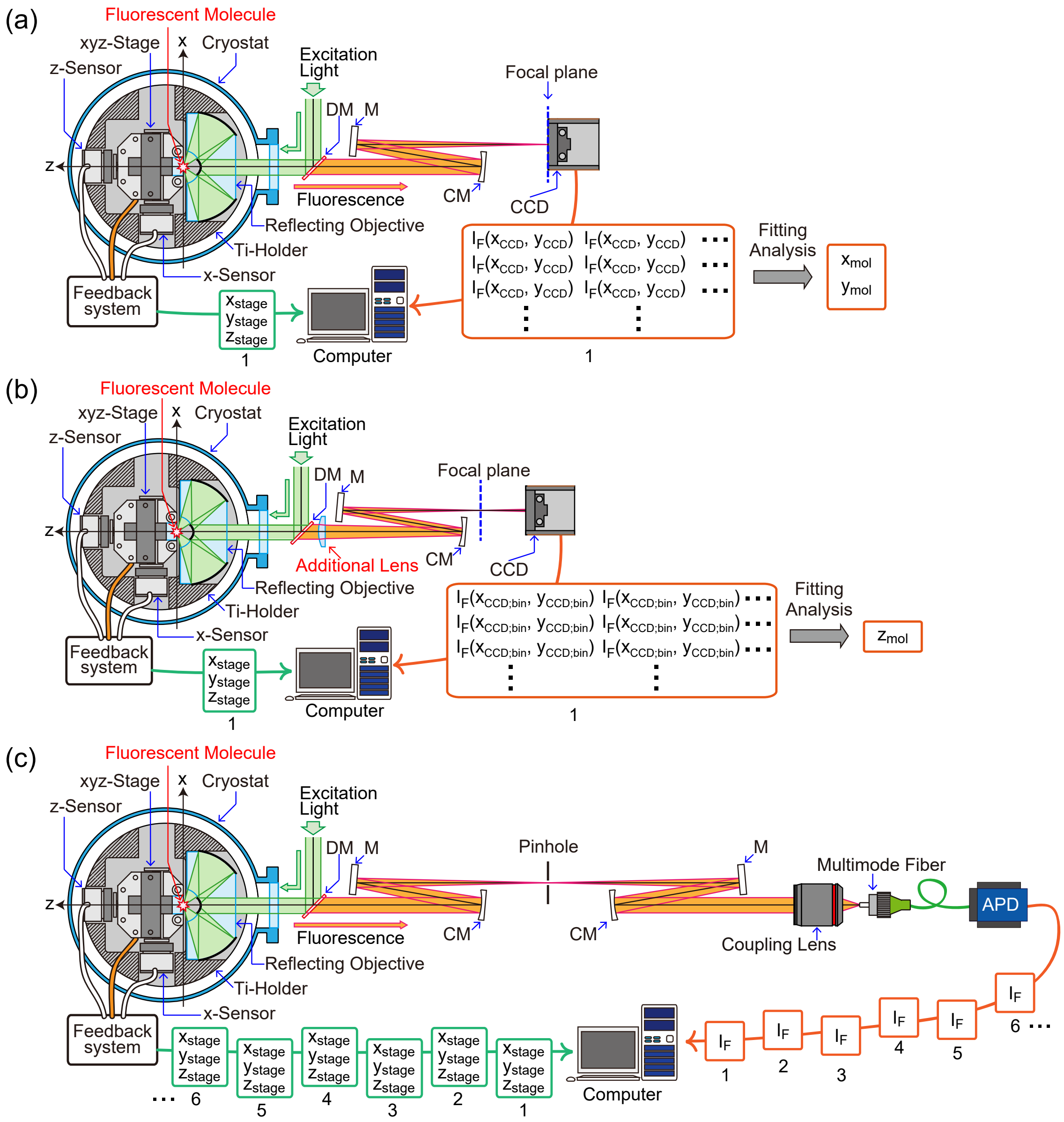

Figure 2.7 Optical setup of the cryo-reflecting microscope. We operated the cryo-reflecting microscope in three modes. (a) Configuration for *xy*-localization. (b) Configuration for *z*-localization. (c) Configuration for imaging using confocal raster-scanning imaging. Symbols are DM: Dichroic mirror, CM: a silver-coated concave mirror ($f_{\mathrm{CM}}$ = 1000 mm), M: a silver-coated flat mirror, CCD: charge coupled device, $x_{\mathrm{stage}}$, $y_{\mathrm{stage}}$, and $z_{\mathrm{stage}}$: the 3D position of the *xyz*-stage measured by capacitive sensors, $I_{\mathrm{F}}(x_{\mathrm{CCD}}, y_{\mathrm{CCD}})$: the fluorescence intensity on a CCD pixel positioned at $x_{\mathrm{CCD}}$ and $y_{\mathrm{CCD}}$, $x_{\mathrm{mol}}$ and $y_{\mathrm{mol}}$: the lateral (*xy*-) position of the fluorescent molecule localized using $I_{\mathrm{F}}(x_{\mathrm{CCD}}, y_{\mathrm{CCD}})$, $I_{\mathrm{F}}(x_{\mathrm{CCD;bin}}, y_{\mathrm{CCD;bin}})$: the fluorescence intensity on a CCD pixel positioned at binning pixel $x_{\mathrm{CCD;bin}}$ and $y_{\mathrm{CCD;bin}}$ , $z_{\mathrm{mol}}$: the axial (*z*-) position of the fluorescent molecule localized using $I_{\mathrm{F}}(x_{\mathrm{CCD;bin}}, y_{\mathrm{CCD;bin}})$, APD: Avalanche photo-diode detector, $I_{\mathrm{F}}$: the fluorescence intensity observed with a single channel detector (APD). In the measurement of c, the fluorescence intensity ($I_{\mathrm{F}}$) of an individual ATTO647N molecule was measured point-by-point with a single-channel photodetector via raster scanning of the sample position ($x_{\mathrm{stage}}, y_{\mathrm{stage}}, z_{\mathrm{stage}}$).

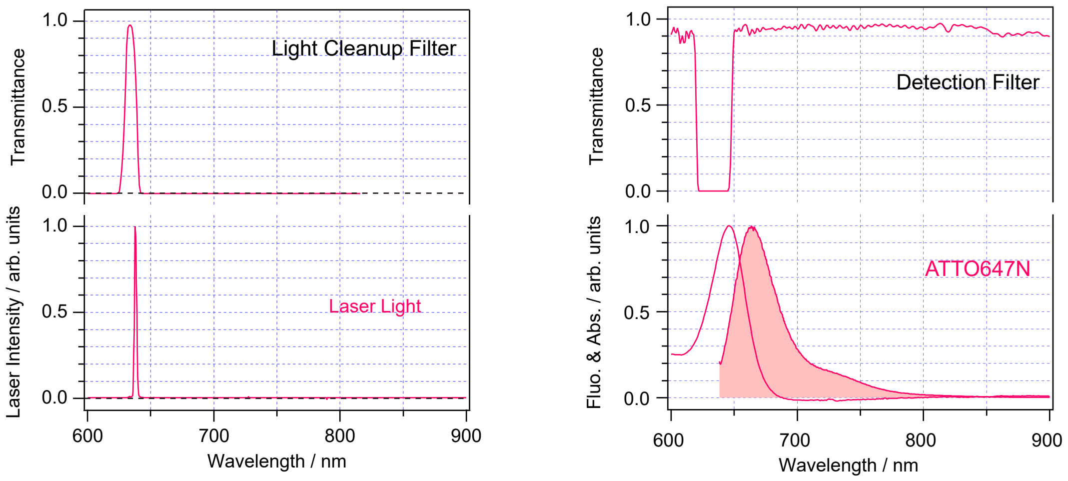

Figure 2.8 Spectra of optical filters, laser light, and ATTO647N. (left top) Transmittance of cleanup filters for red laser light. This filter are represented by Filter 1in Fig. 2.6. (left bottom) Spectrum of the red laser light (OBIS637-140mW, Coherent). (right top) Detection filter for the fluorescence of the ATTO647N. This filter are represented by Filters 2 and 3 in Fig. 2.6. (right bottom) Absorption and fluorescence spectra of ATTO647N in buffer solution at a temperature of 296 K. The excitation wavelength of the fluorescence spectrum of ATTO647N were 637 nm.

taken point-by-point with a single-channel detector through raster scanning of the sample is severely influenced by blinking, whereas an image taken with a 2D multi-channel detector is free from blinking noise. Figures 2.9b and 2.9c compare the fluorescence image of the same ATTO647N molecule taken using raster scanning with a single-channel detector (b) and 2D imaging with a multichannel detector (c) at 1.8 K. In the raster scanning image, the blinking noise is observed as several black lines along the $x$-axis (the scanning-line direction). The central disk was weakened and the concentric rings were emphasized. By contrast, the signal-to-noise ratio of the multichannel image (Fig. 2.9c) is apparently better than that of the raster scan image (Fig. 2.9b). Therefore, in the present work, not only the lateral $(x, y)$ localization but also the axial ($z$-) localization of an individual fluorescent molecule was performed using blinking-free images obtained with a 2D multichannel detector.

### 2.4.2 Blinking free image

Figure 2.7b shows the cryo-reflecting microscope for the 3D-localization of an individual fluorescent molecule. In Fig. 2.7b, the microscope is shown in the configuration for the $z$-localization. The details of the microscope are described in section 2.3.5. In brief, the blink-

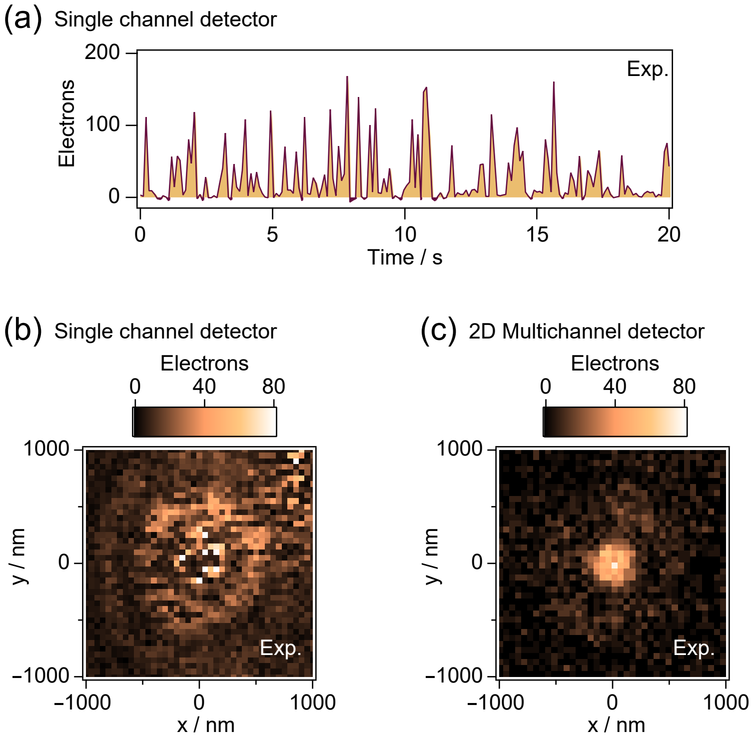

Figure 2.9 Experimental results for fluorescence blinking of an individual ATTO647N molecule at 1.8 K. (a) The temporal behavior of the fluorescence intensities of an individual ATTO647N molecule was measured with a single-channel detector. The time interval was 0.1 s. (b, c) The fluorescence image of the individual ATTO647N molecule at 1.8 K taken by raster scanning with a single-channel detector (b) and 2D imaging with a multichannel detector (c). The accumulation time was 0.05 s/pixel (b) and 10 s/frame (c). The accumulation time of image c relative to that of image b was adjusted for the two types of measurements to yield similar fluorescence intensities inside the central disk. The excitation wavelength ($\lambda_{\mathrm{ex}}$) was 637 nm, and the laser intensity on the sample was 0.8 kW/cm$^2$ in image a, b, and c.

ing noise of the fluorescence of an individual molecule was rejected via localization in all three directions using a 2D multichannel detector. We minimized back-ground emission by focusing the excitation light tightly to a nearly diffraction-limited spot on the sample. For the $xy$-localization, the fluorescence of the molecule was tightly focused with a concave mirror onto a charge-coupled device (CCD) sensor. The $xy$-position of the individual ATTO647N molecule was determined from the centroid of the full-pixel fluorescence image at the focal plane using a weighted-least-squares fitting of a 2D Airy function (Fig. 2.10b) [27].

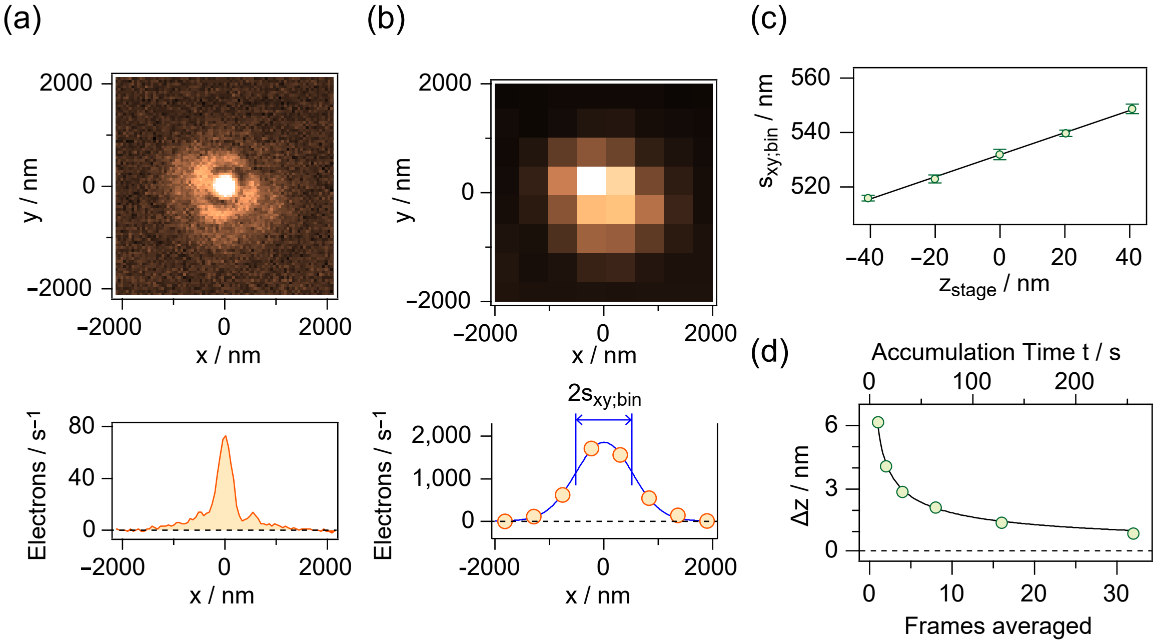

Figure 2.10 Results of axial ($z$-) localization using a 2D multichannel detector. The symbols are DM: Dichroic mirror, M: Plane mirror, CM: Concave mirror, CCD: Charge-coupled device. (a) Full-pixel image of defocused fluorescence of an individual ATTO647N molecule at 1.8 K. (b) 10 × 10 on-chip-binning image of the defocused fluorescence. (c) Standard deviation of image b ($s_{xy;\mathrm{bin}}$) as a function of the stage position ($s_{z;\mathrm{stage}}$), shown as a circle with an error bar. (d) The $z$-localization error of the individual ATTO647N molecule (circle) at 1.8 K as a function of the number of frames averaged (bottom axis) and corresponding accumulation time $t$ (top axis). The excitation wavelength ($\lambda_{\mathrm{ex}}$) was 637 nm.

### 2.4.3 3D-localization using CCD camera

The axial ($z$-) position of a fluorescent molecule was determined from the 2D image. Figure 2.10a shows the full-pixel image (80 × 80 pixels) of the defocused fluorescence of an individual ATTO647N molecule at 1.8 K and its 1D section at $y = 0$ nm. As characteristic of optics with obstruction, concentric outer rings stand out. The high-spatial-frequency components depend on the fluorescence spectrum of individual molecules and it is difficult to make the model function. We binned the 10 × 10 pixels of the defocused fluorescence image to suppress the high-spatial-frequency components. Figure 2.10b shows the 10 × 10 on-chip-binning image (8 × 8 pixels) of the defocused fluorescence of the individual ATTO647N molecule at 1.8 K and its 1D section at $y = 0$ nm. As observed in the 1D section, the 10 × 10-binning image approximates a Gaussian function (blue). The standard deviation of the binning image on the $xy$-plane ($s_{xy;\mathrm{bin}}$) was evaluated by the weighted-least-squares fitting of a 2D Gaussian function. In Fig. 2.10c, $s_{xy;\mathrm{bin}}$ was found to be linearly proportional to the position of the sample stage ($s_{z;\mathrm{stage}}$) in the range form -40 nm to 40 nm. The $z$-localization error ($\Delta z$) of the individual ATTO647N molecule at 1.8 K was measured as a function of the number of frames averaged (Fig. 2.10d). The accumulation time for one frame was 8 s. The axial localization error $\Delta z$ reached 0.90 nm when the 32 frames were averaged (corresponding accumulation time $t$ = 256 s and the numbers of detected photons $N = 3.0 \times 10^6$). To test whether our cryo-reflecting microscope can resolve nanometer-scale displacement, the individual ATTO647N molecule at 1.8 K was repeatedly localized under the same condition at the three stage positions $(x_{\mathrm{stage}}, y_{\mathrm{stage}}, z_{\mathrm{stage}}) = (-3$ nm, $-3$ nm, $-3$ nm), (0 nm, 0 nm, 0 nm) and (3 nm, 3 nm, 3 nm). The accumulation time t was 64 s $(x, y)$ and 256 s ($z$) per one localization point. Figure 2.11(a) shows the experimental result for the 3D localization microscopy for the individual ATTO647N molecule at 1.8 K. The sizes of the $xy$- and $zy$-images are $12 \times 12$ nm$^2$. The stage position was monitored with capacitive sensors and is indicated by colored crosses. The 3D position of the individual ATTO647N molecule was localized repeatedly using its fluorescence and is shown as a circle of the same color. The pink, yellow and green circles were measured at $(x_{\mathrm{stage}}, y_{\mathrm{stage}}, z_{\mathrm{stage}}) = (-3$ nm, $-3$ nm, $-3$ nm), (0 nm, 0 nm, 0 nm), and (3 nm, 3 nm, 3 nm), respectively. As shown, the cryo-reflecting microscope can resolve a 3-nm displacement of the individual ATTO647N molecule. Figure 2.11(b) shows histograms of the variances between the localized positions $(x_{\mathrm{mol}}, y_{\mathrm{mol}}, z_{\mathrm{mol}})$ and the stage positions. The standard deviations of the variances are 0.53 nm ($x$), 0.31 nm ($y$) and 0.90 nm ($z$), which correspond to $\Delta x$, $\Delta y$, and $\Delta z$ of our cryo-reflecting microscope.

The number of electrons is shown as $N$ in Table S12.1. The standard deviations of s were evaluated from the observed images (see Figs.2.9c and 2.10b). From the experimental values of $\Delta r$, $N$, and $s$, the experimental coefficients in Eq. 2.5 and 2.8 were calculated as 3.8 ($A_x^{\mathrm{Exp.}}$), 2.2 ($A_y^{\mathrm{Exp.}}$), and 3.0 ($A_z^{\mathrm{Exp.}}$). The experimental coefficients are approximately twofold of the simulated coefficient, which suggests that the $xyz$-localization errors are twofold greater than that in the case of $\delta_{\mathrm{drift}}$ and $\delta_{\mathrm{back}} = 0$. We preliminarily tested that the temperature of the driver box for the $x$-position sensors was stabilized; $\Delta x$ then became similar to $\Delta y$. The $y$-localization might have been due to the thermal drift of the feedback loop circuit. Finally, we consider the $z$-localization experiment. In Eq. 2.7, $\delta_{z;\mathrm{drift}}{}^2 + \delta_{z;\mathrm{back}}{}^2$ is approximately 1 nm$^2$. From the mechanical design, the mechanical stabilities of the stage in the $x$ and $z$-

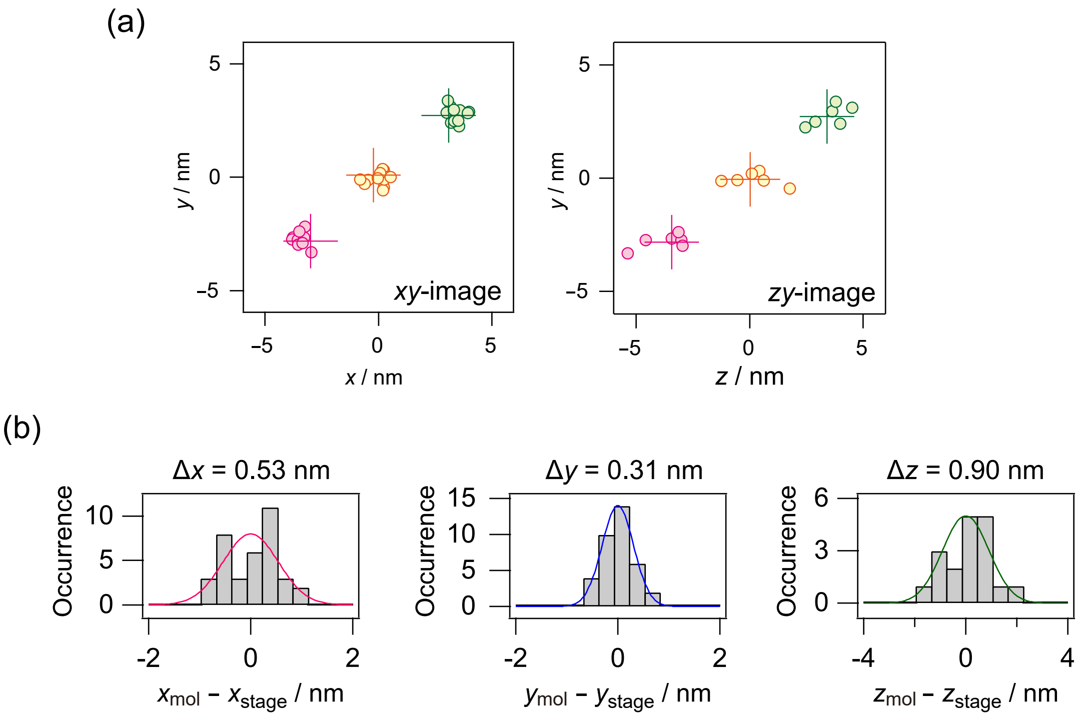

Figure 2.11 3D localization of an individual ATTO647N molecule with $\lambda_{\mathrm{ex}}$ of 637 nm at 1.8 K. (a) The $xy$- and $zy$-images of the localized position of the ATTO647N molecule at three stage positions $(x_{\mathrm{stage}}, y_{\mathrm{stage}}, z_{\mathrm{stage}})$ = (−3 nm, −3 nm, −3 nm), (0 nm, 0 nm, 0 nm) and (3 nm, 3 nm, 3 nm), shown as pink, yellow and green circles, respectively. The measurements were repeated 12 times $(x, y)$ and 6 times $(z)$ at each stage position. The image size is 12 × 12 $\mathrm{nm}^2$ and the accumulation time t was 64 s $(x, y)$ and 256 s $(z)$. During the repeated localization measurements, the cryo-stage positions were monitored and stabilized by the capacitive sensors and are shown with colored crosses. (b) Histograms of the variance between the stage position and the localized positions of the individual ATTO647N molecule.

directions are similar to each other. The ${\delta_{z;\mathrm{drift}}}^2$ is less than $\Delta x^2 = (0.53\mathrm{nm})^2$. The readout noise of the CCD camera (4.5 $e^-$ in the standard deviation) is negligible because the noise was much smaller than the number of electrons in the signal (2000 $e^-$ at the peak), as shown in Fig. 2.10b. Thus, the $z$-localization error might be deteriorated by the background of emission ($\delta_{z;\mathrm{drift}}$).

In addition, the optical performance of the cryo-reflecting microscope was characterized by other fluorophores, i.e., Alexa Fluor 750 and Qdot 705, as shown in Figures 2.12 and 2.13.

Table 2.1 Three-dimensional localization error of cryo-localization microscopy for an individual ATTO647N molecule at 1.8 K.

| Axis | Localization Error | $t$ / s | $N$ | $s$ / nm | $A^{\mathrm{exp.}}$ | $A^{\mathrm{sim.}}$ | $A^{\mathrm{exp.}}$ / $A^{\mathrm{sim.}}$ |
|---|---|---|---|---|---|---|---|
| $x$ | 0.53 nm | 64 | $0.99 \times 10^6$ | 139 | 3.8 | 1.7 | 2.2 |
| $y$ | 0.31 nm | 64 | $0.99 \times 10^6$ | 139 | 2.2 | 1.7 | 1.3 |
| $z$ | 0.90 nm | 256 | $3.0 \times 10^6$ | 515 | 3.0 | 1.3 | 2.4 |

(a) Alexa750-DNA

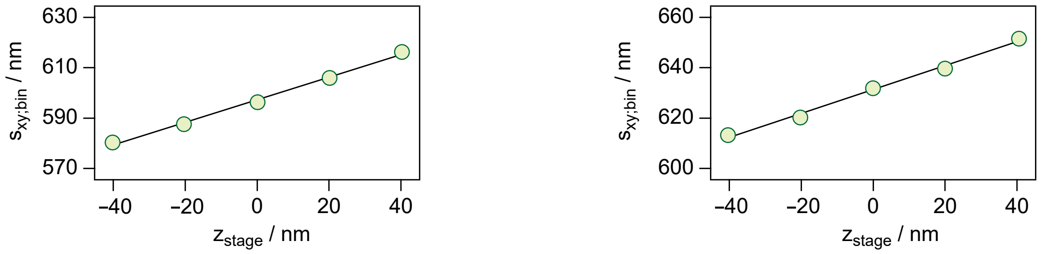

(b) Alexa750-DNA

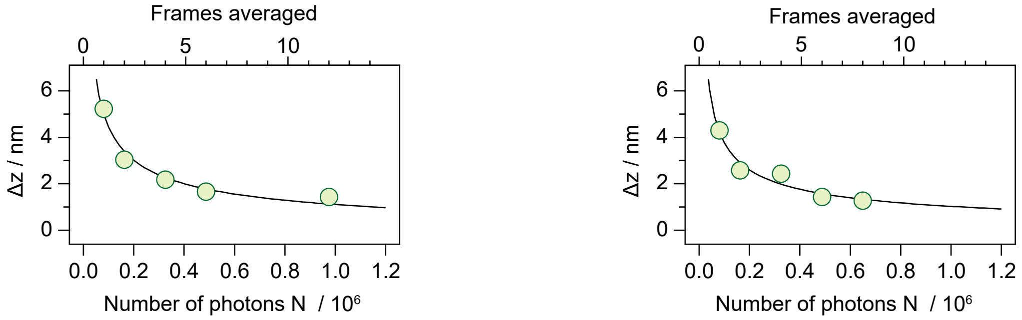

Figure 2.12 (a) Standard deviation of the binned image ($s_{xy;\mathrm{bin}}$) of two Alexa750-DNA molecules at 1.8 K as a function of the stage position ($z_{\mathrm{stage}}$). (b) The $z$-localization error ($\Delta z$) of two Alexa 750-DNA molecules at 1.8 K as a function of the number of photons collected ($N$). We used another reflecting objective (NA = 0.93, $f$ = 2.52 mm); hence the standard deviation sxy;bin is slightly different from Fig. 2.10c. The excitation wavelength ($\lambda_{\mathrm{ex}}$) was 730 nm.

## 2.5 Conclusion

The present experimental work demonstrated that 3D cryo-localization microscopy allows us to localize a small fluorescent molecule with molecular precision. The cryo-reflecting microscope is perfectly achromatic, which is useful for multicolor imaging of different molecules in cells. In the wavefront error, a molecular orientation with respect to the fo-

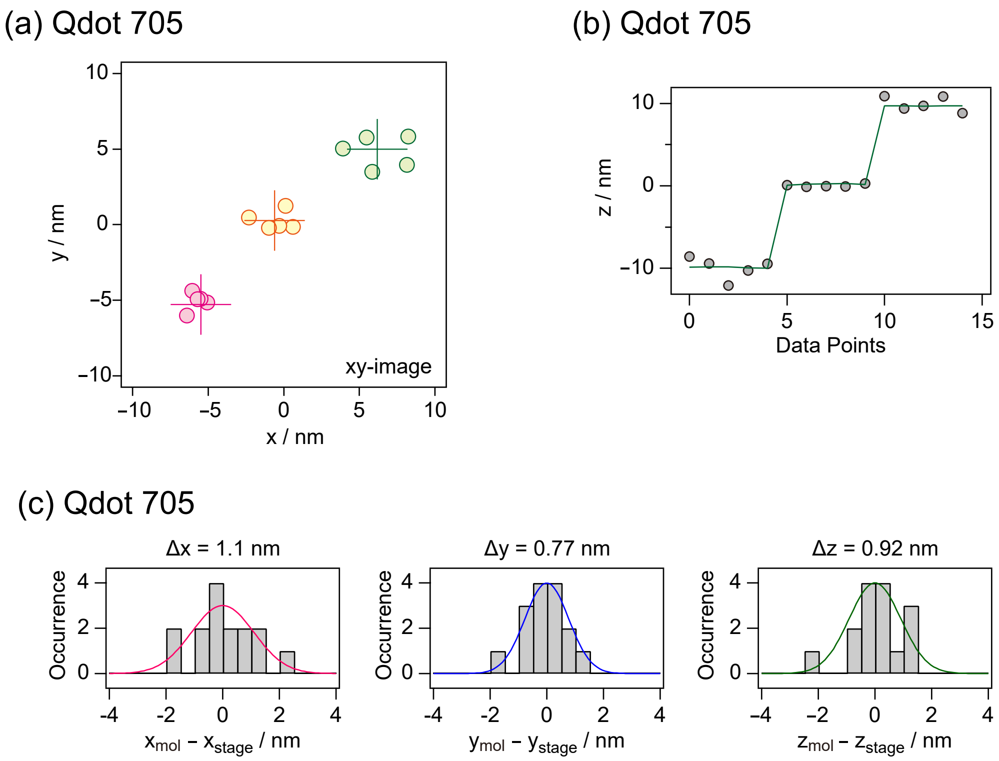

Figure 2.13 3D localization of quantum dot (Qdot 705 carboxylic acid, Invtrogen) with $\lambda_{ex}$ of 637 nm at 1.8 K. (a) The $xy$-image of localized position of the individual quantum dot at three stage positions of $(x_{stage}, y_{stage}, z_{stage})$ = (−5 nm, −5 nm, 0 nm), (0 nm, 0 nm, 0 nm), and (5 nm, 5 nm, 0 nm). The stage position is indicated by colored crosses. The localized positions of the individual quantum dot are shown in the pink, yellow, and green circles measured at $(x_{stage}, y_{stage}, z_{stage})$ = (−5 nm, −5 nm, 0 nm), (0 nm, 0 nm, 0 nm), and (5 nm, 5 nm, 0 nm), respectively. (b) The $z$-localized position of another quantum dot at three stage positions $(x_{stage}, y_{stage}, z_{stage})$ = (0 nm, 0 nm, −5 nm), (0 nm, 0 nm, 0 nm), and (0 nm, 0 nm, 5 nm). The localized positions are indicated by gray circles and the $z$-stage position is shown by green line. The accumulation time $t$ per point was 6 s (a) and 256 s (b), and the number of detected photons per point was $1.1 \times 10^5$ in (a) and $1.6 \times 10^6$ (b). (c) Histograms of the variances between the stage position and localized positions of the individual quantum dots, which are calculated from (a) and (b). The localization errors were evaluated from the variances to 1.1 nm ($\Delta x$), 0.77 nm ($\Delta x$), and 0.92 nm ($\Delta x$).

cal plane will cause a spatial shift on the $xy$-image at the off-focus position if a large size of a molecular complex is observed [30]. The spatial shift can be perfectly corrected by information about $xyz$-position of individual molecules and the $xy$-section images around $z = 0$ μm, which can be obtained with our cryo-microscope. Thus, biomolecules in such a specimen will be precisely localized by our cryo-reflecting microscope.

The experimental barrier expected for 3D cryo-localization microscopy of multiple molecules in cells is how to distinguish multiple fluorescent molecules that reside within their fluorescence spots. In general, at a few K, the spectral width of the electronic absorption of individual fluorescent molecules is much narrower than that of the ensemble absorption of the fluorescent molecule [13, 17]. The absorption peaks of individual fluorescent molecules are spectrally isolated from each other by their local environments; consequently the spectral overlap of different fluorescent molecules becomes negligible at an appropriate concentration. Three hundred individual fluorescent molecules in an n-hexadecane matrix that resided inside the focal volume of light were spectrally selected and localized with the standard error of approximately 20 nm in the $xy$-directions [13]. Although the spectral width of individual dye molecules becomes broad in a polar matrix such as cell, the width of individual molecules is narrower than that of their ensemble [18, 31–33]. Therefore, there will be a system and condition that enables excitation and imaging of individual fluorescent molecules in cells.

# Reference List

[1] S. Nickell, C. Kofler, A. P. Leis and W. Baumeister: “A visual approach to proteomics”, Nature Reviews Molecular Cell Biology, **7**, 3, pp. 225–230 (2006).

[2] E. Betzig, G. H. Patterson, R. Sougrat, O. W. Lindwasser, S. Olenych, J. S. Bonifacino, M. W. Davidson, J. Lippincott-Schwartz and H. F. Hess: “Imaging intracellular fluorescent proteins at nanometer resolution”, Science, **313**, 5793, pp. 1642–1645 (2006).

[3] M. Fernández-Suárez and A. Y. Ting: “Fluorescent probes for super-resolution imaging in living cells”, Nature Reviews Molecular Cell Biology, **9**, 12, pp. 929–943 (2008).

[4] B. Huang, S. A. Jones, B. Brandenburg and X. Zhuang: “Whole-cell 3D STORM reveals interactions between cellular structures with nanometer-scale resolution”, Nature Methods, **5**, 12, pp. 1047–1052 (2008).

[5] S. Jia, J. C. Vaughan and X. Zhuang: “Isotropic three-dimensional super-resolution imaging with a self-bending point spread function”, Nature Photonics, **8**, 4, pp. 302–306 (2014).

[6] H. Shroff, C. G. Galbraith, J. A. Galbraith and E. Betzig: “Live-cell photoactivated localization microscopy of nanoscale adhesion dynamics”, Nature Methods, **5**, 5, pp. 417–423 (2008).

[7] A. Yildiz, J. N. Forkey, S. A. McKinney, T. Ha, Y. E. Goldman and P. R. Selvin: “Myosin V walks hand-over-hand: single fluorophore imaging with 1.5-nm localization”, Science, **300**, 5628, pp. 2061–2065 (2003).

[8] A. Pertsinidis, Y. Zhang and S. Chu: “Subnanometre single-molecule localization, registration and distance measurements”, Nature, **466**, 7306, pp. 647–651 (2010).

[9] F. Balzarotti, Y. Eilers, K. C. Gwosch, A. H. Gynnå, V. Westphal, F. D. Stefani, J. Elf and S. W. Hell: “Nanometer resolution imaging and tracking of fluorescent molecules with minimal photon fluxes”, Science, **355**, 6325, pp. 606–612 (2017).

[10] R. Zondervan, F. Kulzer, M. A. Kol’chenk and M. Orrit: “Photobleaching of rhodamine 6G in poly (vinyl alcohol) at the ensemble and single-molecule levels”, The Journal of Physical Chemistry A, **108**, 10, pp. 1657–1665 (2004).

[11] S. Fujiyoshi, M. Hirano, M. Matsushita, M. Iseki, et al.: “Structural change of a cofactor binding site of flavoprotein detected by single-protein fluorescence spectroscopy at

1.5 K", Physical Review Letters, **106**, 7, p. 078101 (2011).

[12] S. Weisenburger, B. Jing, A. Renn and V. Sandoghdar: "Cryogenic localization of single molecules with angstrom precision", Nanoimaging and Nanospectroscopy, Vol. 8815International Society for Optics and Photonics, p. 88150D (2013).

[13] A. Bloeß, Y. Durand, M. Matsushita, H. Van Dermeer, G. Brakenhoff and J. Schmidt: "Optical far-field microscopy of single molecules with 3.4 nm lateral resolution", Journal of Microscopy, **205**, 1, pp. 76–85 (2002).

[14] S. Weisenburger, B. Jing, D. Hänni, L. Reymond, B. Schuler, A. Renn and V. Sandoghdar: "Cryogenic colocalization microscopy for nanometer-distance measurements", ChemPhysChem, **15**, 4, pp. 763–770 (2014).

[15] W. Li, S. C. Stein, I. Gregor and J. Enderlein: "Ultra-stable and versatile widefield cryo-fluorescence microscope for single-molecule localization with sub-nanometer accuracy", Optics Express, **23**, 3, pp. 3770–3783 (2015).

[16] S. Weisenburger, D. Boening, B. Schomburg, K. Giller, S. Becker, C. Griesinger and V. Sandoghdar: "Cryogenic optical localization provides 3D protein structure data with angstrom resolution", Nature Methods, **14**, 2, pp. 141–144 (2017).

[17] A. Van Oijen, J. Köhler, J. Schmidt, M. Müller and G. Brakenhoff: "3-Dimensional super-resolution by spectrally selective imaging", Chemical Physics Letters, **292**, 1-2, pp. 183–187 (1998).

[18] S. Fujiyoshi, M. Fujiwara and M. Matsushita: "Visible fluorescence spectroscopy of single proteins at liquid-helium temperature", Physical Review Letters, **100**, 16, p. 168101 (2008).

[19] S. Fujiyoshi, Y. Furuya, M. Iseki, M. Watanabe and M. Matsushita: "Vibrational microspectroscopy of single proteins", The Journal of Physical Chemistry Letters, **1**, 17, pp. 2541–2545 (2010).

[20] D. Uchiyama, H. Oikawa, K. Otomo, M. Nango, T. Dewa, S. Fujiyoshi and M. Matsushita: "Reconstitution of bacterial photosynthetic unit in a lipid bilayer studied by single-molecule spectroscopy at 5 K", Physical Chemistry Chemical Physics, **13**, 24, pp. 11615–11619 (2011).

[21] M. Maruo, H. Inagawa, Y. Toratani, T. Kondo, M. Matsushita and S. Fujiyoshi: "Three-dimensional laser-scanning confocal reflecting microscope for multicolor single-

molecule imaging at 1.5 K”, Chemical Physics Letters, **591**, pp. 233–236 (2014).

[22] I. Nakamura, T. Yoshihiro, H. Inagawa, S. Fujiyoshi and M. Matsushita: “Spectroscopy of single $Pr^3$+ ion in $LaF_3$ crystal at 1.5 K”, Scientific Reports, **4**, p. 7364 (2014).

[23] H. Inagawa, Y. Toratani, K. Motohashi, I. Nakamura, M. Matsushita and S. Fujiyoshi: “Reflecting microscope system with a 0.99 numerical aperture designed for three-dimensional fluorescence imaging of individual molecules at cryogenic temperatures”, Scientific Reports, **5**, p. 12833 (2015).

[24] Y.-W. Chang, S. Chen, E. I. Tocheva, A. Treuner-Lange, S. Löbach, L. Søgaard-Andersen and G. J. Jensen: “Correlated cryogenic photoactivated localization microscopy and cryo-electron tomography”, Nature Methods, **11**, 7, pp. 737–739 (2014).

[25] Y. Fujiyoshi, T. Mizusaki, K. Morikawa, H. Yamagishi, Y. Aoki, H. Kihara and Y. Harada: “Development of a superfluid helium stage for high-resolution electron microscopy”, Ultramicroscopy, **38**, 3-4, pp. 241–251 (1991).

[26] T. Hinohara, Y. I. Hamada, I. Nakamura, M. Matsushita and S. Fujiyoshi: “Mechanical stability of a microscope setup working at a few kelvins for single-molecule localization”, Chemical Physics, **419**, pp. 246–249 (2013).

[27] R. E. Thompson, D. R. Larson and W. W. Webb: “Precise nanometer localization analysis for individual fluorescent probes”, Biophysical journal, **82**, 5, pp. 2775–2783 (2002).

[28] H. P. Kao and A. Verkman: “Tracking of single fluorescent particles in three dimensions: use of cylindrical optics to encode particle position”, Biophysical Journal, **67**, 3, pp. 1291–1300 (1994).

[29] L. Holtzer, T. Meckel and T. Schmidt: “Nanometric three-dimensional tracking of individual quantum dots in cells”, Applied Physics Letters, **90**, 5, p. 053902 (2007).

[30] J. Engelhardt, J. Keller, P. Hoyer, M. Reuss, T. Staudt and S. W. Hell: “Molecular orientation affects localization accuracy in superresolution far-field fluorescence microscopy”, Nano Letters, **11**, 1, pp. 209–213 (2010).

[31] A. M. van Oijen, M. Ketelaars, J. Köhler, T. J. Aartsma and J. Schmidt: “Unraveling the electronic structure of individual photosynthetic pigment-protein complexes”, Science, **285**, 5426, pp. 400–402 (1999).

[32] R. J. Cogdell, A. Gall and J. Köhler: “The architecture and function of the light-

harvesting apparatus of purple bacteria: from single molecules to in vivo membranes”, Quarterly Reviews of Biophysics, **39**, 3, pp. 227–324 (2006).

[33] J. Baier, M. Gabrielsen, S. Oellerich, H. Michel, M. Van Heel, R. Cogdell and J. Köhler: “Spectral diffusion and electron-phonon coupling of the B800 BChl a molecules in LH2 complexes from three different species of purple bacteria”, Biophysical Journal, **97**, 9, pp. 2604–2612 (2009).

# Chapter 3

# Nanometer accuracy of individual fluorophores

The contents of this chapter were prepared from the journal of our group.

Taku Furubayashi, Keita Ishida, Hiromu Kashida, Eiji Nakata, Takashi Morii, Michio Matsushita, and Satoru Fujiyoshi,

“ Nanometer Accuracy in Cryogenic Far-Field Localization Microscopy of Individual Molecules ” *The Journal of Physical Chemistry Letters* **10**, 5841 – 5846 (2019)

## 3.1 Introduction

Biological activity in cells is regulated by a variety of molecules that interact with each other. To understand life, it is essential to obtain nanoscale three-dimensional (3D) information regarding the intracellular arrangements and mutual orientations of individual biomolecules. The most promising methods in realizing the nanometer-accuracy 3D imaging of cellular interiors include cryogenic (cryo) electron tomography of a thin section of the cell and cryo-fluorescence localization microscopy with a far-field configuration. The samples are prepared by vitrification, i.e., rapid freezing of a living cell below glass transition temperature. In the vitrified samples, the native state of the living cell is almost preserved; thus, the near-native state can be imaged with any desired spatial precision using any long accumulation time [1, 2]. The cryo-electron tomography of a mechanically sliced section has a high resolution for cellular imaging (4 – 5 nm). However, the resolution is still insufficient for identifying molecular species from the image alone. In addition, because of the penetration depth of electrons, the maximum thickness of a sample is approximately 0.1 μm, which is much thinner than the typical thickness of a cell (approximately 10 μm). Fluorescence far-field microscopy, in contrast, does not face these difficulties. A fluorophore can be employed as a label to a target biomolecule in cell with a high molecular specificity; thus, the identified biomolecules can be selectively imaged [3]. Because of the high transmission of excitation and fluorescence wavelengths, a lateral ($xy$-) optical section of a whole cell at a desired axial ($z$-) position can be observed without mechanical slicing [4]. In addition, under cryogenic conditions, the electronic spectrum of a single fluorophore is narrower than that of the ensemble; thus, each fluorophore can be selectively localized from an ensemble of the same fluorophores [5–7]. In 2002, the $xy$-localization precision of each fluorophore ($\Delta_{xy}$), in units of standard error, reached 3 nm at 1.2 K [8]. However, the $z$-localization precision $\Delta_z$ had remained at approximately 100 nm for some times beginning in 1998 [9]. In 2017, instead of achieving the 3D localization of a single molecule, the 3D average position (probability density) of fluorophores at 4 K was reconstructed from $xy$-images of thousands of fluorophores [10]. This approach using ensemble averaging requires the assumption of a single conformation common to all molecules. In the same year, we demonstrated the 3D localization microscopy of a single fluorophore with nanometer precision using a homemade reflecting cryo-microscope [11]. In many cases, the localization precision of each fluorophore is different from the accuracy of the relative positions of multiple fluorophores.

I developed cryogenic fluorescence microscope which has angstrom precision in the previous chapter. In this chapter, I demonstrated nanometer accuracy in the far-field fluorescence localization microscopy of two fluorophores bonded to both ends of 30 base pairs (30 bp) of double-stranded DNA (dsDNA) molecule at 1.8 K. The dual-labeled dsDNA molecule served as a molecular ruler with nanometer accuracy [12, 13]. In conventional fluorescence localization using far-field microscopy, an $xy$-centroid for each fluorophore is determined from an image at a $z$-position within a diffraction-limited focal depth ($\Delta_z$ = 700 nm for the present microscope). Although $\Delta_{xy}$ was 1 nm, the $xy$-projection of the distance between the two fluorophores ($D_{xy}$) was distributed from 0 to 50 nm. Mislocalization was mainly caused by a $z$-dependent $xy$-shift due to the dipole-orientation effect [14–22]. This $xy$-shift was reduced using a 3D localization with $\Delta_z$ = 11 nm and$\Delta_{xy}$ = 1 nm. By correcting the mislocalization, the distribution of $D_{xy}$ was centered around a dsDNA length of 10 nm and the standard deviation of $D_{xy}$ was 5 nm. This result shows that nanometer-accuracy localization of multiple fluorophores with far-field microscopy requires not only the $xy$-precision but also the $z$-precision, far beyond the diffraction limit.

## 3.2 Experiment steup

### 3.2.1 Cryo-reflecting microscope

Figure 3.1a shows an optical setup for reflecting cryogenic (cryo-) microscope. The cryo-microscope was operated in CCD-localization and sample-scanning modes. The microscope consisted of the reflecting optics to minimize the chromatic aberration. The optics on the outside of a cryostat were placed in airtight stainless-steel boxes for the mechanical stabilization. The photographs of the airtight boxes were reported previously [11]. Figure 3.1b shows the optical arrangement and the coordinates for 3D centroid determination with the cryo-microscopy. The distance between the cryo-objective mirror and the imaging mirror was set to 1002 mm (= $f_{\mathrm{obj}} + f_{\mathrm{img}}$). The image plane of the CCD camera was set to the focus of the imaging mirror. We define an orientation angle of fluorophores as $\theta_{zx}$ on the $zx$-plane (and $\theta_{zy}$ on the $zy$-plane) and a tilt angle of the PSF as $\phi_{zx}$ on the $zx$-plane (and $\phi_{zy}$ on the

$zy$-plane).

In the setup (Fig. 3.1a), a light source for photoexcitation of fluorophores was a continuous-wave diode laser with the excitation wavelengths $\lambda_{\mathrm{ex}}$ of 637 nm (OBIS637-140mW, Coherent) and 730 nm (OBIS730-30mW, Coherent). The spectra of the laser lights are shown in the bottom panel of Fig. 3.2a. The laser lights were coupled with polarization-maintained single-mode fibers (mode field diameter of 4.5 μm at 630 nm and Numerical aperture of 0.12; PM630-HP, Thorlabs) and the outputs were collimated by the achromatic lenses with a focal length of 30 mm (for $\lambda_{\mathrm{ex}}$ of 730 nm, AC254-030A, Thorlabs; for $\lambda_{\mathrm{ex}}$ of 637 nm, AC254-030B, Thorlabs). The collimated laser lights were spectrally cleaned with bandpass filters (for $\lambda_{\mathrm{ex}}$ of 637 nm, FF01-637/7, Semrock; for $\lambda_{\mathrm{ex}}$ of 730 nm, #65176, Edmund optics). The spectra of the laser cleanup filters are shown in a top panel of Fig. 3.2a. The component of the elliptical polarization of the excitation light was blocked by the film polarizers (for $\lambda_{\mathrm{ex}}$ of 637 nm, 10LP-VIS-B, Newport; $\lambda_{\mathrm{ex}}$ of 730 nm, LPVIS050-MP2, Thorlabs). The polarization of the light on the sample was controlled with the combination of a half-wave ($\lambda/2$) plate and a quarter-wave ($\lambda/4$) plate (for $\lambda_{\mathrm{ex}}$ of 637 nm, WPHH05M-633 and WPQ05M-633, Thorlabs; $\lambda_{\mathrm{ex}}$ of 730 nm, AHWP05M-600 and AQWP05M-600, Thorlabs). The wave front error of the lights was reduced by a reflecting spatial filter that composed of a silver-coated concave mirror (the focal length of 250 mm, 10DC500ER.2, Newport) and a 20-μm pinhole (PA-20, Sigma Koki).

The light reflected by a parallel window of $\mathrm{CaF_2}$ (the thickness of 5 mm, the surface flatness of $\lambda$ / 10 at 632.8 nm, and the parallelism of < 5 arc-seconds; OPCFSP-25.4C05-10-5, Sigma Koki) was conducted into a superfluid-helium cryostat. The light was focused on the sample by a cryo-objective mirror called the ‘ INAGAWA mirror ’ (the focal length of 2.04 nm in detection, the numerical aperture of 0.99 in superfluid helium). The fluorescence of the fluorophores was collected and collimated by the INAGAWA mirror. To obtain a 3D fluorescence image, the sample position was finely moved with a piezo-driven cryo-scanner in the $xyz$-directions with a scanning range of $30 \times 15 \times 30$ μm$^3$ in the $x \times y \times z$ directions (ANSxyz100std-LT, Attocube system) and coarsely moved with two piezo-driven positioners in the $xz$-directions with the travel distance of 5 mm (ANPx101, Attocube system). The $xyz$-positions of the sample stage ($x_{\mathrm{stage}}$, $y_{\mathrm{stage}}$, $z_{\mathrm{stage}}$) were monitored with three capacitive sensors that were custom-made for cryogenic experiments (the detection range of 100 – 150

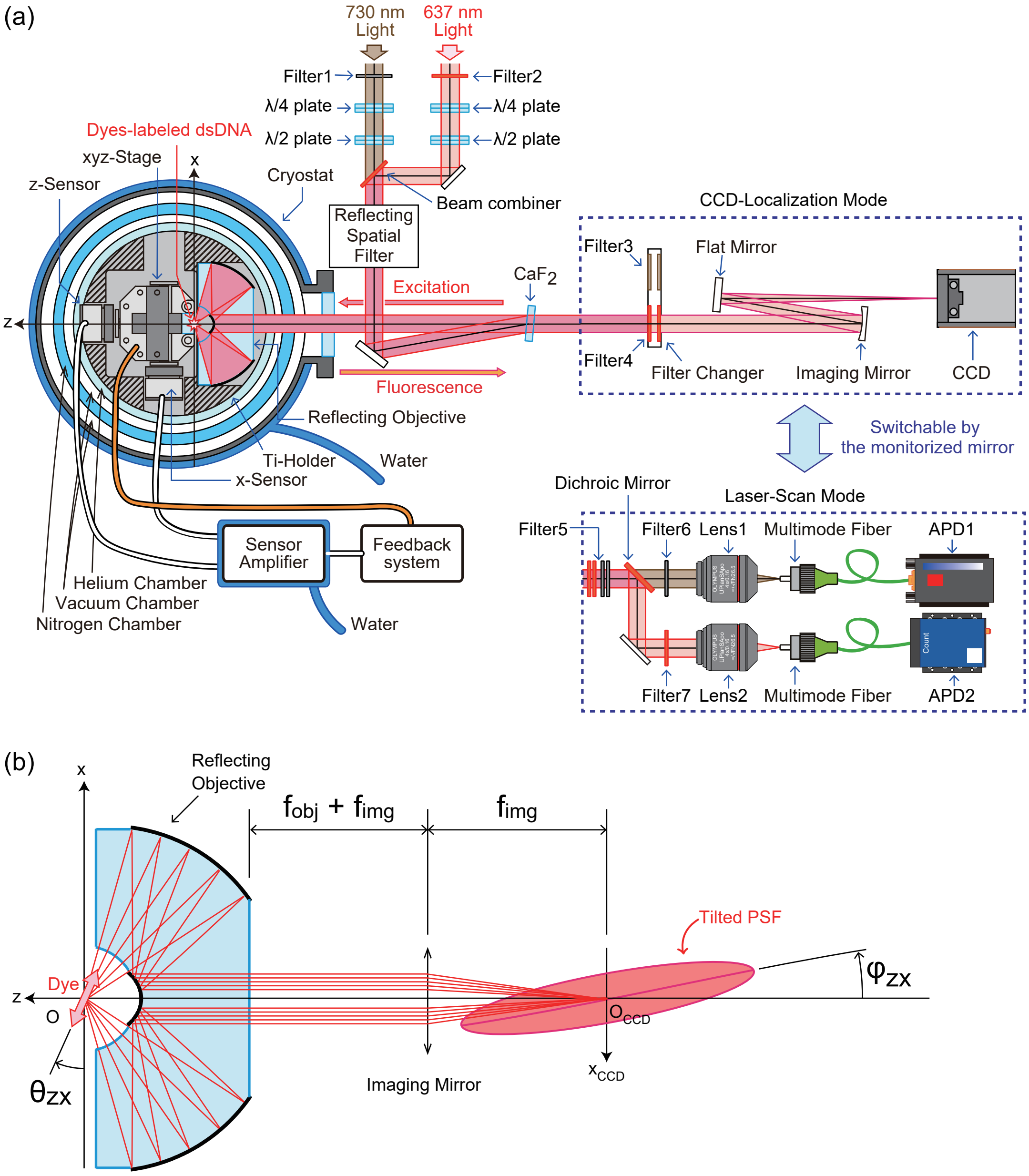

Figure 3.1 Cryo-fluorescence reflecting microscope. (a) The microscope setup. The microscope was operated in CCD-localization and in raster-type sample-scanning modes. The two modes were switchable by using a motorized flat mirror. (b) Optical arrangement for the CCD localization mode. The focal lengths of the objective mirror and the imaging mirror are represented by $f_{\mathrm{obj}}$ and $f_{\mathrm{img}}$, respectively. The orientation angle of the transition dipole of a fluorophore on the $zx$- (or $zy$-) plane is represented by $\theta_{zx}$ (or $\theta_{zy}$). The coordinate of the fluorophore around the focus of the objective is denoted by $x$, $y$, and $z$. The tilt angle of the PSF on the $xz$- (or $yz$-) plane is represented by $\phi_{zx}$ (or $\phi_{zy}$). The coordinate on the CCD camera is denoted by $x_{\mathrm{CCD;pixel}}$ and $y_{\mathrm{CCD;pixel}}$.

μm; Unipulse). The INAGAWA mirror and the three sensors were fixed with a monolithic titanium holder [11]. Components near the sample (the sample holder, the cryo-stages, and the position sensors) were mainly composed of titanium and alumina. The expansion coefficient of titanium is close to that of alumina. Thus, the mechanical drift due to asymmetric thermal expansion was reduced passively. In addition to the passive stabilization, the temperature of the superfluid helium was actively stabilized within a 0.2-mK standard deviation by using a resistance thermometer (Cernox, Lake Shore), a wire-wound resistance heater (W23, Welwyn Components), and a temperature controller (model 335, Lake Shore). Furthermore, we have stabilized the temperature of the outer wall of the cryostat as well as the amplifiers of the cryo-sensors by a circulating-cooling-water system shown in Fig. 3.3 (T257P, ThermoTek). Consequently, the image stability had a 0.05-nm standard deviation in 10 min [11].

Fluorescence of fluorophores was imaged (i) with a CCD localization mode or (ii) with a raster-type sample scanning mode. The two operation modes were switchable using a flat mirror mounted on a motorized linear stage (KXL06075-N1-C5, Suruga Seiki). In the CCD localization mode, the reflection and the scattering of the excitation light was blocked with Filters 3 and 4 (see the top panel of Fig. 3.2a). The filters could be exchanged at a frequency of approximately 10 Hz by a motorized linear stage (KXL06030-N1-C5, Suruga Seiki). A top panel of Fig. 3.2b shows the trans-mittance of Filters 3 (two 633-nm notch filters, NF-01-633U, Semrock; two 730-nm notch filters, ZET730NF, Chroma Technology; one long-pass filters, FELH0750, Thorlabs) and Filter 4 (two 633-nm notch filters, NF-01-633U, Semrock; two 730-nm notch filters, ZET730NF, Chroma Technology; one short-pass filters, FESH0750, Thorlabs). To select the fluorescence from either NIR or red fluorophores, we used Filters 3 and 4 (the top panels in Fig. 3.2b). The filtered fluorescence light was focused onto CCD camera (the pixel size of 26 μm × 26 μm, the quantum efficiency in the range of 700 nm to 850 nm of >0.9, and the standard deviation of the readout noise of 4.7 $e^-$ ; Newton DU920P-BEX2-DD, Andor) with an imaging mirror (the focal length $f_{\mathrm{img}}$ of 1000 mm, protected silver coating, PS-SMCC-1025-2.00-UV, CVI).

In the sample scanning mode (Fig. 3.1a), the reflection and the scattering of the excitation light were blocked by Filter 5. Filter 5 was a filter stack consisting of two 633-nm notch filters (NF01-633U, Semrock) and two 730-nm notch filters (ZET730NF, Chroma Technology). The filtered fluorescence was separated into two parts for the NIR and red signals by the long-pass dichroic mirror (750-nm long-pass dichroic mirror; #69-893, Edmund). The transmitted signal of the NIR fluorophore was filtered by Filter 6 (750-nm long-pass filter; FELH0750, Thorlabs) and was coupled with a multimode fiber (the core diameter of 100 µm; the numerical aperture of 0.12; superguide G SFM100/140, Fiberguide) by an objective lens (UPlanSpo4x, Olympus). The fluorescence photons from the NIR fluorophore were counted by APD1 (SPCM-AQR-16-FC, Perkin Elmer). On the other hand, the reflected signal of the red fluorophore was filtered by Filter 7 (750-nm short-pass filter; FELH0750, Thorlabs) and was coupled with a multimode fiber (the core diameter of 50 µm; the numerical aperture of 0.12; superguide G SFM50/125Y, Fiberguide) by an objective lens (UPlanSpo4x, Olympus). The fluorescence photons of the red fluorophore were counted by APD2 (Count Blue, Laser Components). The number of the fluorescence photons of the NIR and red fluorophores was recorded as a function of the 3D position of the sample, and then the 3D fluorescence image was obtained.

### 3.2.2 Sample condition

Alexa Fluor 750 (Ax750) and sulfo-cyanine 7 (sCy7) molecules were used as the NIR fluorophore. ATTO655 (AT655) was used as the red fluorophore. The autofluorescence of a buffer solution and biological tissues in the wavelength range from 650 nm to 900 nm is 3 – 4 orders of magnitude weaker than that from 400 nm to 500 nm. Consequently, background-free imaging was performed in the present experiments.

Single-stranded DNA (ssDNA) molecules were purchased from Integrated DNA Technologies and Japan Bio Services. Figure 3.4 shows the molecular structures of the double-stranded DNA (dsDNA) molecules. The sequence A (30-base ssDNA) was Ax750-ATC AGT ATC CGA ATC GTG AGC ACC GTA GTA-AT655. The complementary of the sequence A was TAC TAC GGT GCT CAC GAT TCG GAT ACT GAT. The sequence B (60-base ssDNA) was sCy7-ATC AGT GAC GTT GGA GTC CAC GTT CTT TAA TAG TGG ACT CTT GTT CCA AAC TGG GTA GTA-AT655. The complementary of the sequence B was TTTT TAC TAC CCA GTT TGG AAC AAG AGT CCA CTA TTA AAG AAC GTG GAC TCC AAC GTC ACT GAT TTTT. To form the most stable straight helix, 10-nM dual-labeled ssDNA was annealed together with the 500-nM complementary ssDNA molecule in

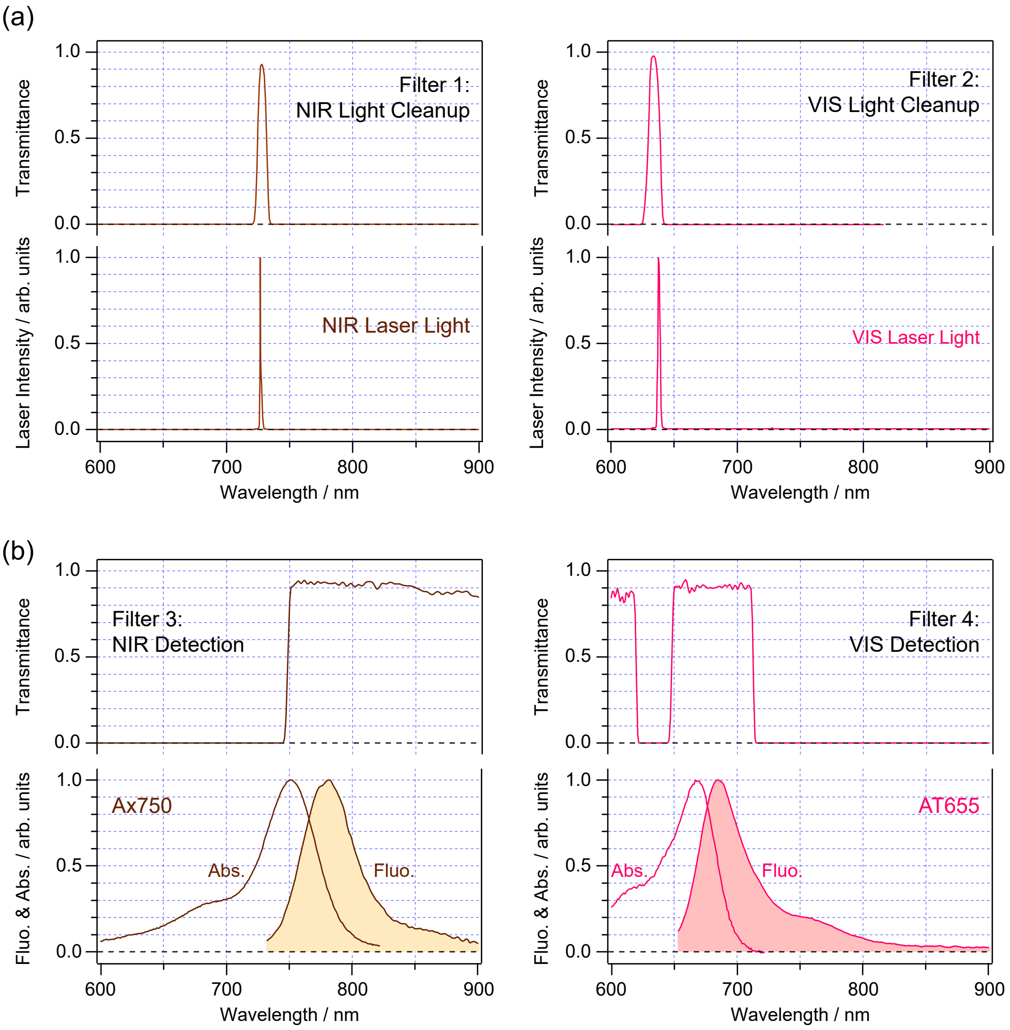

Figure 3.2 Optical filters 1 – 4 for the CCD-localization microscopy. (a, Top) Transmittance of cleanup filters for red and NIR laser lights. These filters are represented by Filters 1 and 2 in Fig. S1a. (a, bottom) Spectrum of these laser lights. (b, top) Detection filters for the fluorescence of the red fluorophore (AT655) and the NIR fluorophore (Ax750 and sCy7) fluorophores. These filters are represented by Filters 3 and 4 in Fig. 3.1a. (b, bottom) Absorption and fluorescence spectra of AT655 and Ax750 in a buffer solution at a temperature of 296 K. The excitation wavelengths of the fluorescence spectra of Ax750 and AT655 were 730 nm and 637 nm, respectively.

a phosphate buffered saline solution at pH = 7 at a temperature of approximately 95 °C. The hot solution was gradually cooled over 120 min to a room temperature. The 10-nM solution of the dsDNA was stored at 4 °C. The stock solution of the dual-labeled dsDNA was diluted to a concentration of 20 pM at pH = 7 in the presence of 5-nM the complementary DNA, phosphate buffered saline, 0.1% Tween 20, and 1% wt/wt polyvinyl alcohol. The 20-pM solution of the dsDNA was spin-coated on a $CaF_2$ substrate with a spinning speed of 3000

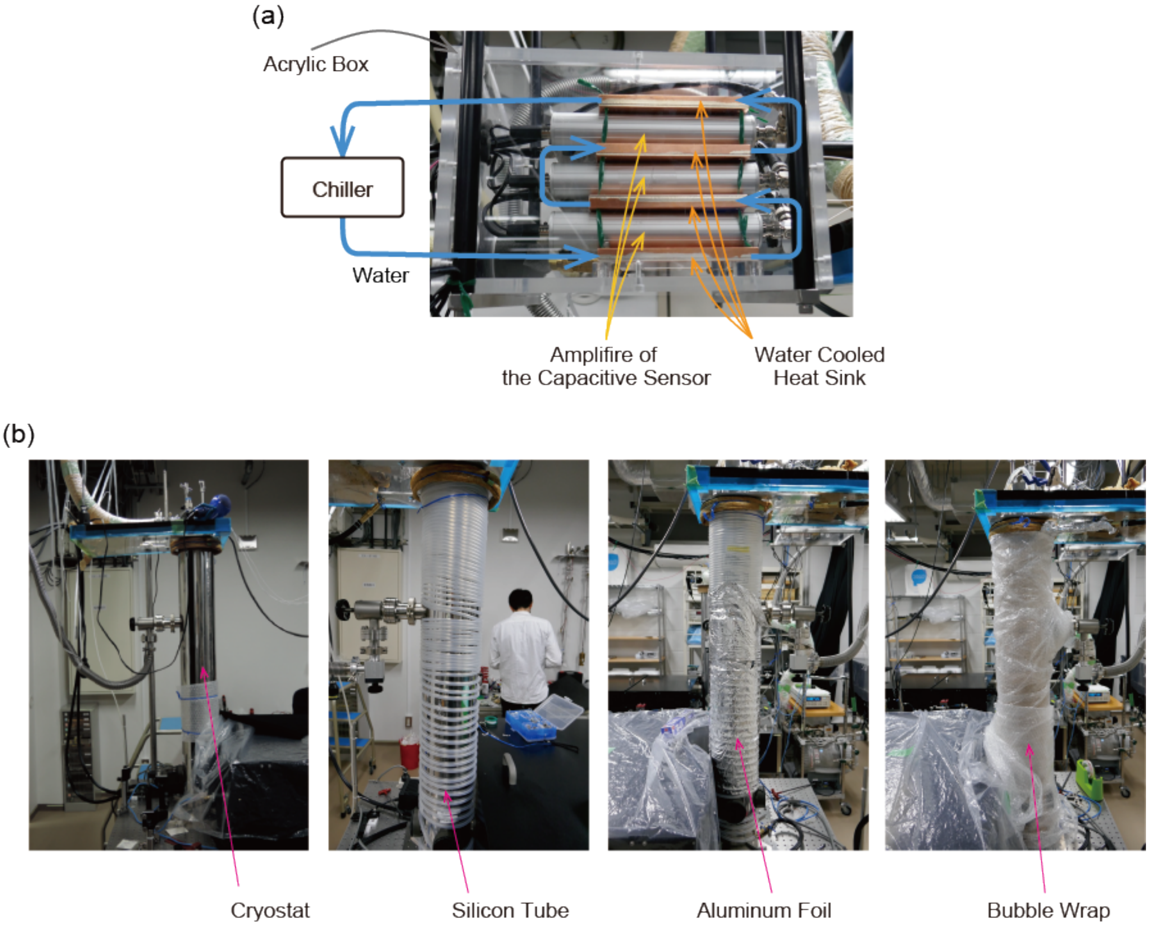

Figure 3.3 Photographs of the water cooled equipments. (a) Water cooled amplifiers of the capacitive sensors monitoring the position of the sample stage. The amplifiers are sandwiched by heat sinks. The heat sinks are kept the temperature by constant-temperature water and keeps the temperature of amplifiers. (b) Circulating-cooling-system for the outer wall of the cryostat. The silicon tube is around the wall and the aluminum foil and the bubble wrap cover the silicon tube. The temperature of the wall is stabilized by the constant-temperature water in the silicon tube.

revolutions per minute for a coat time of 120 s.

### 3.2.3 Spectral-selective imaging of the dual-labeled dsDNA

We show a concept of spectral-selective imaging of the red fluorophore (AT655) and the NIR fluorophore (Ax750 or sCy7) bound to the same dsDNA molecule. Figure S4a shows the absorption spectrum of the dual-labeled 30-bp dsDNA in a buffer solution at pH = 7 at a temperature of 296 K. The spectrum of the dual-labeled 30-bp dsDNA (black curve) is reproduced with a linear combination of the spectrum of an Ax750-labeled ssDNA (filled brown curve) and that of an AT655-labeled ssDNA (filled red curve). Under the irradiation

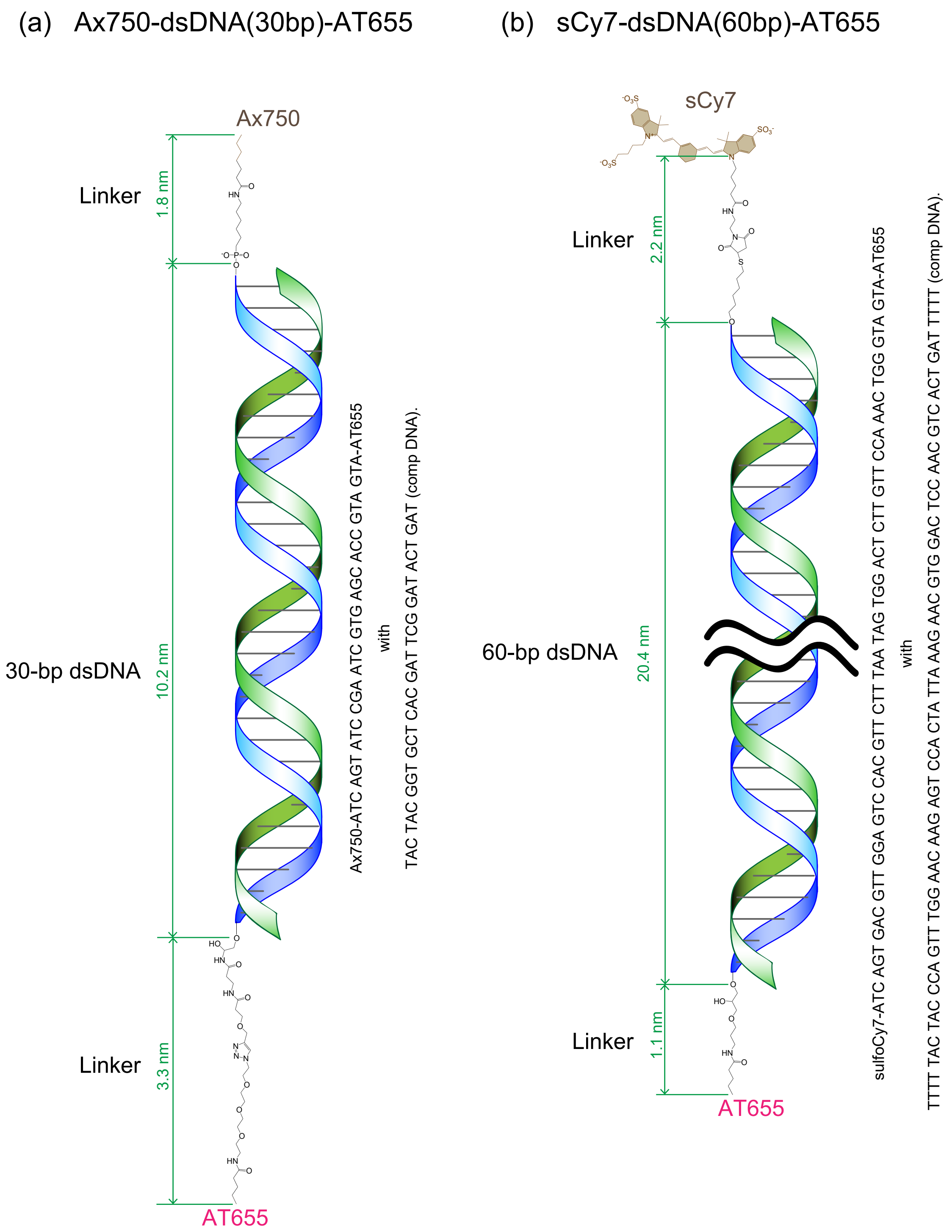

Figure 3.4 Structure of dual-labeled dsDNA for (a) the 30-bp and (b) the 60-bp. The sequences of the dual-labeled DNA and the complementary DNA are depicted on the right side of the structure.

at a $\lambda_{\mathrm{ex}}$ of 637 nm (red arrow in a), AT655 and Ax750 were simultaneously excited, and emitted their fluorescence (Fig. S4b). Therefore, with Filter 4, we blocked not only the excitation light but also the fluorescence of Ax750, and detected only the fluorescence of AT655. Under the irradiation at $\lambda_{\mathrm{ex}}$ of 730 nm (brown arrow in A), only Ax750 was excited and emitted the fluorescence (Fig. S4c). The excitation light was blocked with Filter 3, and the fluorescence of Ax750 was detected.

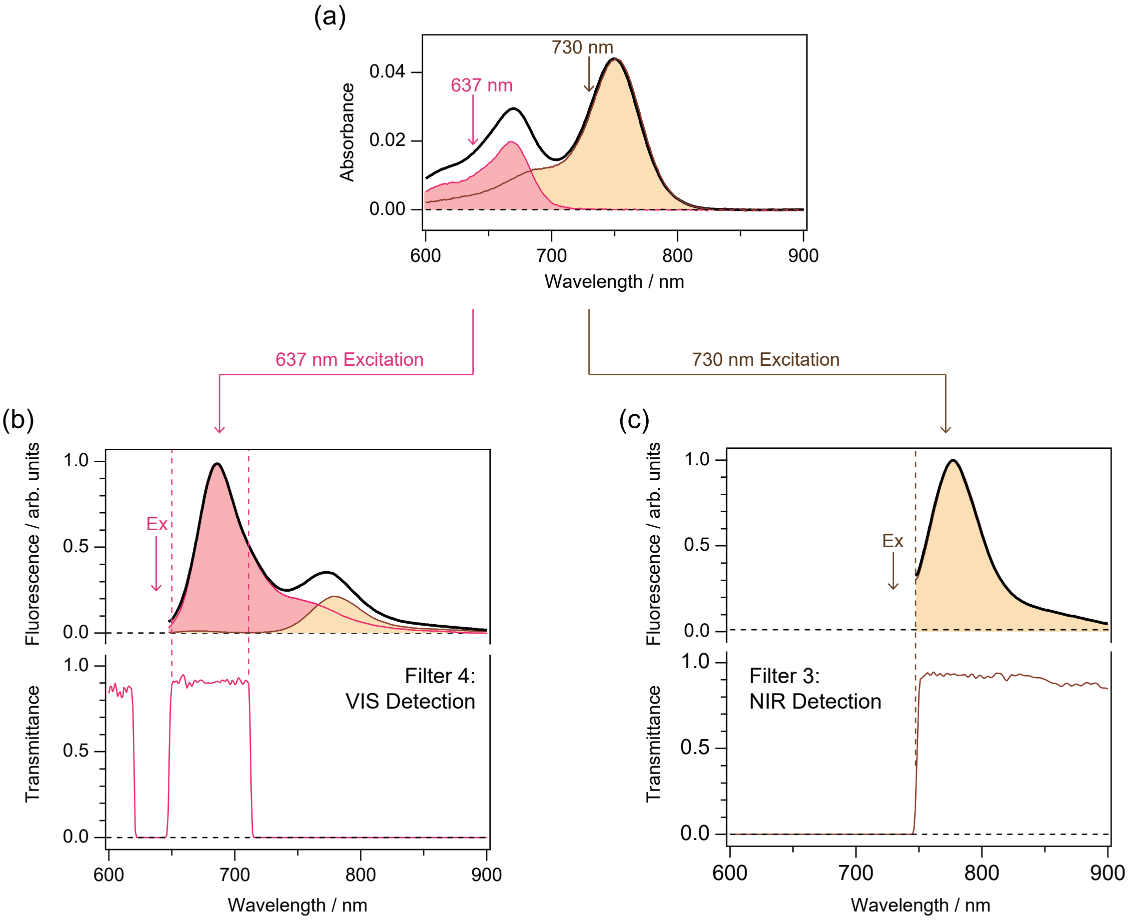

Figure 3.5 Structure of dual-labeled dsDNA for (a) the 30-bp and (b) the 60-bp. The sequences of the dual-labeled DNA and the complementary DNA are depicted on the right side of the structure.

## 3.3 Imaging of single 30-bp dsDNA molecule using 2D localization

The cryo-fluorescence localization of a single 30-bp dsDNA molecule was performed using a 2D image obtained by a far-field cryo-microscope equipped with a charge coupled device (CCD) camera. The dsDNA length is 10.2 nm (Fig. 3.6a). The 5'- and 3'-ends of the dsDNA molecule were labeled with near infrared (NIR) and red fluorophores, respectively (see the chemical structure in Fig. 3.4). Within each single dsDNA molecule, the fluorescence of each of the two different fluorophores can be selectively excited and detected. (see the details in Fig. 3.5). The autofluorescence of a sample in the red region from 650 nm to 900 nm is 3-4 orders of magnitude weaker than in the blue region from 400 nm to 500 nm [23]. Using the red wavelength region, background-free imaging was achieved in the present experiments. Figure 3.6b shows the fluorescence images of the two fluorophores bonded to a single dsDNA molecule at a $z$-position within a diffraction-limited focal depth. The focal depth is $\pm n\lambda/\mathrm{NA}^2$, where $n$ is the refractive index, and $\lambda$ is the wavelength of light. In the present experiment, $n$ was 1.03, $\lambda$ was 700 nm, and NA was 0.99, so $\Delta z$ was ±700 nm. The $xy$-centroid of each fluorophore was determined by fitting the central disk to a 2D Gaussian function. The $xy$-coordinates of the two fluorophores' centroids had an offset of approximately 20 nm, which is common in the measurements of different DNA molecules. The 20-nm offset was mainly due to the $xy$-chromatic aberration between the fluorescence wavelengths because the sample position was moved to select a target molecule without changing the microscope alignment. The chromatic aberration might have been caused by the parallelism error of optical windows and optical filters. This chromatic aberration offset was subtracted as a constant value, and $D_{xy}$ was determined from the $xy$-centroids of two fluorophores. Figure 3.6c shows a histogram of $D_{xy}$ for 96 molecules. For each fluorophore, $10^5$ fluorescence photons were acquired in 3 min (the exposure and readout times were 10 s and 3 s, respectively, and the >20 images were averaged). The $xy$-localization precision of each fluorophore ($\Delta_{xy}$) was 1 nm (Fig. 3.6d). Although the dsDNA distance was 10.2 nm, $D_{xy}$ was distributed from 0 to 50 nm. This $xy$-mislocalization was likely to due to a dipole orientation effect. When orientationally fixed, a single fluorophore should be regarded as an anisotropic emitter [14, 15]. Depending on the dipole orientation of a fluorophore with respect to the focal plane, the major axis of the point spread function (PSF) is tilted from the $z$-direction [18–20].

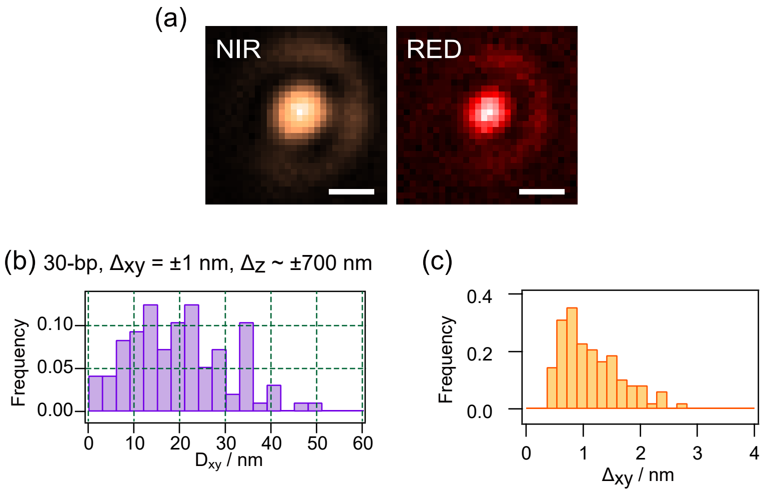

Figure 3.6 Cryo-fluorescence microscopy of two fluorophores bonded to a single 30-bp dsDNA molecule, using 2D localization with $\Delta_{xy}$ equal to ± 1 nm and $\Delta_z$ equal to approximately ±700 nm. (a) Structure of the dual-labeled dsDNA molecule. (b) Fluorescence images of the NIR and red fluorophores at 1.8 K (scale bar of 500 nm). (c) Histogram of $D_{xy}$ for the 96 molecules of the 10-nm-long dsDNA molecule determined from the two images at a $z$-position within the focal depth ($\Delta_z \sim \pm 700$ nm). (d) Histogram of the $xy$-localization precision of each fluorophore.

## 3.4 Sample scanning imaging of 30-bp dsDNA at 296 K

As a preliminary step, we performed colocalization of the two fluorophores using the sample-scanning 3D image at 296 K. To confirm the PSF tilt under the present conditions, the individual 3D PSFs of the dual-labeled dsDNA molecule were observed using the reflecting cryo-microscope; this observation was performed at 296 K because the blinking noise at 296 K was smaller than at 1.8 K. The top panels in Fig. 3.7 show a sample-scanning fluorescence image of dual-labeled dsDNA molecule at 296 K obtained using circularly polarized excitation light. A $10^{-11}$ M solution of dsDNA with 1% polyvinyl alcohol was coated onto a $CaF_2$ substrate. The solution concentration was adjusted for the fluorescence spots to be well-separated in the images [24]. The dsDNA molecules were fixed orientationally and spatially. Since the dsDNA length (10.2 nm) is much smaller than the spot size, the spots of the two fluorophores bonded to a common DNA molecule appear at the same position in both images; half the fluorescence spots were observed in both images (spots observed in only one image are marked with sky-blue asterisks). According to the results of high-performance liquid chromatography (HPLC) analysis, >80% of the dsDNA molecule was labeled with both fluorophores, and one of the two fluorophores was ikely in a dark state. The middle and bottom panels in Fig. 3.7 show the $zx$- and $zy$-fluorescence images for the single dsDNA molecule at $(x, y)$ = (2400 nm, 1600 nm) in the top panels. The PSFs of the two fluorophores in the $zx$-image were nearly parallel to the $z$-axis, whereas they were tilted in the $zy$-image. The PSF tilt angles in the $zy$-plane for the NIR and red fluorophores were $\phi_{zy;\mathrm{N}}$ = 0.05 rad and $\phi_{zy;\mathrm{R}}$ = -0.09 rad, respectively.

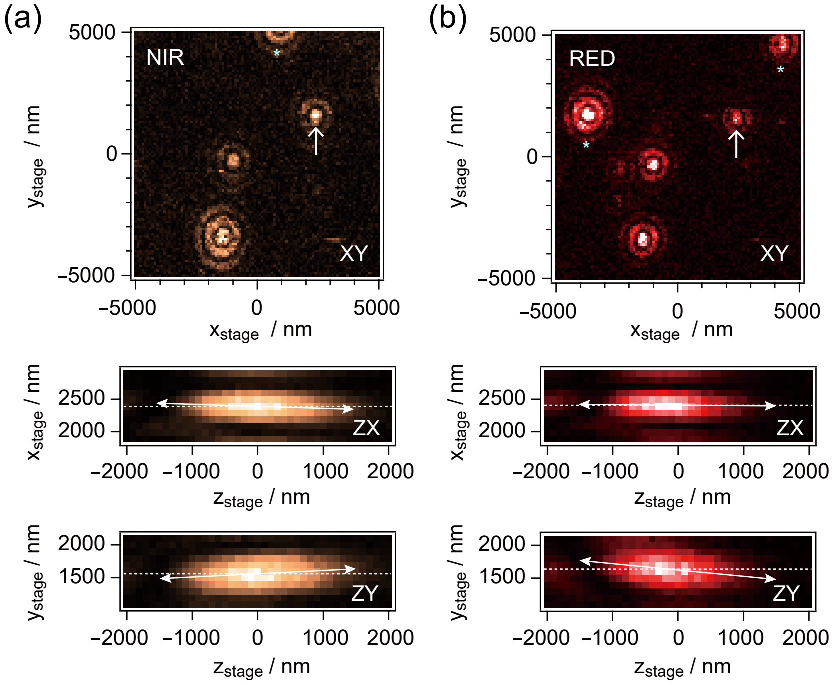

Figure 3.7 3D PSFs of the (a) NIR and (b) red fluorophores bonded to a single dsDNA molecule at 296 K obtained using sample-scanning far-field microscopy. The top panels are the $xy$-fluorescence images. The middle and bottom panels show the $zx$- and $zy$-PSFs of the single dsDNA molecule that is indicated by single-headed arrows in the top panels. The major axes of PSFs are indicated by double-headed arrows for clarification.

Using the sample-scanning, the localization precision in all directions was approximately 30 nm because of the blinking noise and photobleaching. Blinking noise is known to be absent in a CCD detection [11], and under cryogenic conditions, photobleaching of fluorophores is drastically suppressed [25]. CCD-equipped cryo-microscopy can collect $10^6$ fluorescence photons from a single fluorophore under the blinking-free conditions. Thus, we performed the 3D cryo-localization microscopy of the two fluorophores using a CCD camera.

## 3.5 Imaging of single 30-bp dsDNA molecule using 3D localization

### 3.5.1 Experimental procedure for 3D localization microscopy of two fluorophores

The two-color fluorescence image of the dual-labeled dsDNA was measured at the excitation wavelengths $\lambda_{\mathrm{ex}}$ of 637 nm and 730 nm at a temperature of 1.8 K. To a suppress background emission due to the autofluorescence of a sample, the excitation light was tightly focused on the sample; thus, the wide-field image such as the top panels of Fig. 3.7 was measured by raster-type sample-scanning. To separate the spots well, the concentration of the dual-labeled dsDNA in the solution used for the spin coat was set to approximately 20 pM. As a result, the individual dsDNA molecules were sparsely observed as diffraction-limited fluorescence spots (see the top panel in Fig. 3.7). Since the length of the 30-bp dsDNA (or the 60-bp dsDNA) was 10 nm (or 20 nm), the fluorescence spots of the two fluorophores bonded to the same dsDNA appeared at almost the same position. We searched for a target dsDNA molecule that simultaneously emitted the fluorescence in the both images. The target DNA molecule was brought to the laser focus by moving the cryo-stage. The $xyz$-position was actively locked at a nanometer precision. The error signal for the locking was generated from the cryo-capacitive sensor. For each fluorophore, the 19 fluorescence images were measured by a CCD camera in the range of the $z_{\mathrm{stage}}$ from −900 nm to 900 nm at the 100 nm intervals. At one $z$-position, an Ax750 (or sCy7) image and an AT655 image were acquired alternately. The 38 images were acquired in order to determine the 3D PSF of the two fluorophores. The exposure and readout times of one image were 10 s and 3 s, respectively. The observation time was approximately 500 s. The magnified image, i.e., the raw data from the CCD camera ($x_{\mathrm{CCD;pixel}}$, $y_{\mathrm{CCD;pixel}}$), was converted to the real-sized image of the sample ($x_{\mathrm{CCD}}$, $y_{\mathrm{CCD}}$) as follows.

$$x_{\mathrm{CCD}} = x_{\mathrm{CCD;pixel}} \cdot a/M_{xy} \quad \mathit{and} \quad y_{\mathrm{CCD}} = y_{\mathrm{CCD;pixel}} \cdot a/M_{xy} \tag{3.1}$$

where a is the CCD pixel size of 26 µm, and $M_{xy}$ is the lateral magnification of the cryo-microscope ($M_{xy} = f_{\mathrm{obj}}/f_{\mathrm{img}} = 490$).

Figure 3.8a shows the experimental procedure for the $xy$-localization of individual fluorophores. The fluorescence images of a single red fluorophore were acquired at the 19 positions of the $z_{\mathrm{stage}}$, $I_{\mathrm{R}}(x_{\mathrm{CCD}}, y_{\mathrm{CCD}}, z_{\mathrm{stage}})$. For the $xy$-centroid determination, only the central disk was used for the Gaussian fitting. Concentric rings in the image were masked with a window function $A_{xy}(x_{\mathrm{CCD}}, y_{\mathrm{CCD}}, z_{\mathrm{stage}})$. To determine $A_{xy}$ at each $z$-position, the width of the central disk in unit of standard deviation ($\sigma_{\mathrm{disk}}$) was predetermined by the 2D Gaussian fitting of the central disk of $I_{\mathrm{R}}$. The window function was an oval with the radius of 2.5 $\sigma_{\mathrm{disk}}$. To determine the $xy$-centroids, the masked image, $I_{\mathrm{R}} \times A_{xy}$, was fitted to a 2D Gaussian function. The 19 images for the NIR fluorophore were analyzed in the same manner as that used for the red fluorophore.

Figure 3.8b shows the experimental procedure for the $z$-localization of individual fluorophores. The same fluorescence images for the $xy$-localization were used for the $z$-localization. The widths of low spatial frequency components, $s_x(z_{\mathrm{stage}})$ and $s_x(z_{\mathrm{stage}})$, contain information about the $z$-position of the fluorophore [5]. The widths of $s_x$ and $s_y$ cannot be directly derived from the fitting of the images because a concentric pattern led the fitting to false minima. Therefore, at each $z$-position, the fluorescence image of $I_{\mathrm{R}}(x_{\mathrm{CCD}}, y_{\mathrm{CCD}}, z_{\mathrm{stage}})$ was Fourier-transformed to $L_{\mathrm{R}}(u, v, z_{\mathrm{stage}})$ in reciprocal space, where $u$ and $v$ are spatial frequencies for the $x$- and $y$-directions, respectively. Before the transformation, the apodization function of $A_z(x_{\mathrm{CCD}}, y_{\mathrm{CCD}})$ was multiplied to $I_{\mathrm{R}}(x_{\mathrm{CCD}}, y_{\mathrm{CCD}}, z_{\mathrm{stage}})$ in order to minimize the background from the readout noise of the CCD. The apodization function was an Airy function with the radius of the first dark ring of 2.5 µm multiplied by a window function. The multiplied window function was a circle with a radius of 2.5 µm. The apodization function $A_z(x_{\mathrm{CCD}}, y_{\mathrm{CCD}})$ was common to the data at all the $z$-positions. The apodized image of $I_{\mathrm{R}} \times A_z$ was Fourier-transformed to the square of the spatial frequency domain function $|L_{\mathrm{R}}(u, v, z_{\mathrm{stage}})|^2$. As seen in the image, the low frequency component appeared as a sharp peak centered at the zero frequency. The width of $|L_{\mathrm{R}}(u, v, z_{\mathrm{stage}})|^2$ was calculated by the fitting of a 2D Gaussian function $|F(u, v)|^2$. The function of $|F(u, v)|^2$ is given by

$$|F(u,v)|^2 = \left| A \exp\left( -\frac{1}{2} \left\{ \left( \frac{u}{s_{u;\mathrm{conv}}} \right)^2 + \left( \frac{v}{s_{v;\mathrm{conv}}} \right)^2 \right\} \right) \right|^2 , \tag{3.2}$$

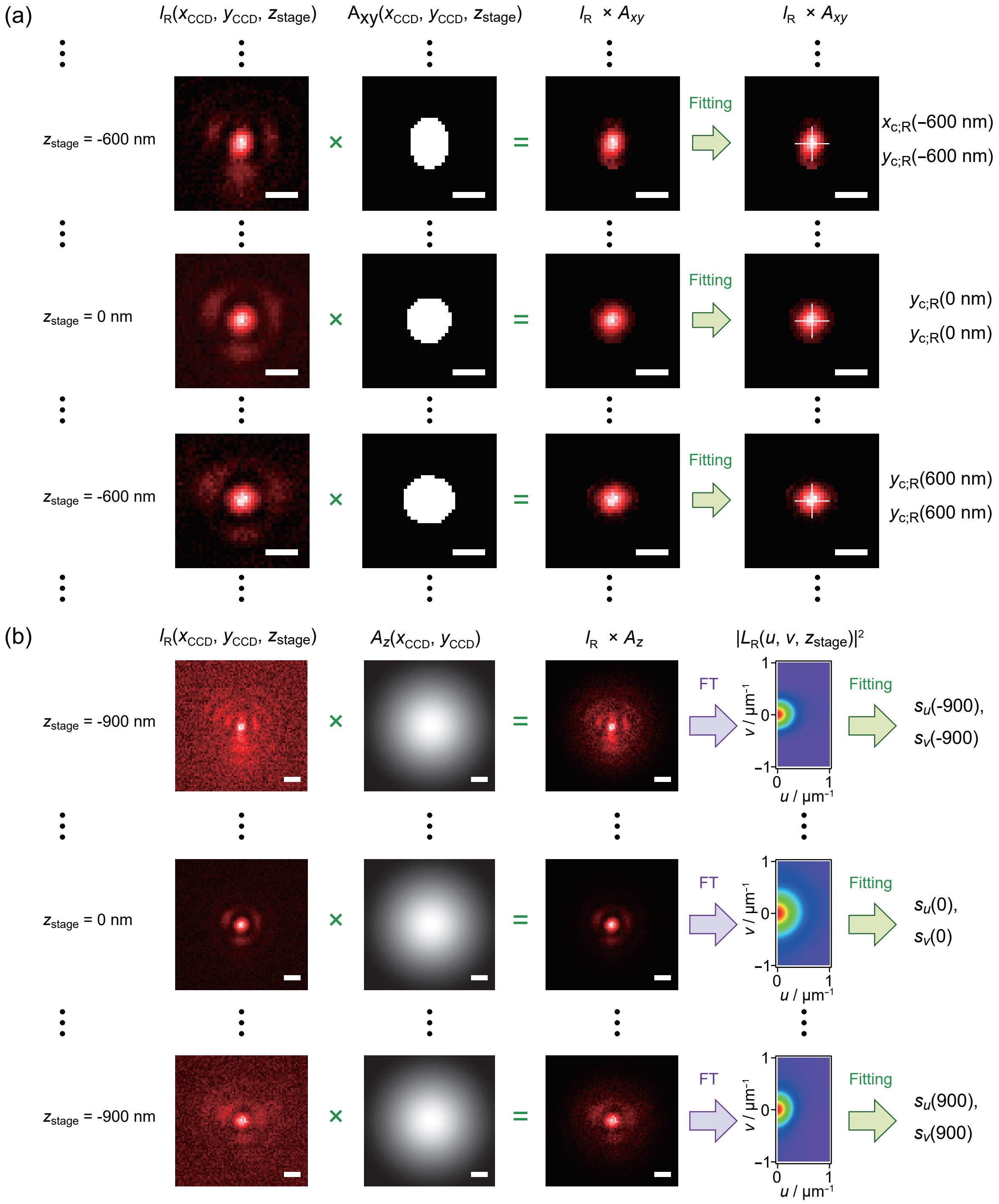

Figure 3.8 Experimental procedure for 3D localization of a single fluorophore. (a) The $xy$-localization and (b) $z$-localization. Here, $I_R(x, y, z_{stage})$ represents the fluorescence image of a single red fluorophore at a position of the $z_{stage}$. $A_{xy}(x, y, z_{stage})$ and $A_z(x, y)$ represent the masks for the $xy$- and $z$-localizations, respectively. $|L_R(u, v, z_{stage}|^2$ is a square of the Fourier-transformed image of $I_R(x, y, z_{stage}) \times A_z(x, y)$. The scale bars of $I_R(x, y, z_{stage})$, $A_{xy}(x, y)$ and $A_z(x, y)$ represent 500 nm.

where $s_{u;\mathrm{conv}}$ and $s_{v;\mathrm{conv}}$ are the calculated width in a unit of standard deviation. In order to block the higher-spatial frequency component, the fitting was conducted in a region near the zero frequency ($u \times v = 0.001\ \mathrm{nm}^{-1} \times\pm\ 0.001\ \mathrm{nm}^{-1}$). The calculated width of $s_{u;\mathrm{conv}}$ (or $s_{v;\mathrm{conv}}$) was a convolution of $s_u$ (or $s_v$) with the apodization function $A_z$. The widths of $s_u$ and $s_v$ were calculated by the deconvolution of $A_z$. The widths in the real and reciprocal spaces are given by

$$s_x s_u = \frac{1}{2\pi} \quad \text{and} \quad s_y s_v = \frac{1}{2\pi}. \tag{3.3}$$

The widths of $s_x$ and $s_y$ were plotted as a function of the $z_{\mathrm{stage}}$ (see the top panel of Figs. 3.9b and 3.9d). The minima of the curve correspond to the $z$-position of the red fluorophore ($z_{x;\mathrm{c;R}}, z_{y;\mathrm{c;R}}$). The 19 images for the NIR fluorophore were analyzed in the same manner as that used for the red fluorophore.

Two examples of the experimental data of the $xyz$-localization are shown in Fig. 3.9. The fluorescence images ($l_\mathrm{R}$ and $l_\mathrm{N}$) and the Fourier-transformed images of $|L_\mathrm{R}|^2$ and $|L_\mathrm{N}|^2$ at the 7 $z_{\mathrm{stage}}$-positions are depicted in (a) and (c). The values of $s_x$, $s_y$, $x_\mathrm{c}$, and $y_\mathrm{c}$ evaluated from these images are shown in (b) and (d). The widths of $s_x$ and $s_y$ as a function of the $z_{\mathrm{stage}}$ (circles and triangles) has been well-fitted with a Gaussian function (solid curves). Consequently, we evaluated the $z$-positions of the fluorophores ($z_{x;\mathrm{c;R}}$, $z_{x;\mathrm{c;N}}$, $z_{y;\mathrm{c;R}}$, and $z_{y;\mathrm{c;N}}$). The values of $z_{x;\mathrm{c;R}}$ and $z_{x;\mathrm{c;N}}$ correspond to the $z$-position of the red fluorophore and NIR fluorophore, respectively, on the $zx$-plane. The values of $z_{y;\mathrm{c;R}}$ and $z_{y;\mathrm{c;N}}$ correspond to the $z$-position of the red fluorophore and NIR fluorophore, respectively, on the $zy$-plane.

The $xy$-centroid of the fluorophores ($x_{\mathrm{c;R}}, x_{\mathrm{c;N}}, y_{\mathrm{c;R}}, y_{\mathrm{c;N}}$) depends on the $z_{\mathrm{stage}}$, the $xy$-centroid around $z_{\mathrm{stage}} = 0$ nm can be fitted by a linear function; consequently the $xy$-centroid of the two fluorophores at $z_{\mathrm{stage}} = z_{x;\mathrm{c;R}}$, $z_{x;\mathrm{c;N}}$, $z_{y;\mathrm{c;R}}$, and $z_{y;\mathrm{c;N}}$ are evaluated to $x_{\mathrm{c;R}}(z_{x;\mathrm{c;R}})$, $x_{\mathrm{c;N}}(z_{x;\mathrm{c;N}})$, $y_{\mathrm{c;R}}(z_{y;\mathrm{c;R}})$, and $y_{\mathrm{c;N}}(z_{y;\mathrm{c;N}})$, respectively. The distance between the red and NIR fluorophores in centroid are given by

$$\delta x_{\mathrm{c;RN}} = x_{\mathrm{c;R}}(z_{x;\mathrm{c;R}}) - x_{\mathrm{c;N}(z_{x;c;N})} \tag{3.4}$$

$$\delta y_{\mathrm{c;RN}} = y_{\mathrm{c;R}}(z_{y;\mathrm{c;R}}) - y_{\mathrm{c;N}(z_{y;c;N})}. \tag{3.5}$$

To obtain the localized position of the fluorophores ($\delta x_{\mathrm{loc;RN}}, \delta y_{\mathrm{loc;RN}}$), we must correct two

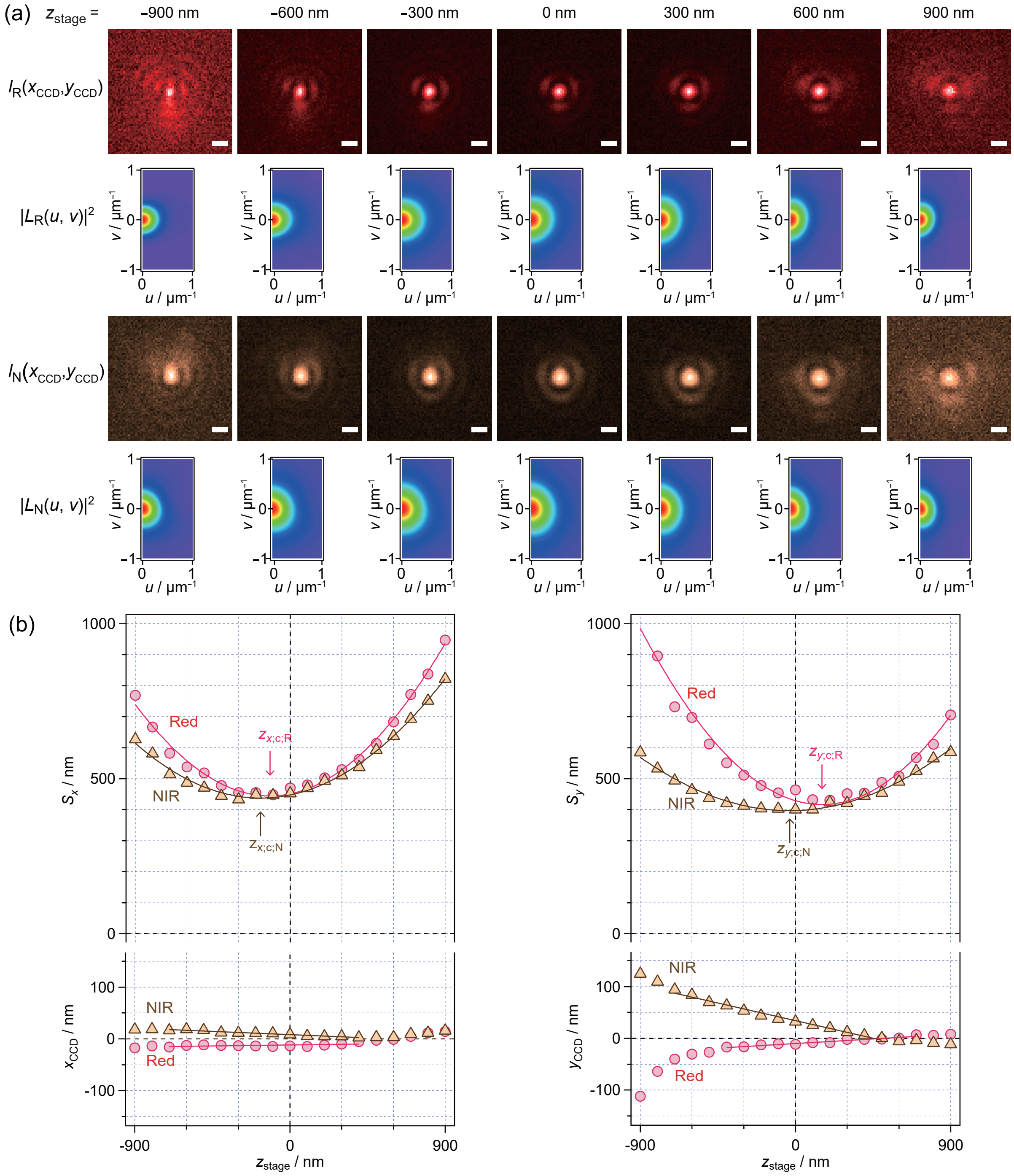

Figure 3.9 Experimental data for 3D localization of an individual dual-labeled 30-bp dsDNA molecule shown in Fig. 3.13 (No.13). (a) Fluorescence images of the red and NIR fluorophores, $l_\mathrm{R}(x, y, z_\mathrm{stage})$ and $l_\mathrm{N}(x, y, z_\mathrm{stage})$, and their Fourier-transformed images, $|L_\mathrm{R}(u, v, z_\mathrm{stage})|^2$ and $|L_\mathrm{N}(u, v, z_\mathrm{stage})|^2$, respectively. The scale bars of $l_\mathrm{R}(x, y)$ and $l_\mathrm{N}(x, y)$ represent 500 nm. (b) The width (standard deviation) of the low frequency component ($s_x$ and $s_y$) and the $xy$-centroid position at $z_\mathrm{stage}$-positions.

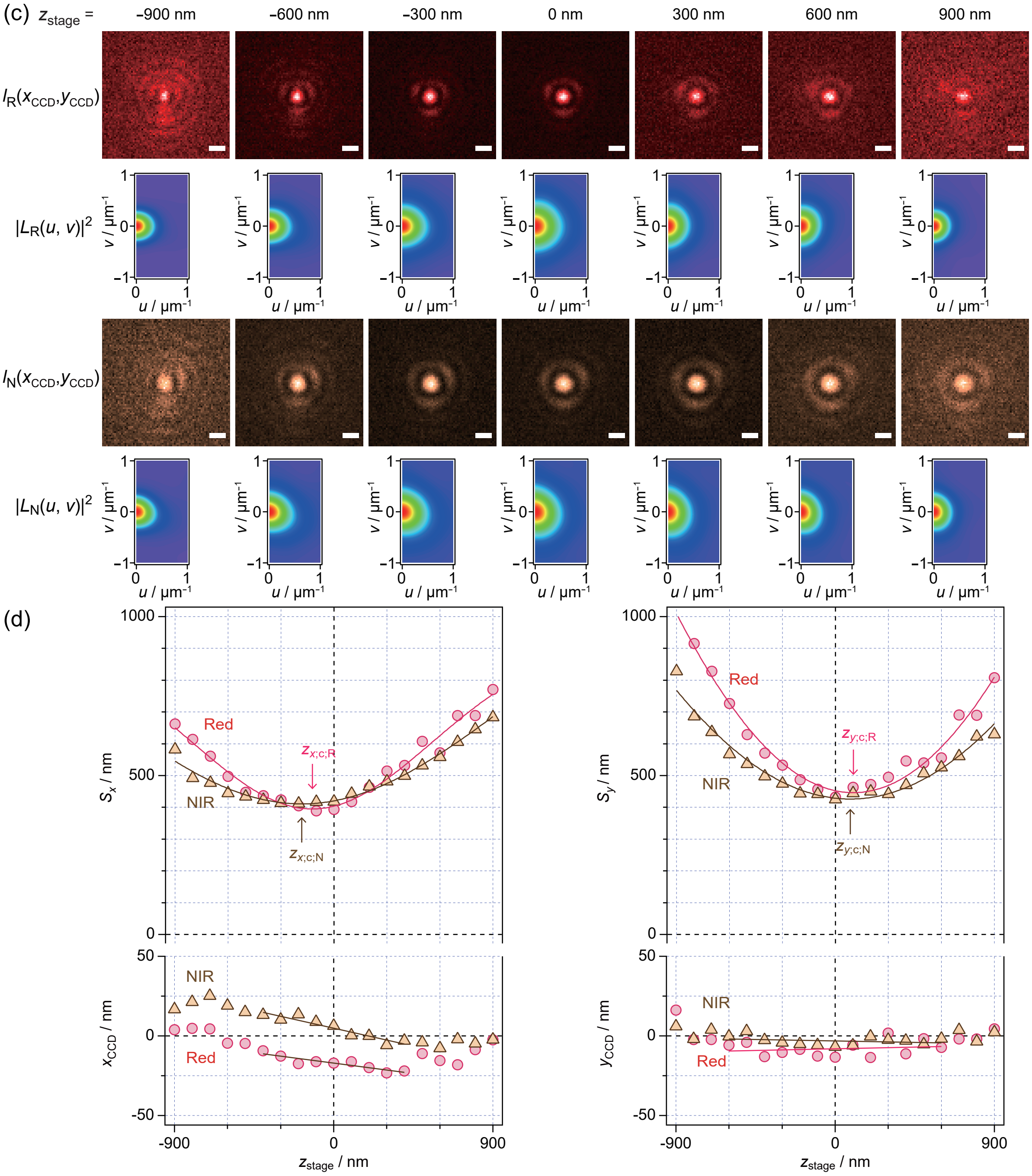

Figure 3.9 (continued). Experimental data for 3D localization of an individual dual-labeled 30-bp dsDNA molecule Fig. 3.13 (No.17). (a) Fluorescence images of the red and NIR fluorophores, $I_R(x, y, z_{stage})$ and $I_N(x, y, z_{stage})$, and their Fourier-transformed images, $|L_R(u, v, z_{stage})|^2$ and $|L_N(u, v, z_{stage})|^2$, respectively. The scale bars of $I_R(x, y)$ and $I_N(x, y)$ represent 500 nm. (b) The width (standard deviation) of the low frequency component ($s_x$ and $s_y$) and the $xy$-centroid position at $z_{stage}$-positions.

experimental errors;

$$\delta x_{\mathrm{loc;RN}} = \delta x_{\mathrm{c;RN}} + \delta x_{\mathrm{chroma;RN}} + \delta x_{\mathrm{distor;RN}}(\delta\phi_{zx;\mathrm{RN}}) \tag{3.6}$$

$$\delta y_{\mathrm{loc;RN}} = \delta y_{\mathrm{c;RN}} + \delta y_{\mathrm{chroma;RN}} + \delta y_{\mathrm{distor;RN}}(\delta\phi_{zy;\mathrm{RN}}). \tag{3.7}$$

The second terms on the right-hand side are an $xy$-shift caused by $xy$-chromatic aberration between the fluorescence wavelengths of the red and NIR fluorophores. The $xy$-chromatic aberration has been described previously [12, 13]. In our cryo-fluorescence imaging, the sample was moved without changing the optical alignment of the cryo-microscope. Therefore, the second term must be constant on each image. The third terms on the right-hand side of equations 3.6 and 3.7 are systematic errors due to the PSF distortion caused by dipole orientation effect [14, 15]. Figure 3.10a shows the fluorescence image of the individual AT655 molecules at a temperature of 1.8 K. The PSF tilt angles were $(\phi_{zx;\mathrm{R}}, \phi_{zy;\mathrm{R}}) = (-0.007, 0.013)$ in the left image, (0.006, 0.117) in the center image, and (−0.145, −0.089) in the right image. At the higher tilt angles, the fluorescence spots were apparently distorted, and the central disk was together with the concentric ring. We excluded data for each fluorophore where one of the tilt angles $(\phi_{zx;\mathrm{R}}, \phi_{zy;\mathrm{R}}, \phi_{zx;\mathrm{N}}, \phi_{zy;\mathrm{N}})$ was $> 0.07$ rad ($3\sigma$ of the tilt angles in Fig. 3.11). The 20 molecules of the 30-bp dsDNA could be used out of the 21 molecules, and the 46 molecules of the 60-bp dsDNA could be used out of the 51 molecules.

The fluorophores were randomly oriented on the lateral plane; consequently $\sum_i \delta x_{\mathrm{loc;RN;i}} \sim 0$ and $\sum_i \delta y_{\mathrm{loc;RN;i}} \sim 0$ when the numbers of data (i) were large enough. Figure 3.10 shows $\delta x_{\mathrm{c;RN}}$ and $\delta y_{\mathrm{c;RN}}$ as a function of $\delta\phi_{zx;\mathrm{RN}}$ and $\delta\phi_{zy;\mathrm{RN}}$ for the data from the 20 molecules of the 30-bp dsDNA. The distance between the two fluorophores $(\delta x_{\mathrm{c;RN}}, \delta y_{\mathrm{c;RN}})$ were approximated to be linearly proportional to the tilt angle of $\delta\phi_{zx;\mathrm{RN}}$ and $\delta\phi_{zy;\mathrm{RN}}$. Equations (3.6) and (3.7) can be approximated as follows:

$$\delta x_{\mathrm{loc;RN}} = \delta x_{\mathrm{c;RN}} + 18.4\ \mathrm{nm} - 374\delta\phi_{\mathrm{zx;RN}}\ \mathrm{rad}^{-1}\mathrm{nm} \tag{3.8}$$

$$\delta y_{\mathrm{loc;RN}} = \delta y_{\mathrm{c;RN}} + 0.5\ \mathrm{nm} + 374\delta\phi_{\mathrm{zy;RN}}\ \mathrm{rad}^{-1}\mathrm{nm}. \tag{3.9}$$

By using the equations of (3.8) and (3.9), we evaluated the localized position of $\delta x_{\mathrm{loc;RN}}$ and $\delta y_{\mathrm{loc;RN}}$. The parameters for the correction of the 60-bp dsDNA were determined from the data from the 20 molecules of the 30-bp dsDNA shown in Fig. 3.10b.

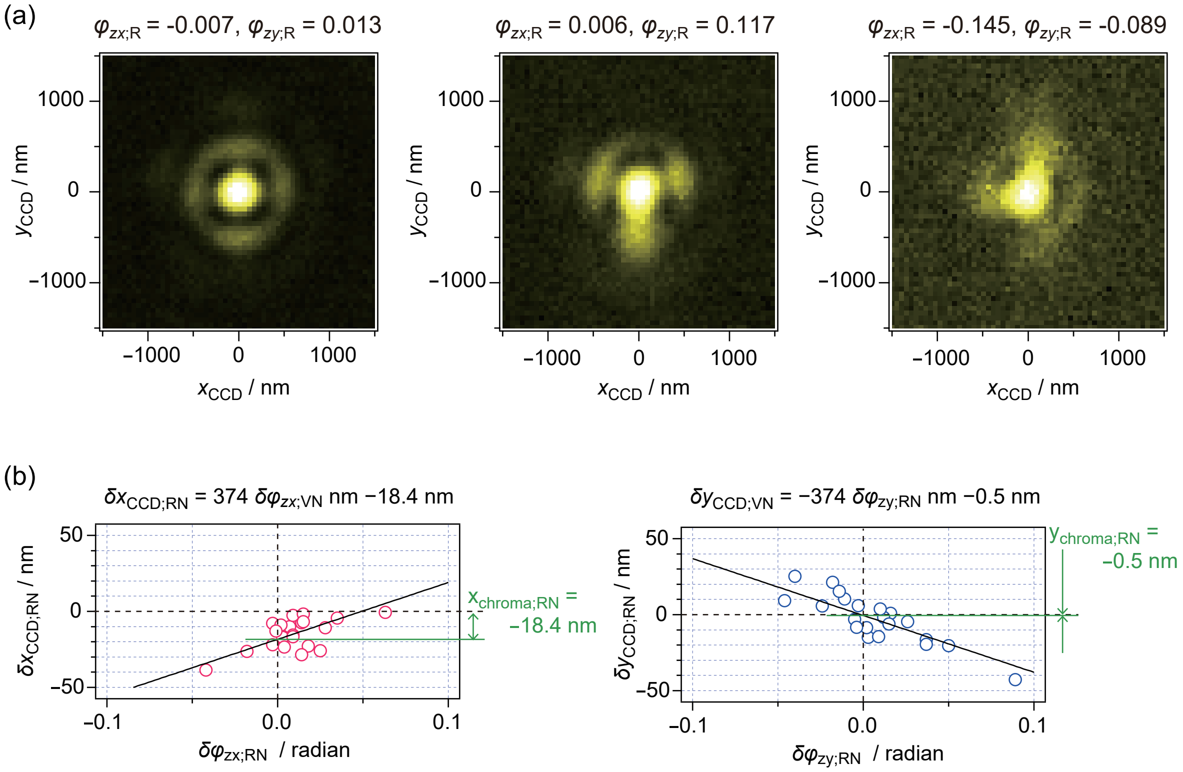

Figure 3.10 PSF distortion and lateral chromatic aberration. (a) The CCD fluorescence images of individual AT655 molecules at $z_{\text{stage}} \sim 0$ nm at 1.8 K. The tilt angles of the 3D PSFs were (left) $\phi_{zx;\text{R}} = -0.007$ rad and $\phi_{zy;\text{R}} = -0.013$; (middle) $\phi_{zx;\text{R}} = 0.006$ rad and $\phi_{zy;\text{R}} = 0.117$ rad; and (right) $\phi_{zx;\text{R}} = -0.145$ rad and $\phi_{zy;\text{R}} = -0.089$ rad. (b) The relative coordinate, $\delta x_{\text{c;RN}}$ and $\delta y_{\text{c;RN}}$, as a function of the difference of the PSF tilt angles, $\delta\phi_{zx;\text{RN}}$ and $\delta\phi_{zy;\text{RN}}$.

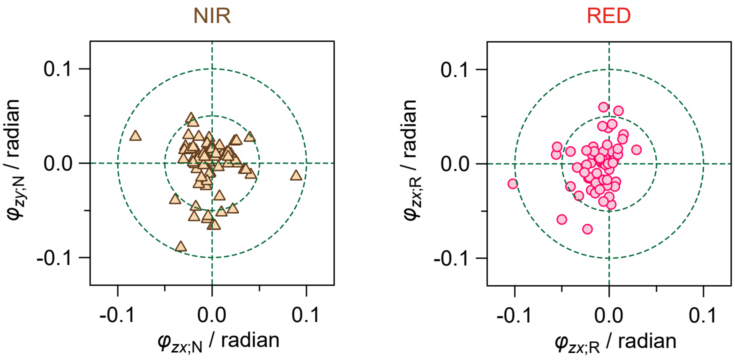

Figure 3.11 PSF tilt angles for the 72 NIR and red fluorophores. Green circles of radii 0.05 and 0.10 rad are depicted for clarification.

### 3.5.2 Evaluation for the localization errors in the *xyz*-directions

We evaluate the localization errors of individual dsDNA molecules. The data are summarized in Fig. 3.12. For two fluorophores, it is necessary to obtain 38 images to perform the 3D localization. Among the dsDNA molecules imaged, we used the data for the dsDNA molecules that were able to perform the 3D localization process more than four times. The 14 molecules of the 30-bp dsDNA molecules out of the 20 molecules could be used for the evaluation, and the thirty-one 60-bp dsDNA could be used out of the 46 molecules.

For each dsDNA molecule, we calculated the average of the *xyz*-positions, $\langle \delta x_{\mathrm{c;RN}} \rangle$, $\langle \delta y_{\mathrm{c;RN}} \rangle$, and $\langle \delta z_{\mathrm{c;RN}} \rangle$, where $\delta z_{\mathrm{c;RN}}$ is $(z_{x;\mathrm{c;R}} - z_{x;\mathrm{c;N}})/2 + (z_{y;\mathrm{c;R}} - z_{y;\mathrm{c;N}})/2$. For each molecule, the deviation is calculated by each determined distance ($\delta x_{\mathrm{c;RN}}$, $\delta y_{\mathrm{c;RN}}$, $\delta z_{\mathrm{c;RN}}$) minus their average: $\delta x_{\mathrm{c;RN}} - \langle \delta x_{\mathrm{c;RN}} \rangle$, $\delta y_{\mathrm{c;RN}} - \langle \delta y_{\mathrm{c;RN}} \rangle$, and $\delta z_{\mathrm{c;RN}} - \langle \delta z_{\mathrm{c;RN}} \rangle$. The histograms of the standard deviation of the individual fluorophores are shown in Fig. 3.12. For the 30-bp dsDNA molecules, the standard deviation of the distance between the two fluorophores was 1.5 nm in $x$ ($\sigma_{x;\mathrm{RN}}$), 1.9 nm in $y$ ($\sigma_{y;\mathrm{RN}}$), and 25 nm in $z$ ($\sigma_{z;\mathrm{RN}}$). The average of the number of the 3D localization measurements of each dsDNA molecule was 3.7. The average localization precision, in the unit of standard error, of each fluorophore was estimated to 0.65 nm ($\Delta_x$), 0.85 nm ($\Delta_y$), and 11 nm ($\Delta_z$). For the 60-bp dsDNA molecules, the standard deviation of the distance between the two fluorophores was 1.7 nm in $x$ ($\sigma_{x;\mathrm{RN}}$), 1.5 nm in $y$ ($\sigma_{y;\mathrm{RN}}$), and 19 nm in $z$ ($\sigma_{z;\mathrm{RN}}$). The average of the number of the 3D localization measurements was 3.9. The average localization precision of each fluorophore was estimated to 0.71 nm ($\Delta_x$), 0.85 nm ($\Delta_y$), and 7.8 nm ($\Delta_z$).

### 3.5.3 Localization images of the individual dsDNA using 3D localization

Figure 3.13a shows a coordinate system on the *xy*-plane. $D_{xy}$ represents the distance between the two fluorophores on the *xy*-plane, and $\theta_{xy}$ represents the angle between the two fluorophores on the *xy*-plane. Figure 3.13b shows the *xy*-localization images of the 20 molecules of the 30-bp dsDNA. The *xy*-images were determined from the 3D localization. The determined parameters are shown at the bottom of each image. The number of the 3D localization processes represents the 'data set'. $N_{\mathrm{R}}$ and $N_{\mathrm{N}}$ are the detected numbers of total photons to measure one 3D PSF for the red and NIR fluorophores, respectively. The

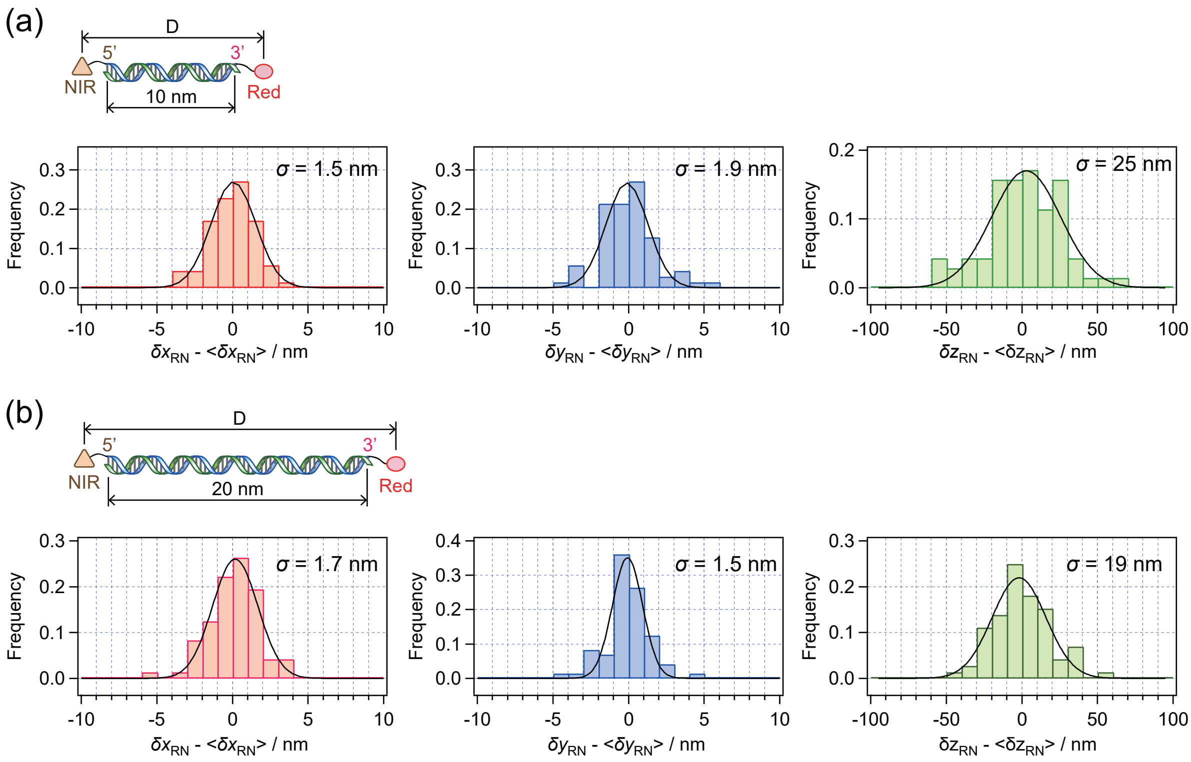

Figure 3.12 The histograms of the deviation of the $xyz$-centroid determination for each 3D colocalization process of (a) the 30-bp dsDNA and (b) the 60-bp dsDNA at 1.8 K.

parameters $\phi_{zx;\mathrm{RN}}$ and $\phi_{zy;\mathrm{RN}}$ are the differences of the tilt angle of the 3D PSF between the red and NIR fluorophores on the $zx$- and $zy$-planes, respectively.

### 3.5.4 Summarized results

The far-field fluorescence localization microscopy of the two fluorophores bonded to the DNA ends at 1.8 K is summarized in Fig. 3.14. $\Delta_{xy}$ was 1 nm and $\Delta_z$ was 11 nm. The details of the estimation of $\Delta_{xy}$ and $\Delta_z$ are given in Fig. 3.12. For each image in Fig. 3.14a, the localization process of the 30-bp dsDNA molecules was repeated more than four times. The true localized positions of the NIR and red fluorophores ($x_{\mathrm{loc;N}}$, $x_{\mathrm{loc;R}}$, $y_{\mathrm{loc;N}}$, and $y_{\mathrm{loc;R}}$) are plotted using triangles and circles, respectively, and the origin of the coordinate axis is the middle point of the two fluorophores for each localization process. The orientation and the length of the dsDNA molecules are clearly imaged. $D_{xy}$ was determined for 20 molecules of the 30-bp dsDNA (all the images in Fig. 3.13.). In the histogram, the distribution of $D_{xy}$ was centered around the DNA length of 10 nm. The average and standard deviation of $D_{xy}$

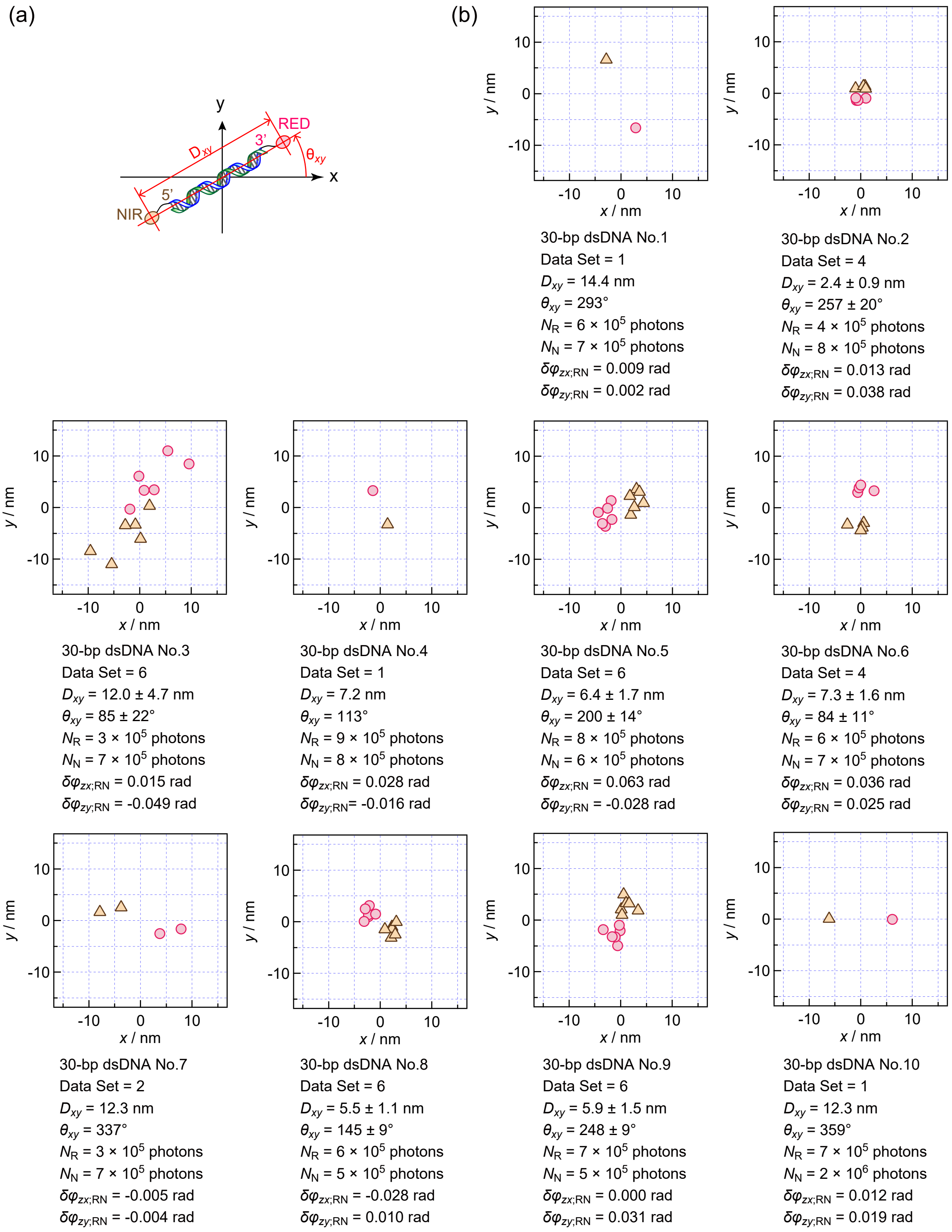

30-bp dsDNA No.1
Data Set = 1
$D_{xy}$ = 14.4 nm
$\theta_{xy}$ = 293°
$N_R = 6 \times 10^5$ photons
$N_N = 7 \times 10^5$ photons
$\delta\varphi_{zx;RN}$ = 0.009 rad
$\delta\varphi_{zy;RN}$ = 0.002 rad

30-bp dsDNA No.2
Data Set = 4
$D_{xy}$ = 2.4 ± 0.9 nm
$\theta_{xy}$ = 257 ± 20°
$N_R = 4 \times 10^5$ photons
$N_N = 8 \times 10^5$ photons
$\delta\varphi_{zx;RN}$ = 0.013 rad
$\delta\varphi_{zy;RN}$ = 0.038 rad

30-bp dsDNA No.3
Data Set = 6
$D_{xy}$ = 12.0 ± 4.7 nm
$\theta_{xy}$ = 85 ± 22°
$N_R = 3 \times 10^5$ photons
$N_N = 7 \times 10^5$ photons
$\delta\varphi_{zx;RN}$ = 0.015 rad
$\delta\varphi_{zy;RN}$ = -0.049 rad

30-bp dsDNA No.4
Data Set = 1
$D_{xy}$ = 7.2 nm
$\theta_{xy}$ = 113°
$N_R = 9 \times 10^5$ photons
$N_N = 8 \times 10^5$ photons
$\delta\varphi_{zx;RN}$ = 0.028 rad
$\delta\varphi_{zy;RN}$= -0.016 rad

30-bp dsDNA No.5
Data Set = 6
$D_{xy}$ = 6.4 ± 1.7 nm
$\theta_{xy}$ = 200 ± 14°
$N_R = 8 \times 10^5$ photons
$N_N = 6 \times 10^5$ photons
$\delta\varphi_{zx;RN}$ = 0.063 rad
$\delta\varphi_{zy;RN}$ = -0.028 rad

30-bp dsDNA No.6
Data Set = 4
$D_{xy}$ = 7.3 ± 1.6 nm
$\theta_{xy}$ = 84 ± 11°
$N_R = 6 \times 10^5$ photons
$N_N = 7 \times 10^5$ photons
$\delta\varphi_{zx;RN}$ = 0.036 rad
$\delta\varphi_{zy;RN}$ = 0.025 rad

30-bp dsDNA No.7
Data Set = 2
$D_{xy}$ = 12.3 nm
$\theta_{xy}$ = 337°
$N_R = 3 \times 10^5$ photons
$N_N = 7 \times 10^5$ photons
$\delta\varphi_{zx;RN}$ = -0.005 rad
$\delta\varphi_{zy;RN}$ = -0.004 rad

30-bp dsDNA No.8
Data Set = 6
$D_{xy}$ = 5.5 ± 1.1 nm
$\theta_{xy}$ = 145 ± 9°
$N_R = 6 \times 10^5$ photons
$N_N = 5 \times 10^5$ photons
$\delta\varphi_{zx;RN}$ = -0.028 rad
$\delta\varphi_{zy;RN}$ = 0.010 rad

30-bp dsDNA No.9
Data Set = 6
$D_{xy}$ = 5.9 ± 1.5 nm
$\theta_{xy}$ = 248 ± 9°
$N_R = 7 \times 10^5$ photons
$N_N = 5 \times 10^5$ photons
$\delta\varphi_{zx;RN}$ = 0.000 rad
$\delta\varphi_{zy;RN}$ = 0.031 rad

30-bp dsDNA No.10
Data Set = 1
$D_{xy}$ = 12.3 nm
$\theta_{xy}$ = 359°
$N_R = 7 \times 10^5$ photons
$N_N = 2 \times 10^6$ photons
$\delta\varphi_{zx;RN}$ = 0.012 rad
$\delta\varphi_{zy;RN}$ = 0.019 rad

Figure 3.13 Localization microscopy of individual 30-bp dsDNA molecules at 1.8 K, determined by the 3D localization process. (a) Molecular coordinates and (b) experimental results.

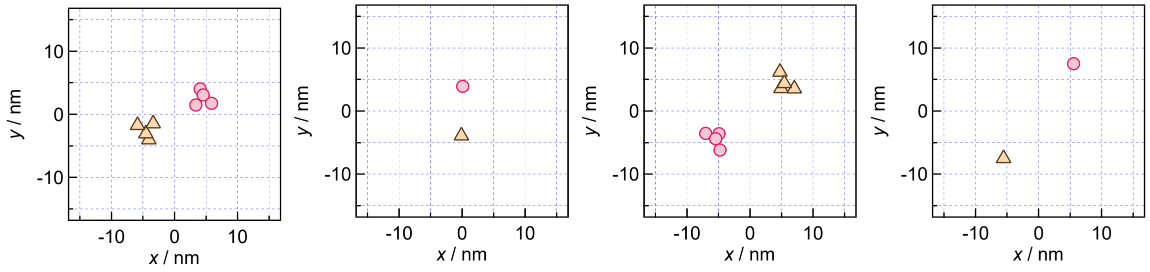

30-bp dsDNA No.11
Data Set = 4
$D_{xy} = 10.3 \pm 1.6$ nm
$\theta_{xy} = 30 \pm 6^\circ$
$N_\mathrm{R} = 6 \times 10^5$ photons
$N_\mathrm{N} = 1 \times 10^6$ photons
$\delta\varphi_{zx;\mathrm{RN}} = 0.002$ rad
$\delta\varphi_{zy;\mathrm{RN}} = -0.004$ rad

30-bp dsDNA No.12
Data Set = 1
$D_{xy} = 7.8$ nm
$\theta_{xy} = 89^\circ$
$N_\mathrm{R} = 1 \times 10^6$ photons
$N_\mathrm{N} = 7 \times 10^5$ photons
$\delta\varphi_{zx;\mathrm{RN}} = 0.003$ rad
$\delta\varphi_{zy;\mathrm{RN}} = 0.010$ rad

30-bp dsDNA No.13
Data Set = 4
$D_{xy} = 14.2 \pm 1.6$ nm
$\theta_{xy} = 219 \pm 5^\circ$
$N_\mathrm{R} = 7 \times 10^5$ photons
$N_\mathrm{N} = 6 \times 10^5$ photons
$\delta\varphi_{zx;\mathrm{RN}} = 0.020$ rad
$\delta\varphi_{zy;\mathrm{RN}} = 0.086$ rad

30-bp dsDNA No.14
Data Set = 1
$D_{xy} = 18.6$ nm
$\theta_{xy} = 54^\circ$
$N_\mathrm{R} = 8 \times 10^5$ photons
$N_\mathrm{N} = 1 \times 10^6$ photons
$\delta\varphi_{zx;\mathrm{RN}} = 0.018$ rad
$\delta\varphi_{zy;\mathrm{RN}} = 0.020$ rad

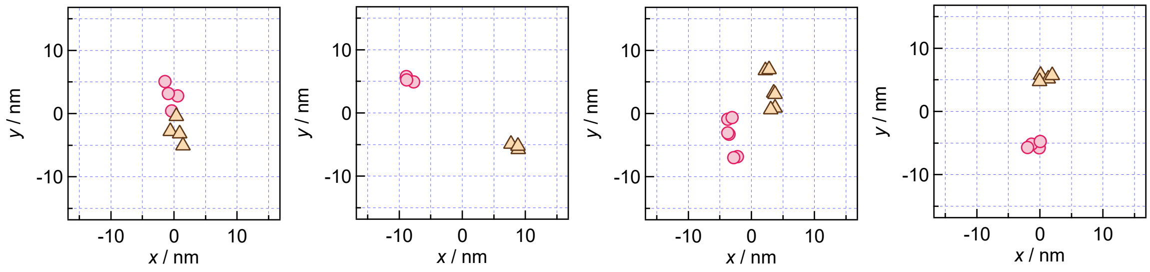

30-bp dsDNA No.15
Data Set = 4
$D_{xy} = 5.8 \pm 2.1$ nm
$\theta_{xy} = 106 \pm 11^\circ$
$N_\mathrm{R} = 6 \times 10^5$ photons
$N_\mathrm{N} = 6 \times 10^5$ photons
$\delta\varphi_{zx;\mathrm{RN}} = -0.015$ rad
$\delta\varphi_{zy;\mathrm{RN}} = 0.024$ rad

30-bp dsDNA No.16
Data Set = 3
$D_{xy} = 20.0$ nm
$\theta_{xy} = 148^\circ$
$N_\mathrm{R} = 7 \times 10^5$ photons
$N_\mathrm{N} = 6 \times 10^5$ photons
$\delta\varphi_{zx;\mathrm{RN}} = 0.027$ rad
$\delta\varphi_{zy;\mathrm{RN}}= -0.014$ rad

30-bp dsDNA No.17
Data Set = 6
$D_{xy} = 9.6 \pm 2.3$ nm
$\theta_{xy} = 221 \pm 11^\circ$
$N_\mathrm{R} = 8 \times 10^5$ photons
$N_\mathrm{N} = 7 \times 10^5$ photons
$\delta\varphi_{zx;\mathrm{RN}} = 0.005$ rad
$\delta\varphi_{zy;\mathrm{RN}} = 0.001$ rad

30-bp dsDNA No.18
Data Set = 4
$D_{xy} = 10.8 \pm 1.1$ nm
$\theta_{xy} = 261 \pm 5^\circ$
$N_\mathrm{R} = 1 \times 10^6$ photons
$N_\mathrm{N} = 7 \times 10^5$ photons
$\delta\varphi_{zx;\mathrm{RN}} = 0.009$ rad
$\delta\varphi_{zy;\mathrm{RN}} = 0.009$ rad

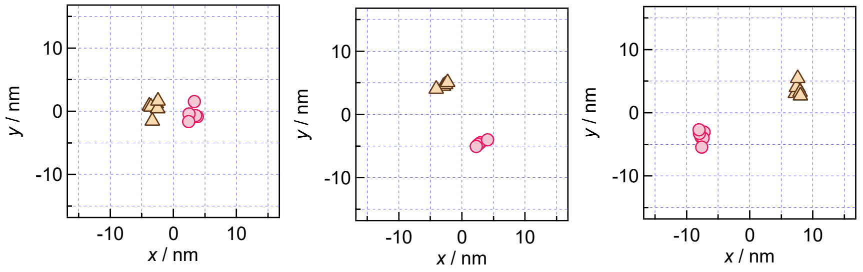

30-bp dsDNA No.19
Data Set = 6
$D_{xy} = 6.2 \pm 1.0$ nm
$\theta_{xy} = 349 \pm 8^\circ$
$N_\mathrm{R} =7 \times 10^5$ photons
$N_\mathrm{N} = 1 \times 10^6$ photons
$\delta\varphi_{zx;\mathrm{RN}} = 0.013$ rad
$\delta\varphi_{zy;\mathrm{RN}} = 0.053$ rad

30-bp dsDNA No.20
Data Set = 4
$D_{xy} = 10.9 \pm 0.9$ nm
$\theta_{xy} = 303 \pm 5^\circ$
$N_\mathrm{R} = 8 \times 10^5$ photons
$N_\mathrm{N} = 9 \times 10^5$ photons
$\delta\varphi_{zx;\mathrm{RN}} = -0.002$ rad
$\delta\varphi_{zy;\mathrm{RN}} = -0.008$ rad

30-bp dsDNA No.21
Data Set = 6
$D_{xy} = 17.0 \pm 0.8$ nm
$\theta_{xy} = 206 \pm 2^\circ$
$N_\mathrm{R} = 8 \times 10^5$ photons
$N_\mathrm{N} = 5 \times 10^5$ photons
$\delta\varphi_{zx;\mathrm{RN}} = 0.014$ rad
$\delta\varphi_{zy;\mathrm{RN}} = -0.043$ rad

Figure 3.13 (continued). Localization microscopy of individual 30-bp dsDNA molecules at 1.8 K, determined by the 3D localization process.

were 10 nm and 5 nm, respectively. Since the persistent length of dsDNA has been reported to be approximately 150 bp, [26] the 30-bp dsDNA molecule mainly formed a straight helical structure. In addition, we did not use a biased sequence, i.e., a multiple repeat of the same base, of the 30-bp dsDNA molecule. Therefore, assuming $D_{xy}$ to be 10 nm, the lateral accuracy of the present work is 5 nm in standard error. The possible causes of the 5-nm residual error in the histogram of Fig. 3.14a are (1) the fluorescence background from the residual fluorophores in the sample, (2) the flexibilities of linkers between the DNA and the fluorophores (5.1 nm), and (3) the orientation of the dsDNA backbone. We measured the 3D images of each fluorophore at the $z$-positions from -900 nm to 900 nm (Fig. 3.8a). The analysis of these defocused images is more susceptible than the 2D centroid determination to disturbance from the background emission from other fluorophores. We performed fluorescence localization microscopy of 60-bp dsDNA molecule at 1.8 K using the 3D localization (left panels in Fig. 3.14b). The correction parameters used were the same as those in the correction of the 30-bp DNA molecules. The standard error of $D_{xy}$ in Fig. 3.14b was almost the same as that for the 30-bp dsDNA molecules in Fig. 3.14a. The distribution of $D_{xy}$ for the 60-bp dsDNA molecules, determined by the 3D localization, (right panel of Fig. 3.14b) was centered at a DNA length of 20 nm.

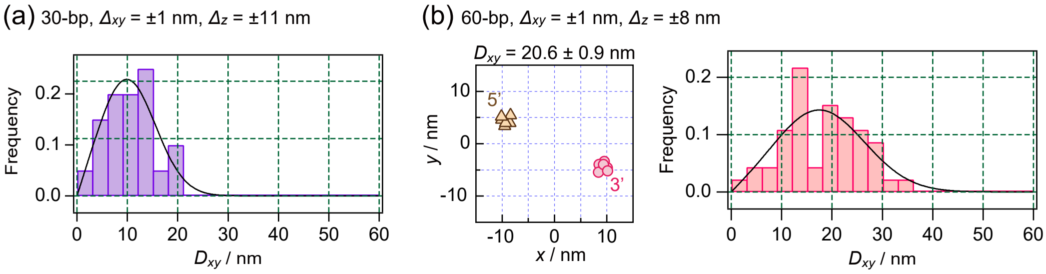

Figure 3.14 Cryo-fluorescence microscopy of two fluorophores bonded to a single dsDNA molecule, using 3D localization with $\Delta_{xy}$ equal to ±1 nm and $\Delta_z$ equal to (a) ±11 nm and (b) ±8 nm. The base-pair number of the dsDNA molecule was (a) 30 and (b) 60. The $xy$-images show the localized positions of the NIR (triangles) and red (circles) fluorophores. The histogram shows $D_{xy}$ for (a) 20 and (b) 46 molecules.

## 3.6 Discussion

### 3.6.1 Comparison between the experiment and optical simulation

Figure 3.15a shows an optical simulation for a PSF tilt due to a dipole-orientation effect. The simulation was performed according to a similar simulation reported from M.D. Lew and W.E. Moerner [20]. We assumed that an objective mirror and an imaging mirror were an aberration-free optics. Points of $N \sim 42000$ were uniformly placed on a spherical surface having a radius of the focal length of the objective ($f_{\mathrm{obj}}$) centered at the focal point of the objective mirror, which is called $S_{\mathrm{obj}}$. The numerical aperture (NA) and the central obstruction in the optical simulation are set to be 0.99 and 0.37 that are equal to our cryo-objective (INAGAWA mirror). A coordinate of the $n$th point represents $f_{\mathrm{obj}}\hat{k}_{\mathrm{obj;n}}$, where $k_{\mathrm{obj;n}}$ is a unit wave vector of the $n$th point on $S_{\mathrm{obj}}$. The electric field of the $n$th point for the divergent beam from the object is given by

$$\vec{E}_{\mathrm{obj};n} = E_0 \exp\left(in_{\mathrm{obj}}kf_{\mathrm{obj}}\{\vec{P} - (\vec{P}\cdot\hat{k}_{\mathrm{obj};n})\hat{k}_{\mathrm{obj};n}\}\right., \tag{3.10}$$

where $n_{\mathrm{obj}}$ is the refractive index at the objective space, $k$ is the wavenumber of light, and $\vec{P}$ is the moment of the transition dipole of a single fluorophore. $\vec{E}_{\mathrm{obj};n}$ is expressed by a $s$-polarized component, $\vec{E}_{s;n}$, and $p$-polarized component, $\vec{E}_{p;n}$,

$$\vec{E}_{\mathrm{obj};n} = E_{s;n}\xi_n + E_{p;n}(\hat{k}_{\mathrm{obj;n}} \times \hat{\xi}_n) \tag{3.11}$$

where $\xi_n$ represents an azimuthal unit vector in a cylindrical coordinate. An ideal mirror can convert a spherical wave or a parallel wave into a parallel wave or spherical wave, respectively. The electric field of the parallel beam from the $n$th point on $S_{\mathrm{obj}}$ is given by

$$\vec{E}_{\parallel;n} = E_{s;n}\xi_n + E_{p;n}(\hat{k}_{\parallel;n} \times \hat{\xi}_n), \tag{3.12}$$

where is $\hat{k}_{\parallel;n}$ is a unit wave vector that is parallel to the $z$-axis. A $n$th point on a surface $S_{\mathrm{img}}$ is defined by a cross point of $\vec{k}_{\parallel;n}$ and $S_{\mathrm{img}}$. The electric field of the convergent beam at the $n$th point on $S_{\mathrm{img}}(\vec{E}_{\mathrm{img};n}))$ can be expressed by the amplitude of $E_{p;n}$ and $E_{s;n}$. $\vec{E}_{\mathrm{img};n}$ is given by

$$\vec{E}_{\mathrm{img};n} = E_{s;n}\hat{\xi}_n + E_{p;n}(\hat{k}_{\mathrm{img};n} \times \hat{\xi}_n), \tag{3.13}$$

where $\hat{k}_{\mathrm{img};n}$ is the unit wave vector at the $n$th point on a spherical surface having a radius of $f_{\mathrm{img}}$ centered at $O_{\mathrm{CCD}}(S_{\mathrm{img}})$. A vector between the $n$th point on $S_{\mathrm{img}}$ and a calculated point ($r_{\mathrm{CCD}}$) is given by

$$\vec{R}_n(\vec{r}_{\mathrm{CCD}}) = \vec{r}_{\mathrm{CCD}} + f_{\mathrm{img}}\hat{k}_{\mathrm{img};n}, \tag{3.14}$$

where $\vec{r}_{\mathrm{CCD}}$ is a vector from $O_{\mathrm{CCD}}$ to $r_{\mathrm{CCD}}$. When a dipole of $\vec{E}_{\mathrm{img};n}$ exists at each point on $S_{\mathrm{img}}$, an electric field at $r_{\mathrm{CCD}}$ generated from the sum of the irradiation of these dipoles is given by

$$\vec{E}(\vec{r}_{\mathrm{CCD}}) = \sum_{n=1}^{\sim 42{,}000} \frac{\exp(i n_{\mathrm{img}} k |\vec{R}_n(\vec{r}_{\mathrm{CCD}})|)}{|\vec{R}_n(\vec{r}_{\mathrm{CCD}})|} \left\{ \vec{E}_{\mathrm{img};n} - \frac{\vec{E}_{\mathrm{img};n} \cdot \vec{R}_n(\vec{r}_{\mathrm{CCD}})}{|\vec{R}_n(\vec{r}_{\mathrm{CCD}})|^2} \vec{R}_n(\vec{r}_{\mathrm{CCD}}) \right\} \tag{3.15}$$

where $n_{\mathrm{img}}$ is a refractive index at the image space. While Lew and Moerner calculated the integral of an electric field, [20] we calculated sum of a finite number of spherical wavelets. A point spread function (PSF) from the dipole transition (Fig. 3.15b) is equal to $|\vec{E}(\vec{r}_{\mathrm{CCD}})|^2$.

Figure 3.15b shows the calculated PSF of a single transition dipole on the $zx$-plane. The molecular orientation angles on the $zx$-plane ($\theta_{zx}$) were set to 0, 15, 30, and 60 deg. In all images, the angle on the $zy$-plane ($\theta_{zy}$) was fixed to 0 deg. As seen in the panels, the PSF tilts with respect to $\theta_{zx}$. The major axis of PSF along the $z$-axis was calculated by fitting the central disk of the $xy$-images at a series of $z$-positions to a 2D Gaussian function. The determined major axes ($x$-centroid) are indicated by double-headed arrows. Figures 3.15c and 3.15d show the PSF tilt angle $\phi_{zx}$ and the peak intensity as a function of $\theta_{zx}$. As seen in the graph, $\phi_{zx}$ is smaller than $\theta_{zx}$ by an order of magnitude. The relationship is consistent with that reported by earlier works [18–20].

### 3.6.2 $z$-dependent $xy$-shift from dipole orientation effect

The $z$-dependent $xy$-shift caused by the PSF tilt is discussed in this section. In Fig. 3.11, the standard deviation of the PSF tilt angles of the individual fluorophores was 0.02 rad on the $zx$- and $zy$-plane ($\sigma_{\phi xz}$ and $\sigma_{\phi xy}$). The PSF tilt angle $\phi$ in the image space is known

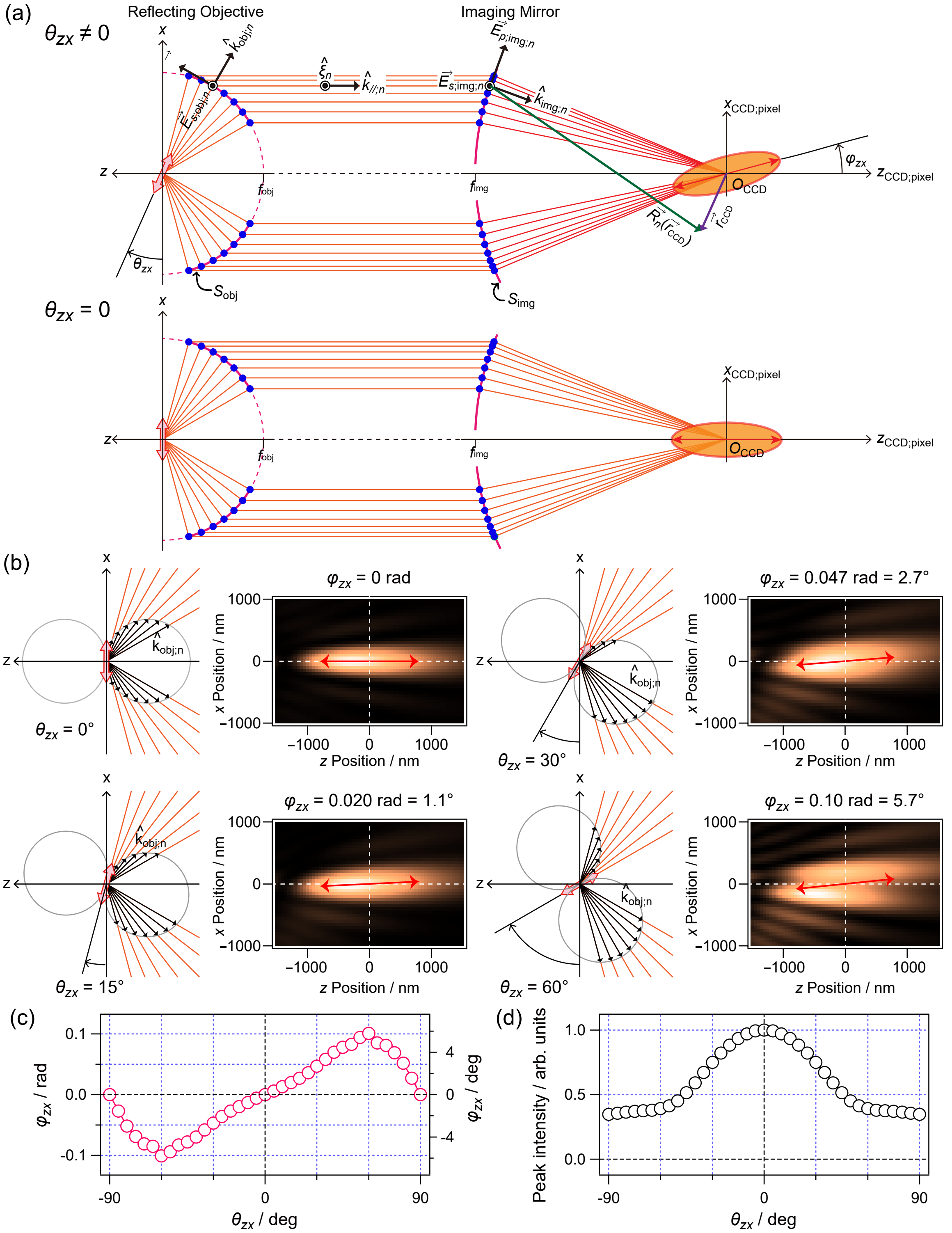

Figure 3.15 Optical simulation for the PSF tilt due to the transition-dipole orientation of a single fluorophore. (a) Optical arrangement of the simulation. The top is the case that the dipole tilts in the $z$-direction ($\theta_{zx} \neq 0$) and the bottom is the case that the dipole aligns to the $z$-direction ($\theta_{zx} = 0$). (b) Optical simulation for the $zx$-plane of PSF with the molecular orientation angle $\theta_{zx}$ = 0, 15, 30, and 60 deg. The orientation angle on the $zy$ plane ($\theta_{zy}$) was fixed to 0 deg. (c) The PSF tilt angle $\phi_{xz}$ and (d) the peak intensity of the PSF as a function of $\theta_{zx}$

to be smaller than the dipole-orientation angle $\theta$ in the objective space by an order of magnitude [18–20]. The optical simulation of the PSF tilt occurring in our reflecting microscope (Fig. 3.15) suggests that randomly orientated fluorophores in the objective space ($-90^\circ < \theta < 90^\circ$) give rise to the PSF tilt angles $\phi$from -0.1 rad to 0.1 rad (the peak to valley). The simulation is consistent with the present observation (Fig. 3.11). Under the condition in Fig. 3.6b of $\Delta_z$ being equal to ±700 nm, the $z$-dependent $xy$-shift of each fluorophore due to the PSF tilt, $\sqrt{(\Delta_z \sigma_{\phi zx})^2 + (\Delta_z \sigma_{\phi zy})^2}$, was estimated to be approximately ±20 nm. The error of the distance measurement was estimated to be ±30 nm; and the error exceeded the size of the 30-bp dsDNA molecule. The histogram of Fig. 3.6b was fitted to a non-Gaussian distribution [27], assuming that $D_{xy}$ (signal, μ) was fixed at 10.2 nm. The fitting result is depicted by a black curve. (For clarification, the fitting results of the non-Gaussian distribution in Fig. 3.14a and 3.14b are also drawn using the black curves.) From the fitting, the error (noise, $\sigma$) of Fig. 3.6b was 15 nm. The distance error from the non-Gaussian distribution fitting is consistent with that of ±30 nm estimated from the focal depth of ± 700 nm. Because $\Delta_z$ was ±11 nm and ±9 nm in Figs. 3.14a and 3.14b, respectively, the systematic error due to the PSF tilt was expected to be at an Angstrom level (± 0.3 nm).

### 3.6.3 An inquiry of dipole orientation for near-field fluorescence microscope

Among the dipole orientation effects of localization microscopy, PSF distortion has been mainly studied with a 2D image measured by a near-field fluorescence (total internal reflection florescence, TIRF) microscope [14–17, 21, 22]. Mortensen et al. demonstrated via TIRF microscopy that the lateral accuracy of the distance between two fluorophores was reduced to a nanometer level by considering the dipole orientation (PSF distortion) in 2D localization [21, 22]. Note that the near-field microscope cannot be applied to the observation of an interior of a thick sample because the excitation is restricted from a region of 0.1 μm from the surface. On the other hand, the far-field microscope has been widely utilized in the observation of whole cells because the observable region of the far-field microscope is > 1 mm. However, J. Engelhardt et al. reported that far-field 2D localization microscopy contains a systematic error due to the PSF tilt up to ±125 nm because of the large focal depth [18]. We experimentally show in Fig. 3.6b that the systematic error of far-field 2D microscopy (±15 nm) exceeds the size of macromolecules. Although reduction of this systematic error has been attempted by 3D imaging with a double-helix PSF method [19] and with an azimuthal polarization filter [20], under physiological conditions, the lateral accuracy of far-field localization microscopy remained at several tens of nanometers, mainly due to the movements of molecules. In the present work, using cryo-immobilization, we have improved the $xy$-precision and simultaneously the $z$-precision to ±1 nm and ±11 nm, respectively. By correcting the dipole orientation effects (the PSF tilt and the PSF distortion), the lateral accuracy of each fluorophore has been improved to a nanometer level (see the histogram of Fig. 3.15a).

## 3.7 Conclusion

We demonstrate that the correction of the dipole orientation effects (the PSF tilt and the PSF distortion) is necessary for nanometer accuracy in far-field cryo-fluorescence microscopy of individual fluorophores. Compared with other cellular-imaging methods, including cryo-electron tomography, the far-field fluorescence microscopy intrinsically has a unique capability to simultaneously realize the optical sectioning of a whole cell and the single molecule sensitivity. Recently, we have developed near-infrared fluorophore for a spectral-selective cryo-localization microscopy, which we called a ”Förster-resonance-energy-transfer (FRET) pair” [7]. Under cryogenic conditions, the fluorescence excitation spectrum of the FRET pair becomes narrower than that of the ensemble; accordingly, the FRET pair can be selected from an ensemble of the same fluorophore within the diffraction-limited spot. Additionally, in the near-infrared wavelength region of the fluorescence of the FRET pair (approximately 800 nm), the autofluorescence background of cells is 3 – 4 orders of magnitude weaker than in the blue region (400 – 500 nm). The FRET pair will enable background-free cryo-localization microscopy of cells. Thus, the far-field cryo-fluorescence localization microscopy will contribute to revealing the molecular-level mechanism of biochemical processes in cellular interiors.

# Reference List

[1] G. Wolff, C. Hagen, K. Grünewald and R. Kaufmann: “Towards correlative super-resolution fluorescence and electron cryo-microscopy”, Biology of the Cell, **108**, 9, pp. 245–258 (2016).

[2] J. Dubochet, M. Adrian, J.-J. Chang, J.-C. Homo, J. Lepault, A. W. McDowall and P. Schultz: “Cryo-electron microscopy of vitrified specimens”, Quarterly Reviews of Biophysics, **21**, 2, pp. 129–228 (1988).

[3] M. Fernández-Suárez and A. Y. Ting: “Fluorescent probes for super-resolution imaging in living cells”, Nature Reviews Molecular Cell Biology, **9**, 12, pp. 929–943 (2008).

[4] F. Huang, G. Sirinakis, E. S. Allgeyer, L. K. Schroeder, W. C. Duim, et al.: “Ultra-high resolution 3D imaging of whole cells”, Cell, **166**, 4, pp. 1028–1040 (2016).

[5] W. E. Moerner and L. Kador: “Optical detection and spectroscopy of single molecules in a solid”, Physical Review Letters, **62**, 21, pp. 2535–2538 (1989).

[6] M. Orrit and J. Bernard: “Single pentacene molecules detected by fluorescence excitation in a *p*-terphenyl crystal”, Physical Review Letters, **65**, 21, pp. 2716–2719 (1990).

[7] H. Tabe, K. Sukenobe, T. Kondo, A. Sakurai, M. Maruo, A. Shimauchi, M. Hirano, S.-n. Uno, M. Kamiya, Y. Urano, M. Matsushita and S. Fujiyoshi: “Cryogenic fluorescence localization microscopy of spectrally selected individual FRET pairs in a water matrix”, The Journal of Physical Chemistry B, **122**, 27, pp. 6906–6911 (2018).

[8] A. Bloeß, Y. Durand, M. Matsushita, H. Van Dermeer, G. Brakenhoff and J. Schmidt: “Optical far-field microscopy of single molecules with 3.4 nm lateral resolution”, Journal of Microscopy, **205**, 1, pp. 76–85 (2002).

[9] A. Van Oijen, J. Köhler, J. Schmidt, M. Müller and G. Brakenhoff: “3-Dimensional super-resolution by spectrally selective imaging”, Chemical Physics Letters, **292**, 1-2, pp. 183–187 (1998).

[10] S. Weisenburger, D. Boening, B. Schomburg, K. Giller, S. Becker, C. Griesinger and V. Sandoghdar: “Cryogenic optical localization provides 3D protein structure data with angstrom resolution”, Nature Methods, **14**, 2, pp. 141–144 (2017).

[11] T. Furubayashi, K. Motohashi, K. Wakao, T. Matsuda, I. Kii, T. Hosoya, N. Hayashi, M. Sadaie, F. Ishikawa, M. Matsushita and S. Fujiyoshi: “Three-dimensional local-

ization of an individual fluorescent molecule with angstrom precision", Journal of the American Chemical Society, **139**, 26, pp. 8990–8994 (2017).

[12] L. S. Churchman, Z. Ökten, R. S. Rock, J. F. Dawson and J. A. Spudich: "Single molecule high-resolution colocalization of Cy3 and Cy5 attached to macromolecules measures intramolecular distances through time", Proceedings of the National Academy of Sciences of the United States of America, **102**, 5, pp. 1419–1423 (2005).

[13] A. Pertsinidis, Y. Zhang and S. Chu: "Subnanometre single-molecule localization, registration and distance measurements", Nature, **466**, 7306, pp. 647–651 (2010).

[14] A. P. Bartko and R. M. Dickson: "Imaging three-dimensional single molecule orientations", The Journal of Physical Chemistry B, **103**, 51, pp. 11237–11241 (1999).

[15] J. Enderlein, E. Toprak and P. R. Selvin: "Polarization effect on position accuracy of fluorophore localization", Optics Express, **14**, 18, pp. 8111–8120 (2006).

[16] F. Aguet, S. Geissbühler, I. Märki, T. Lasser and M. Unser: "Super-resolution orientation estimation and localization of fluorescent dipoles using 3-D steerable filters", Optics Express, **17**, 8, pp. 6829–6848 (2009).

[17] K. I. Mortensen, L. S. Churchman, J. A. Spudich and H. Flyvbjerg: "Optimized localization analysis for single-molecule tracking and super-resolution microscopy", Nature Methods, **7**, 5, pp. 377–381 (2010).

[18] J. Engelhardt, J. Keller, P. Hoyer, M. Reuss, T. Staudt and S. W. Hell: "Molecular orientation affects localization accuracy in superresolution far-field fluorescence microscopy", Nano Letters, **11**, 1, pp. 209–213 (2010).

[19] M. P. Backlund, M. D. Lew, A. S. Backer, S. J. Sahl, G. Grover, A. Agrawal, P. Rafael and M. WE: "Simultaneous, accurate measurement of the 3d position and orientation of single molecules", Proceedings of the National Academy of Sciences of the United States of America, **109**, 47, pp. 19087–19092 (2012).

[20] M. D. Lew and W. Moerner: "Azimuthal polarization filtering for accurate, precise, and robust single-molecule localization microscopy", Nano Letters, **14**, 11, pp. 6407–6413 (2014).

[21] K. I. Mortensen, J. Sung, H. Flyvbjerg and J. A. Spudich: "Optimized measurements of separations and angles between intra-molecular fluorescent markers", Nature Com-

munications, **6**, p. 8621 (2015).

[22] K. I. Mortensen, J. Sung, J. A. Spudich and H. Flyvbjerg: “How to measure separations and angles between intramolecular fluorescent markers”, Methods in Enzymology, Vol. 581, Elsevier, pp. 147–185 (2016).

[23] T. Hinohara, Y. I. Hamada, I. Nakamura, M. Matsushita and S. Fujiyoshi: “Mechanical stability of a microscope setup working at a few kelvins for single-molecule localization”, Chemical Physics, **419**, pp. 246–249 (2013).

[24] H. Inagawa, Y. Toratani, K. Motohashi, I. Nakamura, M. Matsushita and S. Fujiyoshi: “Reflecting microscope system with a 0.99 numerical aperture designed for three-dimensional fluorescence imaging of individual molecules at cryogenic temperatures”, Scientific Reports, **5**, p. 12833 (2015).

[25] R. Zondervan, F. Kulzer, M. A. Kol’chenk and M. Orrit: “Photobleaching of rhodamine 6G in poly (vinyl alcohol) at the ensemble and single-molecule levels”, The Journal of Physical Chemistry A, **108**, 10, pp. 1657–1665 (2004).

[26] C. G. Baumann, S. B. Smith, V. A. Bloomfield and C. Bustamante: “Ionic effects on the elasticity of single DNA molecules”, Proceedings of the National Academy of Sciences of the United States of America, **94**, 12, pp. 6185–6190 (1997).

[27] L. S. Churchman, H. Flyvbjerg and J. A. Spudich: “A non-gaussian distribution quantifies distances measured with fluorescence localization techniques”, Biophysical Journal, **90**, 2, pp. 668–671 (2006).

# Chapter 4

# Conclusion

We developed a far-field fluorescence microscope for localization of individual fluorophores under cryogenic condition. To realize subangstrom mechanical stability, the objective mirror and a sample are set to a monolithic holder and the holder is cooled down to a few K. By the microscope, we demonstrated localization of an individual ATTO647N molecule with angstrom precision in 3D. However, the precision of individual fluorophore is different from the accuracy of a relative distance between multiple fluorophores. We measured red and near-infrared fluorophores labeled with two ends of dsDNA. The length of DNA is 10.2 nm. The red fluorophore can be distinguished from the NIR dye by absorption and fluorescence wavelength. Although $xy$-localization precision $\Delta_{xy}$ was 1 nm, the $xy$-projection of the distance between the two fluorophores ($D_{xy}$) was distributed from 0 to 50 nm when the $z$-localization precision $\Delta_z$ was $\sim$ 700 nm. Mislocalization was mainly caused by $z$-dependent $xy$-shift due to the dipole orientation effect. We measured 3D-PSF and obtained the dipole orientation angle of each fluorophore. As a result, the distance between two fluorophores was centered at the DNA length. The accuracy of the localization microscopy was established to 5 nm.

This microscope possibly provides 3D structure of nucleosome in nucleus. The nucleosome is a structure containing DNA that is wrapped around histone octamer [1]. A histone modification occurs activation or innactivation of transcription to RNA from DNA. Thank to chemical biological technique, molecule level labeled fluorophore has been established. The modification such as methylation or acetylation can be labeled by the technique of immunofluorescence and observed by fluorescence microscope. The histone octamer size is 11 nm, which size can be observed by 5-nm accurate microscope. However, multiple nucleosome are existed in optical resolution. we need to distinguish these nucleosomes. Recently, H. Tabe et al. developed near-infrared fluorophore for spectral-selective cryo-localization microscopy, which they called a "Förster resonance energy transfer (FRET) pair" [2]. Using this FRET pair, we will possible resolve tens of relative positions of fluorophores labeled nucleosome.

## Reference List

[1] H. Kimura, Y. Hayashi-Takanaka, T. J. Stasevich and Y. Sato: "Visualizing posttranslational and epigenetic modifications of endogenous proteins in vivo", Histochemistry and Cell Biology, **144**, 2, pp. 101–109 (2015).

[2] H. Tabe, K. Sukenobe, T. Kondo, A. Sakurai, M. Maruo, A. Shimauchi, M. Hirano, S.-n. Uno, M. Kamiya, Y. Urano, M. Matsushita and S. Fujiyoshi: "Cryogenic fluorescence localization microscopy of spectrally selected individual FRET pairs in a water matrix", The Journal of Physical Chemistry B, **122**, 27, pp. 6906–6911 (2018).

# Acknowledgment

This Ph.D. thesis is the result of research at Matsushita Lab. for 5 years. I thank many people for their kind advices and supports. First, I would like to thanks Associate Professor M. Matsushita, the supervisor of my study. I also appreciate to examiners, Prof. T. Sasamoto, Prof. M. Notomi, Prof. T. Satoh, and Prof. M. Vacha for their advices to improve my thesis.

In Chepter 2, I thank coauthers of " Three-dimensional localization of individual fluorescent molecule with angstrom precision ", Kazuya Motohashi, Keisuke Wakao, Tsuyoshi Matsuda, Isao Kii, Takamitsu Hosoya, Nobuhiro Hayashi, Mahito Sadaie, Michio Matsushita, and Satoru Fujiyoshi. Moreover, I thank Martin Vacha for helpful discussions and comments and Hiromu Kashida for helpful comments. This work was financially supported by Grants-in-Aid for Scientific Research (16H04094, 15H02383, and 15H03765) and JST/PRESTO (JPMJPR14FC).

In Chepter 3, I thank coauthers of " Nanometer Accuracy in Cryogenic Far-Field Localization Microscopy of Individual Molecules " , Keita Ishida, Hiromu Kashida, Eiji Nakata, Takashi Morii, Michio Matsushita, and Satoru Fujiyoshi. Moreover, I thank Makio Tokunaga, Martin Vacha, and Ryo Iizuka for helpful comments and discussion. This work was financially supported by JST/CREST (JPMJCR15G2), JST/PREST (JPMJPR14FC), and Grants-in-Aid for Scientific Research (16H04094 and 18K19054).

This Ph.D. study had been given technical support and advises that lead this thesis. I thank H. Kashida from Nagoya University for helpful advises about DNA sequence and E. Nakata from Kyoto University helpful confirming and providing DNA sample. I consider realizing this study is far away without their technical supports. This work was supported by Grant-in-Aid for JSPS Fellows 19J13557. I appreciate for this financial support.

I am deeply grateful to members of Matsushita Lab. in Tokyo Institute of Technology. Particularly, Dr. S. Fujiyoshi, the assistant professor of Matsushita Lab. instructed about research of method and responsible, and advised study. K. Motohashi developed cryogenic fluorescence microscope with me and measured Qdot sample. K. Ishida built a program of optical simulation and calculated dipole orientation effect. I thank all members studying with me in the laboratory.

Thanks to my friends advised at times and encouraged at another time. I deeply thanks to family, especially father, mother, and brother. My parents have brought me up and fot a lot of things. Thank you very much. I will continue work hard.